Alma Mater Studiorum - Università di Bologna

Fermi blazars as candidate neutrino emitters: a study of temporal coincidence with IceCube events

Tesi di Laurea Magistrale

Candidata:
Loreta Minutilli

Relatore:
**Chiar.mo Prof.
Cristian Vignali**

Co-relatori:
Prof.ssa Paola Grandi

Abstract

Multimessenger astronomy provides a unique tool for exploring the universe at the highest energies. While photons at $E > 100$ TeV are stopped by the interaction with matter before reaching Earth, cosmic neutrinos produced in the same sources can travel unimpeded and reach us: as a consequence, the association between neutrinos and their astrophysical sources would constitute a powerful probe of the high-energy sky.

The search for the neutrino counterparts was significantly pushed by the Ice-Cube observatory through a program of prompt alerts in 2016, with the purpose of allowing rapid multi-wavelength follow-up observations. In 2017, the neutrino event IceCube-170922A was found to be coincident in arrival time and direction with an enhanced γ-ray activity from the blazar TXS 0506+056 at redshift $z \sim 0.34$. The association between this source and the event was confirmed at the 3σ confidence level through a likelihood ratio test, making TXS 0506+056 the first extragalactic neutrino source (IceCube Collaboration et al. 2018a).

This discovery motivates further research in the field of the blazar-neutrino connection. These objects feature a double-humped SED and can be classified on the basis on the position of their low energy peak due to synchrotron emission as HBL ($\nu_{peak}^{S} \geq 10^{15}$ Hz), IBL ($10^{14} < \nu_{peak}^{S} < 10^{15}$) and LBL ($\nu_{peak}^{S} \leq 10^{14}$). In Giommi et al. (2020) a study of *spatial* coincidence between a sample of IceCube events and blazars found in their error regions (ellipses with area smaller than a circle with radii 3°) was performed. A stastistical excess of $\sim 3.5\sigma$ over background expectations was found for the class of HBLs and IBLs, while no excess was found for the LBL class.

In this work, the *temporal* coincidence between the arrival times of IceCube neutrinos and the γ-ray ($0.1 - 300$ GeV) emission from blazars is investigated. The sample of blazars selected by Giommi et al. (2020) was matched with sources detected by *Fermi*-LAT in the 4FGL and 3FGL catalogues. A selection of 61 γ-ray emitting blazars was obtained, and the γ-ray light curves of the sources centered on the associated IceCube events were built in order to study their variability on short time scales (6-months with 7-days binning, 3-months with 3-days binning and 1-month with 1-day binning) and to allow a search for *flare-neutrino coincidences*.

The same light curves were built for TXS 0506+056 as a comparison.

The different nature of LBLs and IBLs/HBLs in the sample, with the former peaking in the *Fermi* energy range and the latter in the $\sim$TeV range, forced us to adopt different criteria for the selection of a *flaring* state for LBLs and IBLs/HBLs, treating the two classes separately. A subsample of 6 promising *flaring* blazars (4 LBLs, 1 HBL and 1 IBL) in the 6-months interval centered on the neutrino event was selected. Among these sources, 4 were found *coincident* with the neutrino event, i.e. the event was comprised in the 7-days interval centered on a detection.

The nature of these coincidences has been investigated with a statistical approach by performing a likelihood ratio test in order to assess if they are casual or due to astrophysical events. An interesting excess over background expectations is found for the HBLs/IBLs class, while no excess is found for the LBLs, in agreement with the results reported in Giommi et al. (2020).

We discussed the implications of these results for the blazar-neutrino connection: the lack of *temporal* coincidences between the arrival time of the neutrino and an enhanced state of γ-ray emission from the sources could be either due to a poor photon statistics linked to the sensitivity of the instrument or to the properties of the phenomenon. Models where the γ-ray flaring activity of blazars can be suppressed if the source is a highly efficient neutrino emitters and models were the neutrino emission is accompanied by enhanced emission in other energy bands (X-rays) are presented. The Cherenkov Telescope Array (CTA) will enable a distinction between the two hypotheses thanks to its high sensitivity and capability of detecting events with energies up to 300 TeV.

Sommario

L'astronomia *multimessanger* è uno strumento fondamentale per l'esplorazione dell'universo alle altissime energie. Mentre i fotoni con $E > 100$ TeV vengono assorbiti dall'interazione con la materia prima di raggiungere la Terra, i neutrini cosmici prodotti nelle stesse sorgenti possono viaggiare senza impedimenti fino a raggiungerci: di conseguenza, l'associazione tra i neutrini cosmici e le loro sorgenti sarebbe una potente sonda per esplorare il cielo alle più alte energie.

La ricerca delle controparti dei neutrini cosmici è stata significativamente incoraggiata dall'Osservatorio IceCube tramite un programma di allerte immediate nel 2016, con lo scopo di favorire rapide osservazioni supplementari a diverse lunghezze d'onda. Nel 2017, è stata trovata per l'evento IceCube-170922A una coincidenza in termini di direzione e tempo di arrivo con uno stato di alta attività γ del blazar TXS 0506+056 a redshift $z \sim 0.34$. L'associazione tra questa sorgente e l'evento è stata confermata al livello di confidenza 3σ tramite un *likelihood ratio test* (IceCube Collaboration et al. 2018a).

La scoperta motiva ulteriore ricerca nel campo della connessione tra neutrini e blazar. Questi oggetti hanno una SED con doppio picco e possono essere classificati sulla base delle posizione del picco a più bassa energia in HBL ($\nu_{peak}^{S} \geq 10^{15}$ Hz), IBL ($10^{14} < \nu_{peak}^{S} < 10^{15}$) e LBL ($\nu_{peak}^{S} \leq 10^{14}$). In Giommi et al. (2020) è stato effettuato uno studio di coincidenza *spaziale* tra un campione di eventi IceCube e i blazar trovati nelle loro regioni d'errore (ellissi con aree inferiori a quelle di un cerchio di raggio 3°). È stato trovato un eccesso rispetto alle aspettative di background con significatività $\sim 3.5\sigma$ per la classe degli HBLs e degli IBLs, mentre non è stato trovato alcun eccesso per i LBLs.

In questo lavoro di tesi è stata investigata la coincidenza *temporale* tra il tempo di arrivo dei neutrini IceCube e l'emissione γ ($0.1 - 300$ GeV) dei blazars. Il campione selezionato da Giommi et al. (2020) è stato abbinato a sorgenti rivelate da *Fermi*-LAT nei cataloghi 4FGL e 3FGL. Una selezione di 61 blazars attivi in banda γ è stata così ottenuta e per queste sorgenti sono state costruite le curve di luce centrate sugli eventi IceCube associati, con lo scopo di studiarne la variabilità su tempi scala brevi (6 mesi con binning di 7 giorni, 3 mesi con binning di 3 giorni e 1 mese con binning di 2 giorni) e di consentire una ricerca di *coincidenze flare-*

neutrino. Le stesse curve di luce sono state costruite per TXS 0506+056 come confronto.

La diversa natura dei LBL e degli IBL/HBL del campione, con i primi che presentano il picco nell'intervallo di energia coperto da *Fermi* e i secondi nella banda TeV, ci ha forzati ad adottare criteri diversi per definire uno stato *flaring* nei LBL e negli IBL/LBL, trattando le due classi separatamente. È stato così selezionato un sottocampione di 6 promettenti blazar *flaring* (4 LBL, 1 HBL e 1 IBL) nell'intervallo di 6 mesi centrato sull'evento neutrino. Tra queste sorgenti, 4 sono *coincidenti* con il neutrino, ossia, l'evento neutrino è compreso nell'intervallo di 7 giorni centrato su una misura di flusso.

La natura di queste coincidenze è investigata con un approccio statistico tramite un *likelihood ratio test* con lo scopo di stabilire se sono casuali o dovute a eventi astrofisici. Un interessante eccesso rispetto alle previsioni di background è stato trovato per gli HBL/IBL, mentre nessun eccesso è stato trovato per i LBL, in accordo con i risultati di Giommi et al. (2020).

Le implicazioni di questi risultati per la connessione blazar-neutrini sono state discusse: la mancanza di *coincidenze temporali* tra il tempo di arrivo del neutrino e uno stato di elevata attività γ delle sorgenti potrebbe essere dovuto a una bassa statistica di fotoni legata alla sensitività dello strumento o alle proprietà del fenomeno. Sono presentati dei modelli in cui l'attività γ *flaring* dei blazars può essere soppressa se la sorgente emette neutrini con efficienza e modelli in cui l'emissione di neutrini è accompagnata da emissione in altre bande energetiche (raggi X). Il Cherenkov Telescope Array (CTA) consentirà di discriminare tra queste ipotesi grazie alla sua alta sensitività e alla capacità di rivelare eventi con energie fino a 300 TeV.

Contents

Chapter 1

High-Energy Neutrino Astrophysics

Neutrinos are electrically neutral fermions produced by the decay of radioactive elements and in high-energy collisions. They are only affected by the weak subatomic force and by gravity.

Their existence was first postulated by Wolfgang Pauli in 1930 in order to explain the missing energy and angular momentum in the final state of beta decays. The phenomena was thought to be due to an undetected, mass-less and electrically neutral particle which was baptized *neutrino* by Enrico Fermi in 1934.

The first detection of a neutrino by an experiment dates back to 1956, when C. Cowan, F. Reines, F. Harrison, H. Kruse and A. McGuire published on Science "Detection of the Free Neutrino: a Confirmation" (Cowan et al. 1956). Their result was awarded with the 1995 Nobel Prize for Physics.

In 1962, the interactions of muon neutrinos were first discovered by L. Lederman, M. Schwartz and J. Steinberger: this was the proof that more than one type of neutrino exists. Neutrinos are in fact created in one of the three leptonic flavors: electronic neutrinos (ν_e), muon neutrinos (ν_μ) and tau neutrinos (ν_τ). They are always associated with the corresponding charged lepton or antilepton.

The idea of neutrino mass was first introduced by B. Pontecorvo in 1958 by means of flavor oscillations. The theory, which was formalized and refined in the following years, states that each neutrino flavor state is a linear combination of three discrete mass eigenstates. Since the three mass components of the flavor state travel at slightly different speeds, neutrino oscillations between different flavors are possible in flight (Gonzalez-Garcia and Maltoni 2008).

In *multimessenger astronomy* different probes are used to study the same astrophysical event or system. Neutrinos are particularly valuable astronomical messengers: they are able to emerge from deep inside their sources without absorption

and their small interaction cross-section allows them to travel long distances without interference. Unlike charged particles, they are not deflected by magnetic fields (Becker 2008).

At the same time, their feeble interaction with matter makes neutrinos extremely difficult to detect.

1.1 Astrophysical production of high-energy neutrinos

High-energy neutrinos can be produced in astrophysical environments in two ways. The first one is the decay of charged pions generated in proton-proton collisions:

$$p + p \rightarrow \pi^{\pm}, \pi^0, K^{\pm}, K^0, p, n... \tag{1.1}$$

The process described in Eq. 1.1 is often called *astrophysical beam dump* mechanism, given its similarity with the process of production of secondary hadrons in a fixed-target experiment. The cross-section[1] for Eq. 1.1 is $\sigma_{pp} \sim 40-50$ mb (Braibant et al. 2011).

In the *beam dump* process, almost the same number of π^+, π^- and π^0 are produced. The neutral pions decay immediately in two γ rays. The π^+ decays as

$$\pi^+ \rightarrow \mu^+ \nu_{\mu} \quad . \tag{1.2}$$

The process described in Eq. 1.2 is followed by

$$\mu^+ \rightarrow e^+ \nu_e \overline{\nu}_{\mu} \quad . \tag{1.3}$$

The charge conjugate reaction occurs for π^-. Therefore, three neutrinos are produced for each pion and six neutrinos for every two γ rays.

Secondary mesons and thus neutrinos can be produced by *photoproduction* as well. This mechanism is based on the interaction of high-energy protons with ambient photons (γ_{ϵ}) in the surroundings of the source. The process occurs through the Δ^+ resonance:

$$p + \gamma_{\epsilon} \rightarrow \Delta^+ \rightarrow \pi^0 + p \tag{1.4a}$$

$$p + \gamma_{\epsilon} \rightarrow \Delta^+ \rightarrow \pi^+ + n \tag{1.4b}$$

Neutrinos are then produced according to Eq. 1.2 and Eq. 1.3. Each individual channel has a cross-section $\sigma_{\gamma p} \sim 0.250$ mb. This number is two orders of

---

[1]The *cross section* is the probability that a collisional process will take place. It has the physical dimensions of an area and it is measured in *barn* (b), where 1 b = 10^{-24} cm^2.

magnitude smaller than the cross-section σ_{pp}, nonetheless in some astrophysical environments neutrinos are more likely to be produced due to Eq. 1.4b than following a *beam dump* mechanism. This happens because the event rate for the beam dump mechanism is given by

$$ER = \sigma_{pp}nc \ , \tag{1.5}$$

where n is the environmental matter number density, while the event rate for photoproduction is

$$ER = \sigma_{\gamma p}n_{\gamma}c \ , \tag{1.6}$$

where n_{γ} is the ambient photon number density. Typically, n_{γ} is much larger than n.

The average energy of the pion produced by Eq. 1.4b is a fraction $f_{p\pi} \sim 0.2$ of the energy of the parent proton, and each of the four leptons produced in the π^{+} decay chain carries roughly $1/4$ of the pion's energy. As a consequence, the neutrino energy from the π^{+} decay is a fraction

$$E_{\nu} \sim 0.05E_{p} \tag{1.7}$$

of the energy of the parent proton. Since there are three neutrinos and one positron in the final state given by Eq. 1.2 and Eq. 1.3, the energy transferred to neutrinos is about $(1/3) \times (3/4) = 1/4$. The positron annihilates producing additional photons, therefore the energy transferred to photons is $(2/3)+(1/3)\times(1/4) = 3/4$. As a consequence, the ratio of neutrino to photon luminosity in photoproduction processes is

$$\frac{L_{\nu}}{L_{\gamma}} = \frac{1}{3} \ . \tag{1.8}$$

The astrophysical sources where neutrino production is thought to be occurring are described in detail in 2.

Given their production mechanism, the expected flux ratio for neutrinos of different flavors is

$$\nu_{e} : \nu_{\mu} : \nu_{\tau} = 1 : 2 : 0 \tag{1.9}$$

However, after their production in astrophysical sources, neutrinos travel a long distance before being detected by Earth-based facilities. This distance is much longer than the length scale of flavor oscillations, therefore the observable flavor composition is the oscillation average (Ahlers and Halzen 2015 and Chiarusi and Spurio 2010):

$$\nu_{e} : \nu_{\mu} : \nu_{\tau} = 1 : 1 : 1 \ \ . \tag{1.10}$$

The existence of a diffuse flux of astrophysical neutrinos is a direct consequence of Cosmic Rays (CR) observations: in a multimessanger picture, the same astrophysical sources can produce Ultra High-Energy CRs and high-energy neutrinos (see Chap. 2).

From now on, ν will indicate both neutrinos and antineutrinos.

1.2 Detection of high-energy neutrinos

1.2.1 Interaction with matter of high-energy neutrinos

High-energy neutrinos can interact with matter via inelastic scattering on nucleons. This process can occur with the exchange of a Z boson (*neutral current* weak interaction, NC)

$$\nu_l + N \to \nu_l + X \quad , \quad l = e, \mu, \tau \ . \tag{1.11}$$

In this situation, the hadronic system X carries part of the neutrino energy. The interaction could be mediated by a W boson as well (*charged current* weak interaction, CC)

$$\nu_l + N \to l + X \quad , \tag{1.12}$$

where a charged lepton l is produced according to the flavor of the neutrino in the initial state. The neutrino cross-section for CC is $\sigma \propto E_\nu$ up to $E_\nu \sim 10^3$ GeV. At $E_\nu \sim 10^3$ TeV, $\sigma \sim 10^{-33}$ cm^2 and at higher energies it rises as $\sigma \propto E_\nu^{0.36}$ (Gandhi et al. 1998). The cross-section for CC interaction of ν_μ and $\overline{\nu}_\mu$ is illustrated in Fig. 1.1.

The interaction length in water of a neutrino of 1 TeV is $\lambda \sim 2 \times 10^9$ m, while a γ-ray with the same energy has $\lambda \sim 42$ m. The interaction length for neutrinos becomes equal to the diameter of Earth at $E_\nu \sim 200$ TeV.

The nucleus involved in the interaction is shattered and its fragments start a *hadronic cascade* in the medium. The mean distance travelled by secondary charged particles before further interaction is called *path length*.

1.2.2 Detection principle

The detection principle of neutrinos in the TeV-PeV energy range is based on the collection of the optical photons produced by the Cherenkov effect of secondary relativistic particles.

Cherenkov radiation is emitted when charged particles cross an insulator medium with speed exceeding the speed of light in that medium. The radiation is coherent and it is emitted along a cone of aperture angle

$$\cos \theta_c = \frac{1}{\beta n} \quad , \tag{1.13}$$

where n is the refraction index of the medium and $\beta = v/c$. For relativistic particles ($\beta \sim 1$) in seawater ($n \sim 1.36$), $\theta_c = 45°$.

The *Frank-Tamm Formula* gives the number of Cherenkov photons (N_C) emitted per unit wavelength interval ($d\lambda$) and distance travelled (dx) by a particle of charge e:

$$\frac{d^2 N_C}{d\lambda dx} = \frac{2\pi}{137\lambda^2}\left(1 - \frac{1}{n^2\beta^2}\right) \ , \tag{1.14}$$

where λ is the wavelength of the radiation. According to Eq. 1.14, short wavelengths contribute more significantly than long ones to Cherenkov radiation.

Water and ice at great depths are typically chosen as targets for the interactions of neutrinos in Cherenkov detectors because they are transparent to Cherenkov radiation for wavelengths above 300 nm. The Cherenkov light is then measured by a three-dimensional array of photomultiplier tubes (PMTs) whose quantum efficiency is large in the wavelength range $300 - 600$ nm, matching the region in which water and ice are transparent to light.

An efficient neutrino detector must cover the largest possible area in order to overcome the small neutrino cross-section with matter (see Sec. 1.3). It must as well provide a shield against secondary particles produced by CRs and, at the same time, it must allow the propagation of the Cherenkov light emitted by relativistic particles produced by neutrino interactions.

A comparison between data collected by neutrino detectors built in seawater and under Antarctic ice has started a debate about the relative performance of seawater and ice in the detection of neutrinos (Halzen 2006). It has been stated that the absorption length of ice exceeds 100 m at the dominant blue wavelengths of Cherenkov radiation, while the absorption length in water is only ~ 10 m; therefore ice is more transparent. Absorption reduces the total amount of light arriving on the PMTs, thus ice has a larger effective volume than water. Water has longer scattering lengths than ice, depending on depth and the color of incident radiation. The direction of incoming Cherenkov photons is changed by scattering and, as a consequence, their arrival on the PMTs is delayed. This effect degrades the measurements of the direction of the incoming neutrinos.

Moreover,the presence of an optical background caused by the decay of radioactive elements must be accounted for in seawater. The most abundant radioactive isotope in seawater is ^{40}K and its β decay produces photons in the same wavelength range of Cherenkov radiation. In addition, bioluminescence produced by the steady glow of bacteria and by flashes of animal origin can give origin to an optical background that in some cases outgrows the one due to ^{40}K. Ice, instead, is almost background-free from radiaoctivity and bioluminescence.

1.2.3 The atmospheric background

The interaction of CRs with atmospheric nuclei produces atmospheric muons and neutrinos. The atmospheric neutrino flux and the atmospheric muon flux represent an irreducible background for the detection of cosmic neutrinos. Given their small energy loss across the atmosphere (~ 2 GeV), their relatively long lifetime (2.6×10^{-6} s) and their small interaction cross-section, muons are the most abundant charged particles at sea level: their flux at $E > 1$ GeV is ~ 200 particles/(m^{2}s).

Atmospheric muons and neutrinos are mainly produced by the decay of charged pions and kaons. The quantity of muons and neutrinos is strictly correlated, while their energy distribution differs because of their different masses. The *conventional atmospheric neutrino flux* is obtained by shifting to lower energies the energy distribution of muons and it is measured in cm^{-2}s^{-1}sr^{-1}GeV^{-1}.

In the $1 - 100$ TeV energy range the conventional neutrino intensity can be expressed by a power-law spectrum:

$$\frac{d\Phi_\nu}{dE}(E) \propto E^{-\alpha_\nu^A} \quad , \tag{1.15}$$

where $\alpha_\nu^A \sim \alpha + 1 \sim 2.7$ and α is the measured spectral index for the most energetic CR (see Chap. 2).

At sufficiently high energies (~ 100 TeV), another possible mechanism must be considered for atmospheric muons and neutrino production. The semileptonic decay of charmed mesons ($D^\pm, D^0$) and baryons produces *prompt* atmospheric muons. Since the lifetime of these particles is very short ($\sim 10^{-12}$ s), prompt muons are produced before the parent particle can lose any energy in collisions and they are highly energetic. As a consequence, their spectrum closely follows the CR spectrum, with $\Phi_{prompt} \propto E^{-\alpha}$, $\alpha \sim 3.7$.

The flux of atmospheric muons exceeds the flux of atmospheric neutrino interactions by several orders of magnitude. This effect decreases with increasing detector's depth, as shown in Fig. 1.2. Atmospheric muons represent a major background source, since their wrong reconstruction could mimic high-energy neutrino interaction. The steepening of the spectrum of astrophysical neutrinos at $E \sim 100$ TeV, however, allows a distinction between the two classes of events (see Fig. 1.6).

1.3 Neutrino telescopes

In a large volume neutrino detector, one can distinguish between two main classes of events: events with a long *track* due to a passing muon and events with a *shower*, without the presence of a muon. Some events signature topologies for different neutrino flavors and interactions are shown in Fig. 1.3 .

While the shower occurs for all event topologies, for ν_μ CC interaction only the muon track can be detected, since its path length exceeds that of a shower by several orders of magnitude at $E > 2$ TeV. As a consequence, such an event might be well detected even if the interaction occurs outside the instrumental volume, in the Earth's crust or in the surrounding medium. The properties of a shower, instead, can be extimated only if the interaction takes place inside the instrumented volume.

A cosmic neutrino signal can be identified by a large volume detector using different methods. A first one relies on the observation of an excess of events above a given observed energy. This method is based on the evidence that the expected cosmic signal is harder than the atmospheric neutrino spectrum and it relies on the *calorimetric capabilities* (i.e., efficiency in energetic measurements) of the instrument. It usually works better for shower events, because in this case the majority of the energy is released inside the detector.

The second method is only effective for track-like events: an excess of events in a very small solid angle region $\Delta\Omega$ over the expected background provides evidence for a cosmic signal. This requires good *tracking capabilities* of the instruments and it works for ν_μ events. In this case, the ν_μ's detector is called *neutrino telescope*.

The muon direction, closely correlated to the neutrino direction, can be accurately reconstructed, and since neutrinos are not deflected by magnetic fields, it is possible to trace the muon back to the neutrino source. This is equivalent to traditional astronomy, where photons point back to their sources. Unlike traditional astronomy, however, neutrino telescopes are *downward looking*: this means that the sky visibility of the instrument is limited to the bottom hemisphere. This choice guarantees the reduction of the background of atmospheric μ's.

Neutrino telescopes must have a volume of at least a cubic-kilometer in order to detect cosmic neutrinos. This can be shown by introducing the event rate during the observation time T:

$$\frac{N_\nu}{T} = \int dE_\nu \frac{d\Phi_\nu}{dE_\nu}(E_\nu) A_\nu^{eff} \quad , \tag{1.16}$$

where $\frac{d\Phi_\nu}{dE_\nu}(E_\nu)$ is the differential neutrino energy spectrum in units of $\mathrm{TeV^{-1}cm^{-2}s^{-1}}$ and A_ν^{eff} is the *effective area* of the detector. This latter quantifies the detector response and, if convoluted with the neutrino flux, gives the event rate, as shown in Fig. 1.4.

The effective area depends on the neutrino flavor, on the interaction type, on the neutrino energy and incoming direction, on the state of the detector and on the cuts used for the suppression of background. It can be determined by Monte Carlo simulations.

In order to estimate an analytic expression for A_ν^{eff}, we consider the case of ν_μ

interacting outside the volume of the telescope (Chiarusi and Spurio 2010). The corresponding effective area is

$$A_{\nu\mu}^{eff} = AP_{\nu\mu}(E_\nu, E_\mu^{thr})\epsilon e^{-\sigma(E_\nu)\rho N_A Z(\theta)} \quad , \qquad (1.17)$$

where A is the geometrical projected detector surface measured in cm^2, $P_{\nu\mu}(E_\nu, E_\mu^{thr})$ is the probability that a neutrino with energy E_ν will produce a muon arriving with a residual threshold energy E_μ^{thr} at the detector, ϵ is the fraction of muons of energy E_μ^{thr} that are actually detected and it is a function of the properties of the detector, while the term $e^{-\sigma(E_\nu)\rho N_A Z(\theta)}$ takes into account the absorption of neutrinos crossing along a path $Z(\theta)$ in the Earth.

We assume that for muons arriving at the detector with $E_\mu^{thr} > 1$ TeV, ϵ has a constant value $\epsilon \sim 0.1$. The probability $P_{\mu\nu}$ is obtained by Monte Carlo Simulations and, at these muon energy, is given by $P_{\mu\nu} \sim 1.3 \times 10^{-6}E_\nu^{0.8}$ (Gaisser et al. 1995). For neutrinos arriving from the nadir ($Z(0) = 6.4 \times 10^8$ cm) at $E < 100$ TeV the absorption is negligible, and assuming $A = 1$ km^2, we obtain $A_{\nu\mu}^{eff}(1$ TeV$) \sim 10^3$ cm^2. The number of expected events is ~ 1.5 per year, where the irreducible background has not been taken into account yet. Therefore, a km^3-sized detector is able to collect only a few neutrino interactions per year.

1.4 Running and planned neutrino detectors: an overview

The first activities for the construction of a neutrino detector trace back to 1970s. The main locations chosen for these instruments are the Mediterran Sea and the Antarctic Ice. The first, pioneering collaboration that worked on an experiment at South Pole was AMANDA (the Antarctic Muon And Neuntrinos Detector Array). Holes were practiced in the ice using a hot water drill and strings of optical sensors were lowered there before the water in the holes could freeze again.
These operations started in 1993: the detectors worked as expected and AMANDA detected its first atmospheric neutrinos. In 2005 AMANDA became a part of its successor project, the IceCube Neutrino Observatory (Sec. 1.4.1). The largest neutrino observatory in the Nothern hemisphere is the ANTARES detector. It is located at a depth of 2475 m in the Mediterranean sea and it was completed in 2008. Its position offers a privileged view of some of the most interesting areas of the sky, such as the Galactic centre.

The next generation of neutrino detectors includes IceCube-Gen2, a new, larger observatory that will enable spectral studies, significant point source detections, and new discoveries. In the Mediterrean sea, the next generation of detectors will be housed in KM3NeT, an infrastructure composed of two different structures

located in Italy and France. The telescope will have an instrumented volume slightly larger than that of IceCube.

1.4.1   IceCube

At present, IceCube is the only running km^3-scale neutrino observatory. It was built between 2005 and 2010 and it is located near the Amundsen-Scott South Pole Station (Aartsen et al. 2017a).

The instrumental volume consists in one cubic kilometer of highly transparent Antarctic ice. The detector is buried beneath the surface, at a depth of 2500 m, while a surface array (IceTop) and a denser inner subdetector (DeepCore) significantly enhance the possibilities of the observatory. A side view of IceCube is shown in Fig. 1.5.

The deepest part of the detector is composed of an array of 5160 digital optical modules (DOM). Each DOM is a spherical, pressure resistant glass housing containing a ten-inch photomultiplier tube and the associated electronics. The DOMs are disposed on 86 vertical strings deployed on a hexagonal grid. Each string holds 60 DOMs. The spacing between the strings is 125 m.

The denser sub-array located at the center of the detector, DeepCore, enhances the sensitivity of the detector to lower neutrino energies (down to 10 GeV).

The surface detector IceTop consists of 81 surface stations located on top of the same number of IceCube strings. It was built as a veto and calibrator detector for IceCube, but it also works as a detector for air showers from primary cosmic rays between 300 TeV and 1 EeV. It measures the arrival direction of the cosmic rays as well as their flux and composition.

The track events can be reconstructed by IceCube with a directional uncertainty lower than 1°. The tracks can be ∼km long and an unknown fraction of their energy is deposited outside the instrumental volume. The energy uncertainty is therefore large.

Shower events tend to deposit all their energy in IceCube within ∼ 10 m and this results in a good energy resolution ($\frac{\delta E}{E} \sim$ 15% above 10 TeV, Aartsen et al. (2014a)). The angular resolution is limited, with typical values on the order of $10° - 15°$, Aartsen et al. (2014b).

The datas from all the DOMs are received by the IceCube Data Acquisition system (DAQ) (Aartsen et al. 2017a). The primary trigger for neutrino alerts requires the signal to be seen at least by 8 DOMs in a 5 μs time window. If the trigger is satisfied, the DAQ records all DOMs signal in a +6 μs$/ - 4$ μs around the trigger time into a single event.

The data are then made available to the online processing and filtering system. In this system, several reconstruction algorithms characterize each event's extracted light arrival information against the expected patterns from track and

shower events to determine the direction, position and energy of each event (Aartsen et al. 2017a). Based on the results, $\sim 1\%$ of the events are selected to be potentially of neutrino origin and they are further processed.

The IceCube Neutrino Observatory was built under a National Science Foundation (NSF) Major Research Equipment and Facilities Construction grant. The international IceCube collaboration is responsible for the scientific research program.

1.5 Observed high-energy flux of astrophysical neutrinos

The IceCube Neutrino Observatory has observed a high-energy flux of astrophysical neutrinos at high statistical significance, above the atmospheric background (IceCube Collaboration (2013), Aartsen et al. (2014b) and Aartsen et al. (2016)).

In IceCube Collaboration (2013), a sample of 28 neutrino events with energy between 30 and 1200 TeV was selected from all-sky data collected between 2010 and 2012. The expected events from atmospheric backgrounds were ~ 10. Taking into account the directions, energies and topologies of the events, a 4σ deviation from the atmospheric hypothesis was observed. In Aartsen et al. (2014b) one additional year of data was analyzed and the atmospheric hypothesis was rejected at the 5.7σ confidence level for the three years combined.

These events were selected by requiring the neutrino candidates to be seen primarily inside the detector rather than at the detector boundary. In Aartsen et al. (2016) complementary measurements where the interaction vertex could be placed outside the volume of the detector were included in the analysis. This condition causes a large contribution from atmospheric muons, the field of view was therefore restricted to the Nothern hemisphere. From the analysis of data collected between 2009 and 2015, the presence of a high-energy (194 TeV - 7.8 PeV) neutrino flux was stated, rejecting the atmospherical hypothesis at a 5.6σ confidence level.

The data in Aartsen et al. (2016) are well described by an isotropic, unbroken power-law flux with a spectral index $\gamma = 2.13 \pm 0.13$, as shown in Fig. 1.6.

The arrival directions of all events with reconstructed muon energies above 200 TeV were analyzed, but no correlation with known γ-ray sources was found. In order to achieve multi-messenger observation that would increase the sensitivity to sources over observations in neutrinos alone, the IceCube collaboration began a program of prompt alerts in 2016 (Aartsen et al. 2017b). The purpose of these alerts is to encourage rapid follow-up observations when neutrino events that are likely to have astrophysical origin are detected.

1.5.1 Follow-up observations: IceCube Alerts

The γ-ray, optical and X-ray follow-up program is designed to detect burst of several neutrino-like events that, when considered alone, would be undistinguishable from background. Given the low expected rate of true neutrino bursts, the thresholds are set to generate alerts for a few background over-fluctuations per year.

The IceCube alerts are issued to the observational community both through public and private channels. They are distributed as Gamma-Ray Coordination Network (GCN) notices. Originally, two GCN streams, EHE and HESE, were provided. They have now been replaced by the Gold and Bronze streams.

These selection classify events based on their probability of being of astrophysical origin. The Gold and Bronze alert are defined according to the *signalness* of the event:

$$Signalness = \frac{N_{signal}}{N_{signal} + N_{background}} \tag{1.18}$$

where N_{signal} and $N_{background}$ are the number of signal and total background (both atmospheric muons and neutrinos) above the selection value.

Astrophysical neutrino candidates with a signalness of at least 50% will generate a Gold alert, while a Bronze alert will rise from candidates with a signalness of at least 30%.

The alerts are generated with several candidate neutrino selection methods, each based on the characteristics of different types of events.

The Gamma-Ray Follow Up (GFU) track selection identifies possible neutrino-induced through-going track events from all directions. In the Nothern Sky, the events with the highest muon energy are selected, while in the Southern Sky the selection is based on the deposited charge. These cuts are used to obtain 50%/30% astrophysical purity for the Gold and Bronze selection.

The High Energy Starting (HESE) track selection is aimed at high energy neutrino events whose interaction vertex occurs inside the IceCube instrumented volume. The deposited charged required to obtain 50% or 30% astrophysical purity varies with the declination. The Extremely High Energy (EHE) track selection is particularly sensitive to the PeV neutrinos. It only contributes to the Gold alerts sample.

For Gold alerts, GFU selection information will be primarily used, then the EHE information and finally the HESE information. For Bronze alerts there is no EHE information, therefore the GFU information is used and then the HESE selection.

The minimum angular resolution for automated alerts is 0.2°.

Every GCN notice contains several useful values for the follow-up observations. These are:

- Time and date in universal time, 0.01 s precision;

- The IceCube Run number and Event Number, which is a unique ID in the IceCube collaboration;

- Right ascension and Declination in different epochs (J2000, current and 1950) with 50% and 90% containment angular error radii;

- The *signalness* given by Eq. 1.18;

- The *false alarm rate*, which is the number of events similar to the current alert that would be seen by IceCube per year;

- The likely neutrino energy under the assumption of a diffuse muon neutrino power-law flux $E^{-2.9}$ (best fit value).

The alerts are not expected uniformly in declination. The IceCube backgrounds are dependent from the zenith angle, moreover the absorption of high-energy neutrinos passing from the Earth's core must be considered. The majority of the alerts is expected in the Nothern hemisphere, just above the Equator, as shown in Fig. 1.7.
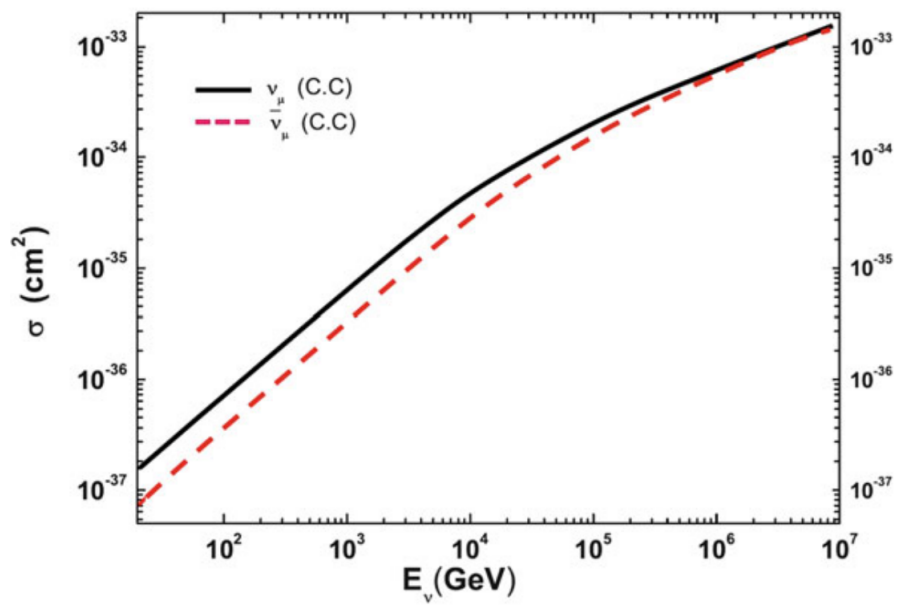
Figure 1.1: Cross-section for ν_μ and $\overline{\nu}_\mu$ as a function of their energy. Credits: Spurio 2018.
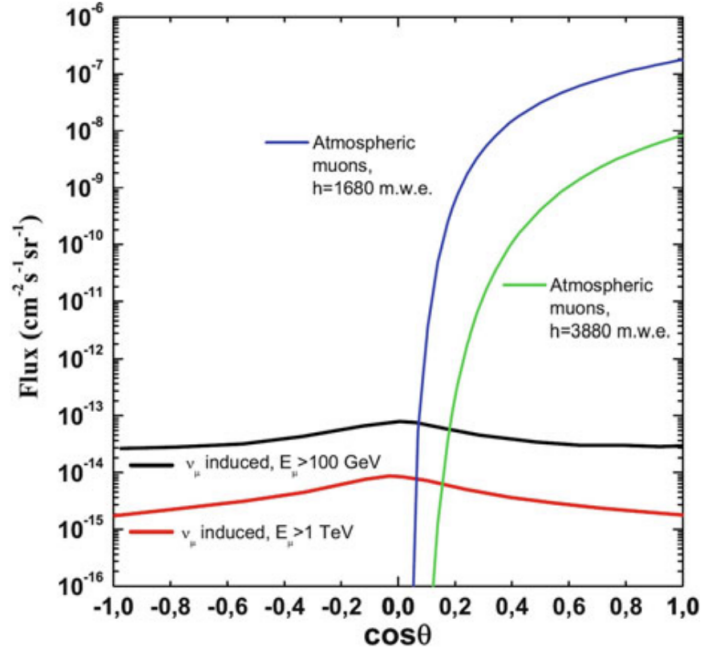
Figure 1.2: Flux as a function of the cosine of the zenith angle θ of atmospheric muons at two different depths and muons induced by CC interactions of atmospheric ν_μ for two different energy thresholds. The heights are expressed in *m.w.e.* units, *meter water equivalent*, a measure for cosmic ray attenuation in underground laboratories. Credits: Spurio (2018).
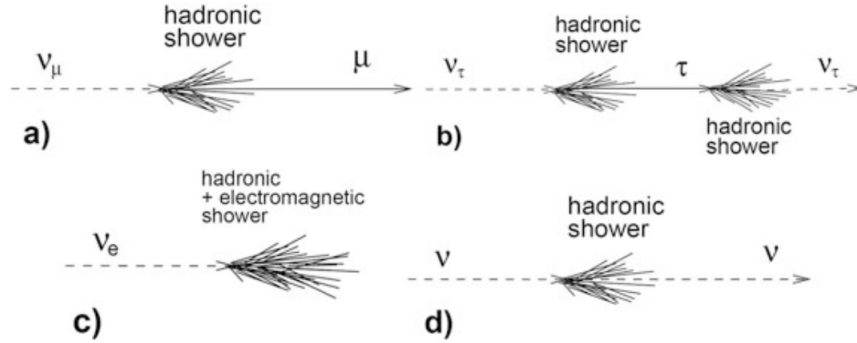

Figure 1.3: (*a*) CC interaction of a ν_μ: a muon and a hadronic shower are produced. (*b*) CC interaction of a ν_τ: a τ and a hadronic shower are produced. The τ decays starting a second hadronic shower (double signature event). (*c*) CC interaction of a ν_e: both a hadronic and electromagnetic shower are produced. (*d*) NC interaction: a hadronic shower is produced. Particles and anti-particles cannot be distinguished in a large volume neutrino detector. Credits: Spurio (2018).
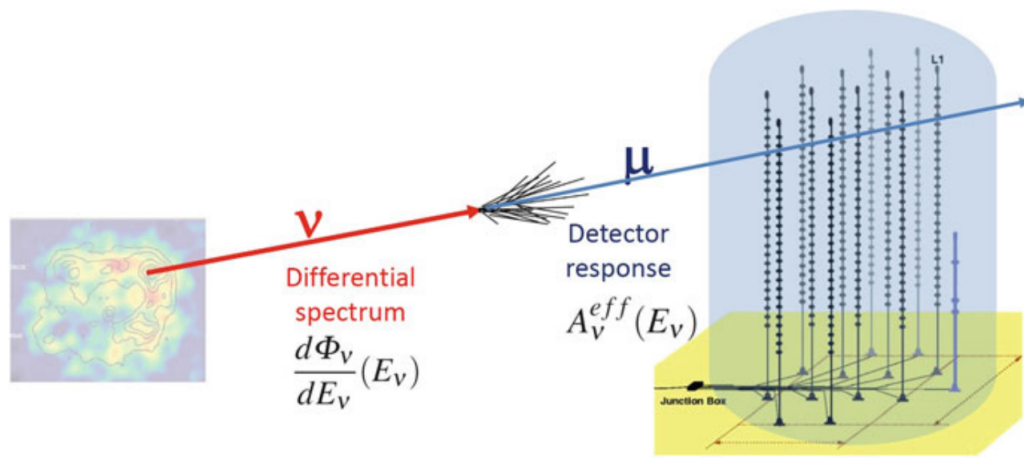
Figure 1.4: The number of events detected by a neutrino telescope is obtained by convolution of the effetcive area and the neutrino flux. Credits: Spurio (2018)
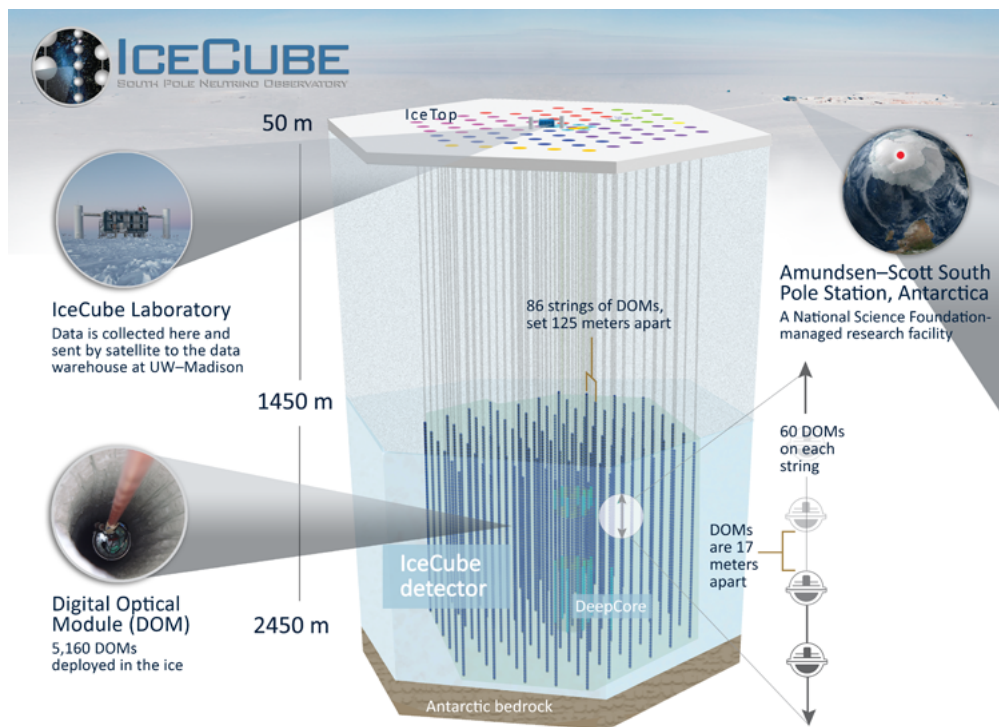

Figure 1.5: A side view of the IceCube Neutrino Observatory. Credits: IceCube.
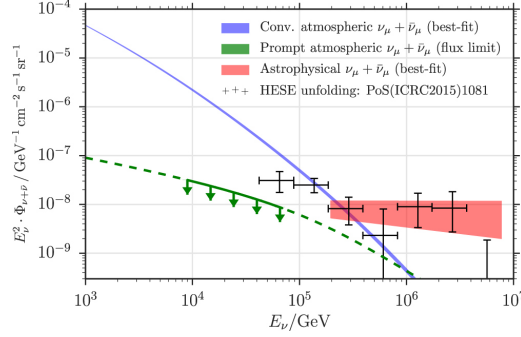
Figure 1.6: Best-fit neutrino spectra from Aartsen et al. (2016) for the unbroken power-law model, $\Phi_\nu = N_0(E_\nu/(100 \text{ TeV}))^{-\alpha}$. The width of the red line shows the effects of varying both N_0 and α within one sigma of the best fit values, $N_0 = 0.9^{+0.30}_{-0.27}$ and $\alpha = 2.13 \pm 0.13$. The green line represents the upper limit on the prompt atmospheric model, while the blue line is the best-fit for the conventional atmospheric neutrino flux.

Figure 1.7: Alert declination distribution for Gold and Bronze alerts. The expected astrophysical neutrinos from starting and through-going tracks and the atmospheric background are shown. The Bronze selection also includes events of the Gold selection. Credits: Ice Cube Collaboration.

Chapter 2

Astrophysical sources of high-energy neutrinos

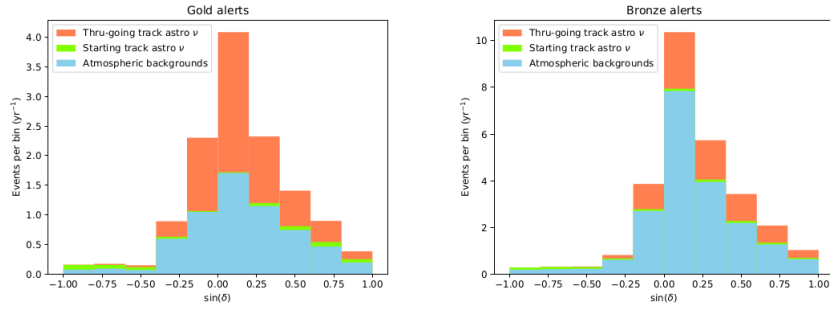Cosmic rays are high-energy nuclei, mostly protons, produced in astrophysical environments and arriving on Earth. We do not know where they come from or how they are accelerated to extreme energies exceeding 10^8 TeV.

While lower-energy photons can travel to us from the farthest corners of the Universe, the highest energy photons and cosmic rays are attenuated after short distances, obscuring our view of the most energetic cosmic events. In contrast, the Universe is transparent to neutrinos, making them suitable probes of the high-energy sky (see Fig. 2.1).

The isotropic arrival direction of astrophysical neutrinos indicates an extragalactic origin. Indeed several models have been proposed, including galaxies with intense star formation, core of AGN, low-luminosity AGN, quasar-driven outflows, blazars, low-power gamma-ray bursts (GRBs), choked GRBs, cannonball GRBs, intergalactic shocks, galaxy clusters, tidal disruption events, or cosmogenic neutrinos (Ahlers and Halzen 2018a). However, the observed match between the energy density of cosmic neutrinos and the extragalactic γ-ray background observed by *Fermi* (see Sec. 2.1) as well as the association of an IceCube event with the blazar TXS 0506+056 has focused the attention of the astrophysical community on AGN with the jet pointing to the Earth.

2.1 Connection between UHECR, γ-rays and high-energy neutrinos

The quest for the origin of high-energy neutrinos is thought to be linked to the problem of the sources of ultra high-energy cosmic rays (UHECR).

UHECR are cosmic rays with $E > 10^{19}$ eV. They are associated with the

structure of the CR spectrum above this energy threshold, the *ankle*, marked in Fig. 2.2.

As for high-energy neutrinos, it has been assumed that UHECR have an extra-galactic origin. This is linked to the evidence that above the *ankle* the gyroradius[1] of a proton is larger than the size of the Galaxy disk. As a consequence, the particles in UHECR are not confined in our Galaxy by the magnetic field.

The theoretical upper limit on the energy of cosmic rays from distant sources is given by the *Greisen-Zatsepin-Kuzmin cutoff* (GZK). This effect takes into account the interactions between UHECR and the Cosmic Microwave Background (CMB), which causes the loss of energy through the resonant pion production illustrated in Eq. 1.4a and Eq. 1.4b. Therefore, protons above 10^{19} eV are not able to travel distances greater than a few Mpc. This limits the existence of standard UHECR emitters to our local super-cluster of galaxies (Chiarusi and Spurio 2010). The pion decay will produce an additional neutrino flux above 5×10^{18} eV, called the GZK or cosmological neutrinos.

High-energy cosmic rays produce γ-rays and neutrinos interacting with photons or nuclei. Targets include strong radiation fields that may be associated with the accelerators as well as any concentrations of matter or molecular clouds in their vicinity with photons. In the acceleration sites, neutrinos are produced from the decay of charged pions (see Sec. 1.1), while γ-rays arise from the decay of neutral pions. While neutrinos escape their sources without further interaction, γ-rays would be absorbed by the Extragalactic Background Light (EBL) and give rise to electromagnetic cascades at lower energies as they interact with photons from the CMB. As a consequence, despite neutrinos being accompanied by pionic γ-rays when they are produced, the γ-rays will appear at lower energies. As discussed in Sec. 1.1, neutrinos and pionic photons need accelerated hadrons (CRs) to be produced.

Considering that γ-rays and neutrinos carry, on average, 1/2 and 1/4 of the energy of the parent pion, respectively, Ahlers and Halzen (2018a) showed that the production rates of neutrinos, Q_{ν_α} (GeV^{-1} s^{-1}) and of pionic γ-rays, Q_γ can be easily related to the rate of production of charge and neutral pions, respectively.

Given a ratio of charged-to-neutral pions $K_\pi = \pi^0/\pi^\pm$, a simple (but powerful) relation between the pionic gamma-ray and neutrino production rates can be obtained:

$$\frac{1}{3} \sum_\alpha E_\nu^2 Q_{\nu_\alpha}(E_v) = \frac{K_\pi}{4} (E_\gamma^2 Q_\gamma(E_\gamma)) \ .$$

The ratio of charged-to-neutral pions depends on the target of the cosmic rays.

---

[1]The gyroradius is the radius of the circular orbit of a charged particle in presence of a uniform magnetic field. It is defined as $r_g = \frac{mv}{qB}$, where m is the mass of the particle, v is its speed, q is the charge and B the intensity of the magnetic field.

The value of K_π is $K_\pi \sim 2$ for a gas (*pp* interactions) environment and $K_\pi \sim 1$ for a photon (*pγ*) filled environment. These considerations allow to link CRs, γ-rays and neutrinos. An example is well illustrated in Fig. 2.3. Under the assumption is that the $\pi^0/\pi^\pm$ production is due to CRs and gas interaction (i.e. $K_\pi \sim 2$), the initial emission spectrum of photons and neutrinos (dashed blue line) from pion decay is almost identical to the spectrum of cosmic rays ($\propto E^{-\Gamma}$).

The γ-ray model (solid blue line) is strongly attenuated at $E > 100$ GeV by interactions with EBL in order to match the Fermi observations. The γ-ray background (blue data) allows also to provide an upper limit for the high-energy cosmic neutrino flux (dashed blue line). The agreement between model and data is quite convincing. The observed neutrino flux above 100 TeV is very close to the corresponding upper limit (dashed blue line), which would imply a large contribution of the underlying (neutrino) source population to the γ-ray background. It is however noticeable that the HESE neutrino data in Fig. 2.3 are only marginally consistent with this upper limit (Ahlers and Halzen 2018b).

The green solid line represents a model of UHECR protons able to account for the most energetic cosmic rays (green data) (Ahlers and Halzen 2018b). Assuming CRs to be trapped in their sources by magnetic fields, they can interact with gas and produce γ-rays and neutrinos. This mechanism can be so efficient that the total energy of CRs is converted, imposing an upper limit on the contribution of UHECRs in neutrino production known as *calorimetric limit* or *Waxman-Bahcall* (WB) upper limit. The observed neutrino flux saturates the calorimetric limit.

The UHECR model in Fig. 2.3 predicts a flux of GZK cosmogenic EeV neutrinos (dotted green line) which could probe the fraction of UHECRs at $E > 10^{19}$ eV.

The interplay between UHECRs, γ-rays and neutrinos shows that a pre-condition for a source to be a VHE neutrino emitter is being source of VHE cosmic rays as well (Mészáros 2017). Given the role of γ-rays, the diffuse isotropic γ-ray background detected by *Fermi* can put severe constraints on models.

2.2 Candidate extragalactic neutrino sources

This work focuses on the role of blazar-type AGN as candidate neutrino emitters. Therefore, event though several astrophysical objects and phenomena have been proposed as possible sources, such as galaxy groups and clusters, starburst galaxies, Gamma Ray Bursts and Tidal Disruption Events, the following section will discuss in detail the properties of AGN and their contribution to the diffuse neutrino flux detected by IceCube.

2.2.1   AGN

We define *Active Galactic Nuclei* (AGN) the engines of a small fraction of galaxies (about a few) whose strong, multi-wavelength emission is powered by accretion onto a central supermassive black hole (SMBH). AGN can have luminosities up to 10^{48} erg/s and they can be classified as radio quiet (RQ) AGN and radio loud (RL) AGN. The latter class shows luminous jets, detected mostly in radio band but also in γ-rays, X-rays and optical bands, and they are roughly 15-20% of all AGN (Urry and Padovani 1995).

The structure of an AGN is inherently axisymmetric, as illustrated in Fig. 2.4. The infalling matter onto the central SMBH loses angular momentum in an accretion disk, while clouds of gas rapidly moving in the potential of the black hole produce broad emission lines in optical and ultraviolet bands (*broad line regions*). Along some lines of sight, the radiation is obscured by a *torus* of dust and gas. At larger distances, narrower emission lines are produced by slower moving clouds (*narrow line region*). The collimated radio jets may be originated by outflows of energetic particles along the poles of the disk and they may be relativistic or non-relativistic (Urry and Padovani 1995).

Those AGN whose relativistic jet is viewed at a small angle with respect to the line of sight are called *blazars* (Urry and Padovani 1995). Depending on their behaviour in the optical band, they can be divided in two subclasses: Flat Spectrum Radio Quasars (FSRQ) and BL Lacertae objects (BL Lacs). While the former display strong emission features in their optical spectrum, the latter show at most weak optical emission lines and they are completely featureless in many cases.

In Giommi (2012) a simple scenario has been proposed were the appearence of the optical spectrum, and therefore the classification of blazars, is the result of three main optical processes: a non-thermal, jet-related one; a thermal one related to the accretion disc and the emission from the host galaxy.

The radiation from blazars spans the entire electromagnetic spectrum and it is composed of two humps. The first one is due to synchrotron radiation, while the second one is thought to be produced by Inverse Compton (IC) or hadronic processes. The position of the first peak ranges between $\sim 10^{12.5}$ Hz (~ 0.01 eV) and $\sim 10^{18.5}$ Hz (~ 13 keV), while the high-energy emission may be extended to several TeV and it reaches its maximum between $\sim 10^{20}$ Hz (~ 0.4 MeV) and $\sim 10^{26}$ Hz (~ 0.4 TeV) (Giommi et al. 2012).
Depending on the position of the synchrotron peak, blazars can be divided in three categories (Abdo et al. 2010b) (see Fig. 2.5):

- *LSP*, Low Synchrotron Peaked blazars, whose synchrotron peak is located in the far-IR or IR, at $\nu^S_{peak} < 10^{14}$ Hz;

- *ISP*, Intermediate Synchrotron Peaked blazars, where the synchrotron emission peaks at 10^{14} Hz $< \nu^S_{peak} < 10^{15}$ Hz;

- *HSP*, High Synchrotron Peaked blazars, whose peak reaches the UV band or higher energies, being located at $\nu^S_{peak} > 10^{15}$ Hz.

When referring to BL Lacs, we talk of LBL ($\nu^S_{peak} < 10^{14}$ Hz), IBL (10^{14} Hz $< \nu^S_{peak} < 10^{15}$ Hz) and HBL ($\nu^S_{peak} > 10^{15}$ Hz) (Padovani and Giommi 1995).

Blazars were the earliest suspected cosmic ray accelerator candidates. The ideal sites for accelerating protons are the termination shocks of the jets and internal shocks within the jets. These galaxies could therefore be sources of UHECR, energetic γ-rays and VHE neutrinos.

In Padovani et al. (2015a) the cumulative neutrino emission from BL Lacs was calculated via Monte Carlo simulations in order to assess if it is possible for BL Lacs as a class to explain the IceCube detections. It was found that BL Lacs as a class could explain the neutrino background (NBG) at $E > 0.5$ PeV while their contribution is less than 10% at lower energies. For more details on the role of blazars as possible neutrino emitters, see Sec. 3.
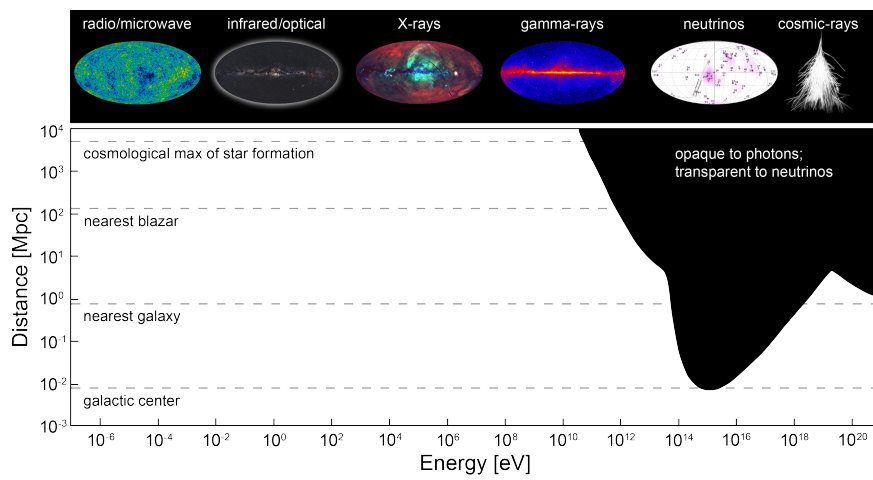
Figure 2.1: Photons absorption versus distance horizon. The Universe is opaque above ~ 100 TeV. While neutrinos travel unimpeded basically across the Universe, harder photons are stopped at various distances due to the media they encounter. Credits: IceCube Collaboration.
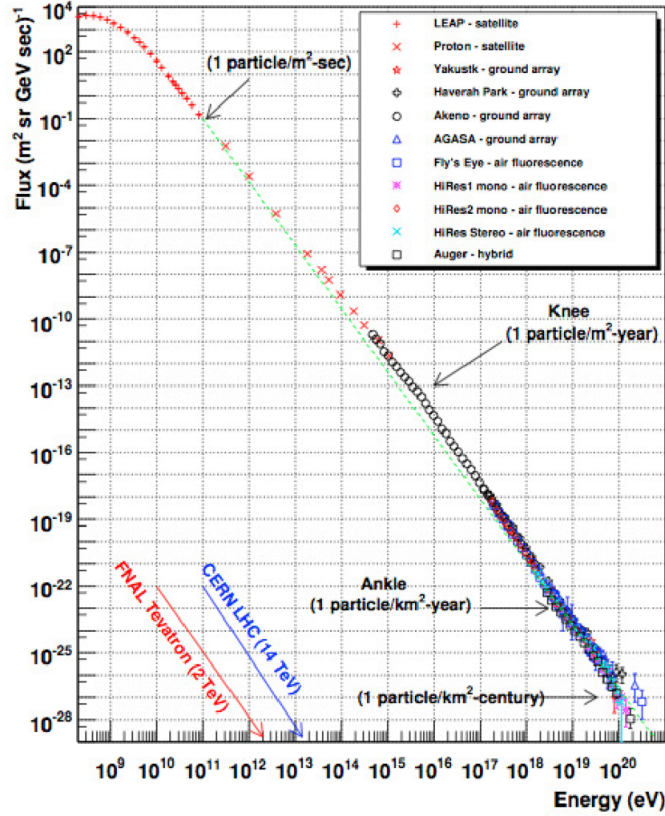
Figure 2.2: Cosmic rays spectrum measured by different experiments. Two transition point are clearly visible, the *knee* ($E > 10^6$ GeV) and the *ankle*($\sim 10^{10}$ GeV). The spectrum can be described with three power-law models. Below the knee, the differential spectral index of the cosmic-rays flux is $\alpha \sim 2.7$, while above the knee it becomes steeper, $\alpha \sim 3.1$. Above the *ankle* the spectrum flattens again. The red and blue arrows mark the energies reached by the largest human-built experiments. Credits: López-Oramas (2015).

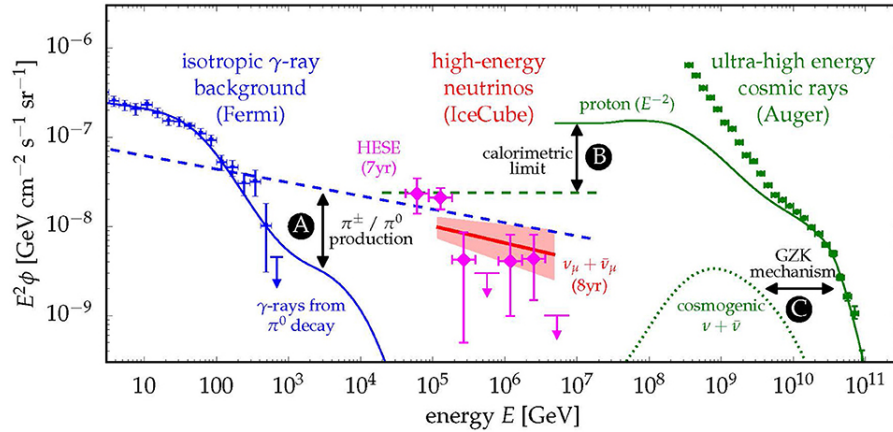Figure 2.3: The spectral flux of neutrinos inferred from the 8-year upgoing track analysis by IceCube and the HESE analysis (magenta data) compared to the flux of unresolved extragalactic γ-ray sources (blue data) and UHECRs (green data). Various multimessanger processes are highlighted: **(A)** The joint emission of neutrinos (dotted blue line) and γ-rays (solid blue line) after the decay of $\pi^{\pm}$ and π^{0}. **(B)** An upper limit on neutrino production (dashed green line) can be imposed by UHECRs emission models (solid green line). **(C)** The UHECRs model predicts a flux of GZK neutrinos in the EeV energy range (dotted green line). Credits: Ahlers and Halzen (2018b).
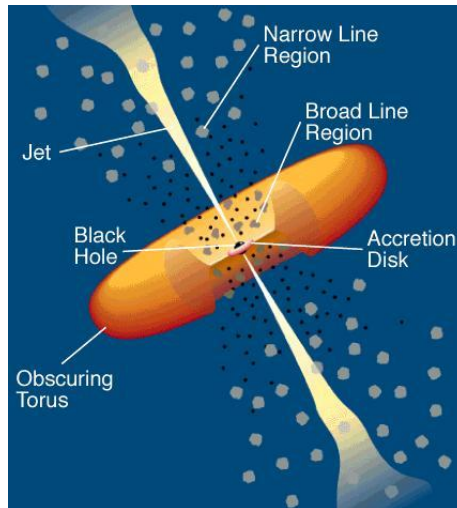
Figure 2.4: AGN Model. The SMBH is surrounded by an accretion disk. The Narrow Line Region and the Broad Line Region are featured. An obscuring torus of dust and gas may prevent the radiation from reaching the observer along some lines of sight. Credits: (Urry and Padovani 1995).
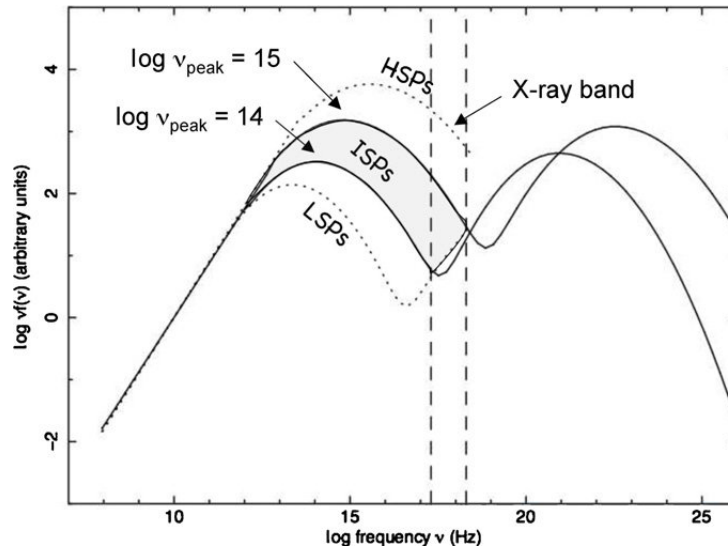
Figure 2.5: Definition of three different blazar classes (High Synchrotron Peaked, Intermediate Synchrotron Peaked and Low Synchrotron Peaked) based on the position of the synchrotron peak (ν_{peak}^S) in their SED. The X-ray frequency range ($\sim 10^{17} - 10^{19}$ Hz) is marked by dashed vertical lines. Credits: Abdo et al. (2010b).

Chapter 3

Blazars as candidate neutrino emitters

This thesis aims at investigating the role of blazars in the production of astrophysical neutrinos. This chapter will therefore contain a review of the current literature on the topic, with a focus on the case of TXS0506+056, which was found to be the counterpart of the neutrino event IceCube170922A at the 5.2σ confidence level.

3.1 Origin of the high-energy emission in blazars

Several models are usually invoked in order to interpretate the high-energy hump in the SED of blazars (see Sec. 2.2.1).

3.1.1 Leptonic models

A common explanation attributes high-energy emission to Inverse Compton (IC) scattering of soft target photons on the synchrotron electrons responsible for the low-energy peak. These target photon fields may have different origin and they may vary with the position along the jet.

In the *one zone leptonic scenario* the emission region (a blob) is assumed to be spherical and it moves along the jet with a specific Doppler factor. In BL Lacs objects, featuring very weak or absent emission lines, the target photons are thought to be the low-energy synchrotron photons produced inside the jet (Synchrotron Self-Compton (SSC) model, see e.g. Bloom and Marscher (1996)). In this picture the two humps are produced by the same electron population.

In FSRQs, having jets that propagate in an environment rich of photons, the second hump can be due to external IC processes with, for example, photons emitted by the accretion disk, reflected from the broad line region (Sikora et al. 1994) or

coming from from a dusty torus (Ghisellini and Tavecchio 2009).

These models, that have succeeded in explaining stationary SEDs of blazars, are challenged by the observation of minute-scale γ-ray variability and TeV emission. The requirements for producing such variability in relativistic blazar jets have been analyzed by Begelman et al. (2008). The most stringent condition is the evidence that the γ-rays must escape their emitting regions without being absorbed in $\gamma\gamma$ pair production[1]. By imposing $\tau_{\gamma\gamma} \leq 1$, where $\tau_{\gamma\gamma}$ is the opacity of the emitting region, the required bulk Lorenz factor should be extremely large, $\Gamma \geq 50$. This value is much higher than the Doppler factors of $\Gamma \sim 10$ typically inferred from superluminal motion speeds observed in radio Very Long Baseline Interferometry (VLBI) monitoring observations of blazars. This discrepancy is sometimes referred to as the Doppler-factor crisis.

As a consequence, more complex scenarios for leptonic models have been proposed. In *multi-zone models*, the low-energy component and the high-energy component are thought to be produced in different regions. An example is the *spine-sheath model* (Tavecchio and Ghisellini 2008a), where the jet is supposed to be structured, with a fast spine surrounded by a slower sheath. The existence of such velocity structure has an impact on the observed properties of blazar jets: both components will see the emission of the other amplified because of the relative speed. This effect contributes to the total energy density and the total Inverse Compton emission is enhanced. A structured jet offers a good opportunity to reproduce rapid TeV variability states without invoking the stringent $\Gamma \geq 50$ condition: assuming the spine to be a very compact region, also called the *needle*, inside the jet, the value of $\Gamma \geq 50$ required by the models would regard only this region, while the normal jet would be responsible by the emission observed most of the time. As a consequence, the total power necessary to reproduce the observed emission does not exceed that carried by the normal jet (Tavecchio and Ghisellini 2008b).

3.1.2 Hadronic models

The high-energy component could also be explained by *hadronic models* where the radiative output of hadrons accelerated in the jets is considered. Radiative emission from hadrons, mostly protons, can occur either through proton synchrotron emission (Aharonian 2000) or via pp interactions or $p\gamma$ interactions as illustrated in Sec. 1.1.

---

[1] γ-rays crossing a sufficient luminous and compact source can produce electron-positron pairs if their energy is ≥ 511 keV. The $\gamma\gamma$ optical depth can be written as: $\tau_{\gamma\gamma} \sim 0.12 n(\epsilon)\epsilon\sigma_T R$, where ϵ is the energy (in units of $m_e c^2$) of target photons with number density n(ϵ) and R=ct$_{var}\delta(1+z)^{-1}$ is the source dimension as deduced by the γ-ray variability (Svensson 1987; Celotti et al. 1998).
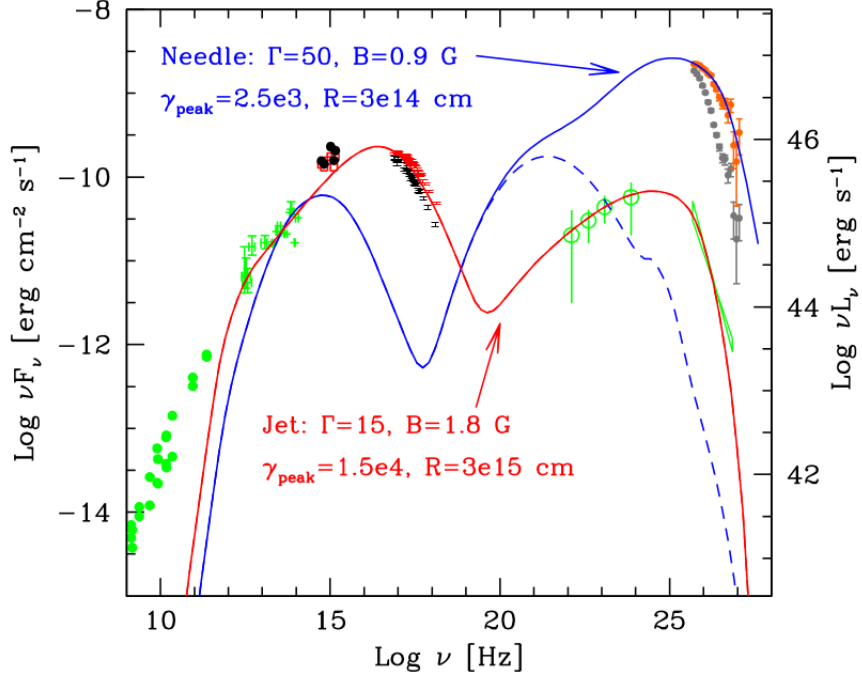
Figure 3.1: Example of needle-jet structure applied to the SED of the blazar PKS 2155-304. Red points compose the TeV spectrum. The dashed line represents the flux produces by the *needle* if the radiation energy density produced by the rest of the jet is neglected. Credits: Tavecchio and Ghisellini (2008b).

In both cases, protons should be accelerated to energies $E_p > 10^{19}$ eV in order to contribute significantly to the radiative output. If we consider that protons should be confined in their emitting regions ($R \sim 10^{15}$ cm), the required magnetic field is $B > 30$ G (Böttcher et al. 2013). The energy density of these magnetic fields would be dominant over the energy density of external radiation fields: as a consequence, one of the most successful hadronic models is the *proton-synchrotron* blazar model, where the same radiation field emitting the synchrotron radiation is the target photon field for $p\gamma$ production.

Proton Synchrotron Model

The idea of a population of accelerated protons and higher-Z nuclei added to the electron population in blazar jets was first proposed in Mannheim (1993) and it was broadly studied afterwards. As for electrons, the proton energy distribution is defined as a power-law function.

The main radiative process in this model is the emission of synchrotron radia-

tion from protons, which is proposed as the origin of the high-energy component in the SED of blazars. The peak of the low- energy, synchrotron emission in blazar's SED can be obtained as

$$\nu^S_{peak} = \frac{e}{2\pi m_e c} B \gamma^2_{break} \frac{\delta}{1+z} \quad \text{Hz} , \qquad (3.1)$$

where B is the magnetic field, γ_{break}, is the Lorentz factor which satisfies $\tau_{syn}(\gamma) = \tau_{ad}(\gamma)$[2], z is the redshift of the source and δ is the Doppler factor (Cerruti 2020).

By replacing the mass of the electron with the proton mass, a peak frequency around 10-100 GeV can be obtained. This is consistent with the observed SEDs of HBLs by assuming $\delta \sim 10 - 50$ and $B \sim 10 - 100$ G. These values of B are roughly 10^3 higher than required by the SSC solution.
The proton-synchrotron model requires a larger number of parameters compared to the SSC model due to the additional parameters of the proton distribution. As a consequence, the model is degenerate and it can constrain only some regions in the parameter space (Cerruti 2020).

Moreover, in order to fit the data proton-synchrotron models require a high proton density which, when expressed in terms of L_p, gets very close to L_{Edd}, the Eddington luminosity of the central SMBH.

Proton-Photon interactions

The presence of a proton population in the jets of blazars implies proton-photon interaction and meson production as described in Sec. 1.1. As a consequence, neutrinos, photons and e^+e^- pairs would be injected in the emitting region.
In particular, photons from the π^0 decay would trigger an electromagnetic cascade. The same process stems from electrons and positron from the decay of charged pions: the synchrotron radiation of these secondary particles would be emitted in the PeV range, thus starting another electromagnetic cascade.

Although $\mu^\pm$ are not stable leptons (their mean lifetime is ~ 2.2 μs, their synchrotron emission could contribute to the radiative output from the source.
The exact computation of the energetic distribution of all secondary particle involved in these processes is a complex numerical task and it can only be performed via Monte Carlo simulations (Cerruti 2020).

The *Bethe-Heitler pair production* is a competitive process with photo-meson production:

$$p + \gamma \rightarrow e^+e^- \qquad (3.2)$$

This process is dominant for low-energy protons, but at energies above the threshold for pion production, $E > 145$ MeV, photo-meson production takes over.

---

[2]$\tau_{syn}(\gamma)$ is the synchrotron cooling time scale, while $\tau_{ad}(\gamma)$ is the adiabatic time scale and it is associated with the expansion of the emitting region as it travels along the jet, $\tau_{ad} \sim R/c$.

It was shown that the radiative signature of Bethe-Heitler pair production may be observable in the SED of blazars as a predicted 'bump' between hard X-rays ($E > 40$ keV) and soft γ-rays ($E < 40$ MeV) (Petropoulou and Mastichiadis 2014).

Lepto-hadronic models

Models were the high-energy emission is due to secondary leptons produced in $p\gamma$ interactions are usually referred to as *lepto-hadronic*.

In these solutions, the radiative output from proton-synchrotron radiation is suppressed by requiring $B < 1$ G. The emission from secondary leptons would emerge in the X-rays as a Bethe-Heitler component and in the TeV band as a photo-meson component. This kind of solutions are typically more promising in terms of neutrino output than pure hadronic models.

3.2   Blazar-neutrino connection

The connection between IceCube events and high-energy emission from blazars has been widely investigated since the diffuse high-energy neutrino flux was discovered (see Sec. 1.5).

In Padovani and Resconi (2014) a sample of 18 IceCube events at $E > 60$ TeV whose interaction vertex is located inside the detector was selected. The counterparts of these events were looked for in the available all-sky catalogues covering the highest-possible energies: TeVCat (Wakely and Horan 2008), the Wise High Synchrotron Peaked (WHSP) catalogue (Arsioli et al. 2015) and the first *Fermi*-Large Area Telescope catalogue of sources detected above 10 GeV (1FHL) (Ackermann et al. 2013). The connection between neutrinos and astrophysical objects was investigated with an *energetic diagnostic*: a hybrid photon-neutrino SED was constructed by deriving the flux per neutrino event assuming that the observed flux is spread over 1 dex in energy and that the spectrum is $f(\nu) \propto \nu^{-1}$ (Fig. 3.3).

The source was considered to be a possible counterpart if a simple extrapolation succeeded in connecting the highest γ-rays to the neutrino. This was performed both for blazars and galactic sources. Possible counterparts were suggested for 9/18 neutrino events and they resulted to be mostly HSP BL Lacs and two Pulsar Wind nebulae (PWNe).

These results lead to further investigation in the field of BL Lac-PeV neutrino connection. In Petropoulou et al. (2015) the interaction of electrons and protons with the magnetic field and with secondary particles leads to a system where five stable particles populations are at work: protons, losing energy via synchrotron radiation, Bethe-Heitler pair production and photo-meson interactions; electrons, photos, neutrons, produced in proton-photon interactions and able to escape al-
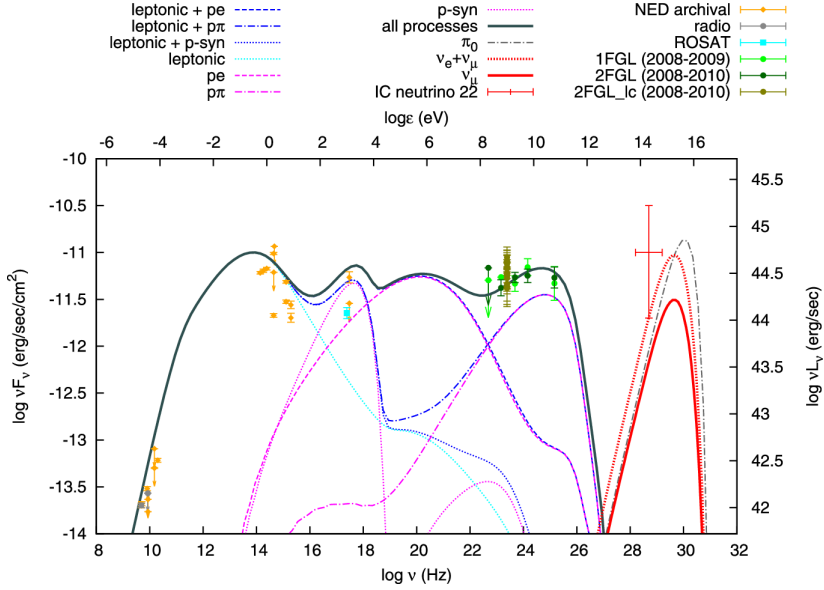
Figure 3.2: SED of the blazar 1H 1914194 and the neutrino flux for the corresponding IceCube event. Contributions from different emission processes are displayed in different colors. The model-predicted neutrino flux is within the 1σ error bar of the observed neutrino flux. Credits: Petropoulou et al. (2015).

most unimpeded by the source region, and neutrinos, able to escape completely unimpeded.

This lepto-hadronic model was applied to six BL Lacs selected in Padovani and Resconi (2014): the neutrino signal was therefore predicted by fitting the individual SEDs of BL Lacs. In five cases out of six, the model-predicted neutrino flux is within the 3σ error bars of the IceCube events and in one case the flux was within the 1σ error bar.

Subsequently, BL Lacs as a class have been analyzed as a candidate emitter for IceCube events in Padovani et al. (2015b). Here, the authors aimed at calculating the cumulative neutrino emission of all BL Lacs within the leptohadronic scenario for their γ-ray emission. The results lead to believe that BL Lacs as a class can explain the neutrino background at high energies (> 0.5 PeV) but they contribute for less than 10% at lower energies. Individual BL Lacs, however, can still make a contribution at a $\sim 20\%$ level at low energies.

Further investigation on this subject was pursued in Padovani et al. (2016). Here, a sample of HESE neutrino events from the first four years of IceCube activity was selected according to two criteria: an energy $E > 60$ TeV and a median angular error $\leq 20°$. The counterparts were looked for in 2FHL (Ackermann et al. 2016) and in 2WHSP (Chang et al. 2017), the *Fermi* 3LAC (Ackermann

et al. 2015) catalogue was also searched for its size and all-sky coverage. In order to study more quantitatively the possible connection between neutrinos and their counterparts, the observable N_ν is introduced. It represents the number of neutrino events with at least one γ-ray counterpart within the median angular error region. The chance probability of observing a certain N_ν for sources above a certain flux was then considered following different randomization procedures. Consistently with Padovani and Resconi (2014), HBL were found to be the only plausible counterparts of at least some of the IceCube events, with a p-value[3] of $0.4 - 1.3\%$ for the three catalogues. These values are dependent on the γ-ray flux and on the *figure of merit*, a quantification of the detectability of the source in the TeV band by the current generation of Imaging Atmospheric Cherenkov telescopes. The predictions of Padovani et al. (2015b) on the impact of blazar emission in IceCube data were also confirmed. These results tend to indicate that, in order to be a neutrino source, a blazar needs to be a strong VHE source with $\nu_{peak}^{S} > 10^{15}$ Hz.

The debate on the role of blazars as high-energy neutrino emitters has been fueled by observations from the AGILE γ-ray satellite (Tavani 2009) as well. In Lucarelli et al. (2017), the search for the γ-ray counterpart of the HESE IceCube event IceCube-160731A is reported. An excess above 100 MeV between one and two days before the neutrino event was found with a significance of 4σ. A possible common counterpart for the transient γ-ray event and the neutrino was proposed: its key features are associated to the HBL class; the lack of evidence for a flaring source in the multi-wavelength coverage, however, prevented identification (Lucarelli et al. 2017).

3.2.1   The case of TXS 0506+056

In 2017 a turning point in neutrino astrophysics occurred: the neutrino event IceCube-170922A was found to be coincident in arrival time and direction with an enhanced γ-ray activity from the blazar TXS0506+056 at redshift $z = 0.3365 \pm 0.0010$ (Paiano et al. 2018).

The event was reported on September 22nd, 2017 as a part of the EHE selection (see Sec. 1.4.1). Its most probable energy was estimated to be 290 TeV, with a 90% confidence level lower limit of 183 TeV (IceCube Collaboration et al. 2018a). Its significance was reported to be 56.5%. The event display is shown in Fig. 3.4.

On September 28th, it was reported by the *Fermi*-LAT collaboration that the event was consistent with the known γ-ray source TXS 0506+056 in a enhanced

---

[3]In a statistical test, the *p-value* is defined as the probability of obtaining the same results or less likely results than those observed during the test under the assumption that the null hypothesis is correct.
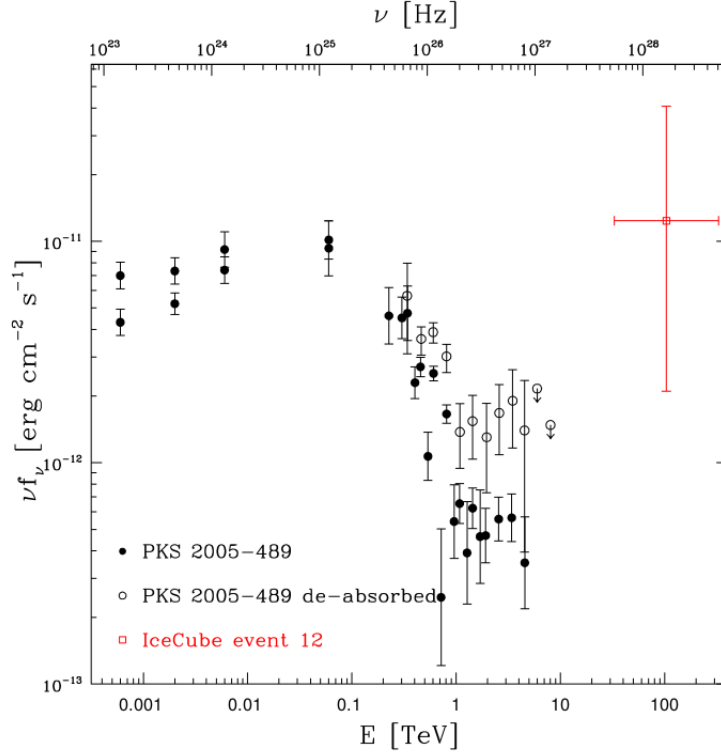
Figure 3.3: Example of a *hybrid* γ-ray SED for the blazar PKS 2005-489. The red square represents the neutrino flux for the corresponding IceCube event. The black filled circles are observed data, while the black open circles are corrected for absorption by the EBL. Credits: Padovani and Resconi (2014).

state of emission. The best fit reconstructed direction of the event was at 0.1° from the position of the blazar (Tanaka et al. 2017).

Multi-wavelength observations

The enhanced γ-ray activity of TXS0506+056 had started in April 2017. Following the announcement of its spatial coincidence with IceCube-170922A, an extensive multi-wavelength campaign on this source started, ranging from radio to γ-rays.

The integrated γ-ray flux of TXS0506+056 above 0.1 GeV, averaged over all Fermi observations spanning 9.5 years in the 3LAC catalog (Ackermann et al. 2015), is $7.6 \pm 0.2 \times 10^{-8}$ cm^{-2}s^{-1}. This flux is consistent with the observations of the AGILE γ-ray telescope. The FAVA (Fermi All-Sky Variability Analysis) light curve at energies above 800 GeV showed an increased flux in the time period following the event. Indeed, the Fermi-LAT flux from 2017, September 15$^{\text{th}}$ to September 27$^{\text{th}}$ was $3.6 \pm 0.7 \times 10^{-7}$ cm^{-2}s^{-1}, roughly a factor of six larger than

the 3LAC flux.

The VHE emission from the source was inspected by several Imaging Atmospheric Cherenkov Telescopes: H.E.S.S., VERITAS and MAGIC. Over 13 hours of observation, MAGIC detected a variable VHE signal at energies above 400 GeV corresponding to a 6.2σ excess over the background (IceCube Collaboration et al. 2018a). The very-high energy observations can be used to infer an upper limit on the redshift of the source as well, taking into account the limits on the attenuation of the VHE flux due to the interaction with the Extragalactic Background Light. The result is consistent with the measured redshift.

Radio observations were performed by the Karl G. Jansky Very Large Array (VLA) in the frequency range 2-12 GHz in six epochs, from October 5th 2017 to November 21st 2017. The source was detected significantly in all bands and epochs. The flux was relatively constant until October 24th, when a slight brightening below 4 GHz was reported. On November 21st, the data indicate a $\sim 20\%$ brighter source below 6 GHz. Spectral steepening at higher frequencies was present as well. The source is also being monitored by the long-term blazar monitoring program of the Owens Valley Radio Observatory (OVRO) (15 GHz) and the light curve shows an increase in radio emission during the 18 months before the neutrino alert (IceCube Collaboration et al. 2018a).

Optical observations were made by several facilities: the All-Sky Automated Survey for Supernovae (ASAS-SN), the Liverpool Telescope, the Kanata Telescope, the Kiso Schmidt Telescope, the high resolution spectrograph on the Southern African Large Telescope (SALT) and the X-SHOOTER instrument on the Very Large Telescope (VLT) (IceCube Collaboration et al. 2018a). The flux of the source in the V band was noticed to be the highest observed in recent years.

In the X-rays, a *Swift* monitoring campaign was initiated and a single NuStar observation was requested. *Swift* found that the strong increase of flux observed at VHE correlates well with the increasing X-ray emission in the same period of time. The spectrum of TXS0506+056 in the X-rays is compatible with the sum of two power-law spectra, a soft one with index -2.8 ± 0.3 in the band covered by *Swift* (0.3 to 10 keV) and a hard component with index 1.4 ± 0.3 in the band covered by NuStar (3 to 79 keV). The NuStar component can be extrapolated to 20 GeV and it connects with the plateau component detected by *Fermi*-LAT (0.1-300 GeV), while the spectral index between 80 and 400 GeV can be inferred from MAGIC observations and it is $\gamma = -3.9 \pm 0.4$. This provides a mostly complete and contemporaneous picture of the source emissions from 0.3 keV to 400 GeV, as shown in Fig. 3.5.
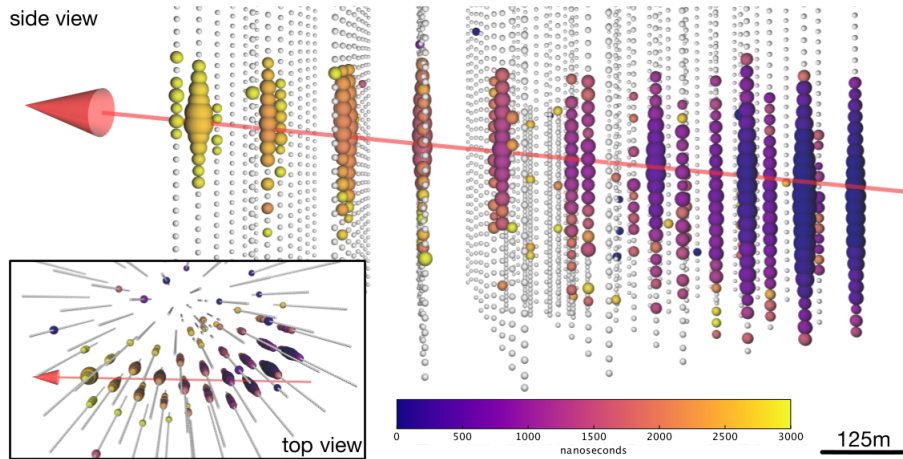
Figure 3.4: Event display for IceCube-170922A. The color reflects the time at which each DOM recorded a signal. The total time spent to cross the detector is ~ 3000 ns. Credits: IceCube Collaboration et al. 2018a.
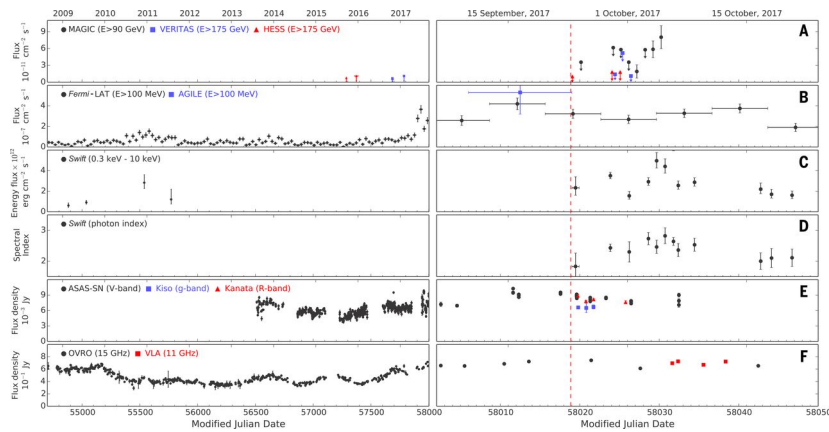

Figure 3.5: Time-dependent multi-wavelength observations of TXS 0506+056 before and after IceCube-170922A. The red dashed line marks the arrival time of IceCube-170922A. On the left, measurements between August 22nd, 2008 and September 6th, 2017 are shown, while on the right an expanded scale from September 6th, 2017 to October 24th, 2017 is displayed. Credits: IceCube Collaboration et al. (2018a).

Association of TXS 0506+056 with IceCube-170922A

Data obtained from the multi-wavelength analysis were used to constrain the chance coincidence probability of the event: the likelihood that a neutrino alert like IceCube-170922A is correlated by chance with a flaring blazar was then cal-
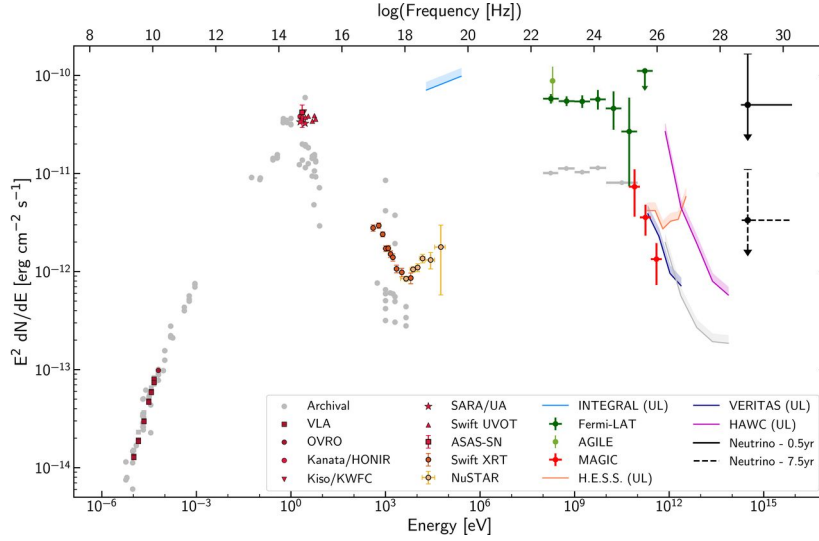
Figure 3.6: Broadband spectral energy distribution for TXS 0506+056, based on observations performed within 14 days of the detection of the IceCube-170922A event. Archival observations in gray illustrate the historical flux level in the radio-to-keV range and in the γ-ray band. The SED displays a double-hump feature typical of blazars. The first peak is located in the optical-UV range and the second in the GeV range. Credits: (IceCube Collaboration et al. 2018a).

culated. No *a priori* model was selected, while several models for the neutrino emissions were considered in the *a posteriori* analysis. The common assumption was that at least part of the γ-rays are produced in the same hadronic interactions where neutrinos have their origin.

The first model considered (model 1) assumed a linear correlation between neutrinos and γ-ray flux: this makes neutrinos more likely to be produced during periods of strong and hard γ-ray emission. The second model (model 2) considers the neutrino flux to be dependent more on variations in γ-ray flux than on its average: in this scenario, even a faint γ-ray source could be considered a neutrino parent source if a time coincidence with the event is present. The third and last model (model 3) considers a correlation between neutrino flux and VHE flux.

A likelihood ratio test was performed for each model. According to the model 1, chance coincidence for the neutrino-blazar correlation is disfavoured at the 3σ level. Following this association, a search in 9.5 years of IceCube archive data was performed in order to look for excess emission at the position of TXS 0506+056 (IceCube Collaboration et al. 2018b). An excess was found in one of the six time periods that make up the whole data-taking period of IceCube.

In the 2012-2015 time period, 13 ± 5 events were found to be above the expected atmospheric background. The significance of this excess was calculated to

be 3.5σ (IceCube Collaboration et al. 2018b). After this period, the next most significant excess includes IceCube-170922A.

During the 2014-2015 neutrino activity, no γ-ray accompanying flaring counterpart was observed from the position TXS 0506+056, while enhanced γ-ray activity was seen from the neighbouring blazar PKS 0502+049. The region around IceCube-170922A was therefore dissected in time, space and energy in Padovani et al. (2018b). It was found that, although PKS 0502+049 contaminates the γ-ray emission at low energies, TXS 0506+056 dominates the high-energy sky above a few GeV: the source is in a low, hard γ-ray state during the neutrino flare, which could be interpreted as a hint that it has undergone a hadronic flare. This supports the picture in which TXS 0506+056 is the only counterpart of all neutrino emissions in the region (Padovani et al. 2018b).

Models for the origin of the neutrino emission

After the discovery, TXS 0506+056 has been extensively studied in order to understand the origin of the neutrino emission. The SED of the source (Fig. 3.6) shows the double hump typical of blazars and its synchrotron peak is $\nu_{peak}^{S} \leq 10^{15}$ Hz, which places it in the HBL/IBL category. The spectral steepening observed at ~ 100 GeV by MAGIC confirms the internal $\gamma\gamma$ absorption mechanism that is expected as a consequence of $p\gamma$ production of a 290 TeV neutrino (Ansoldi 2018). The optical spectrum features three weak emission lines, [O II] 3727 Å, [O III] 5007 Å, [N II] 6583 Å, with equivalent widths (EWs) ranging between 0.05 Å and 0.17 Å. According to the empirical definition ($EW < 5$ Å), TXS 0506+056 is therefore a BL Lac. Nonetheless, the objects classified as BL Lacs because of their weak optical emission lines can be divided in two categories: intrinsically weak-lined objects and heavily diluted broad-lined sources. The latter have been called *masquerading BL Lacs* in Giommi et al. (2013) and they are actually quasars: they constitute the missing FSRQ population that peaks at high ν_{peak}^{S}. These objects are High Excitation Galaxies (HEG) and they show radiatively efficient accretion at high Eddington rates ($0.01 \leq L/L_{Edd} \geq 1$): this is associated to a standard geometrically thick but optically thin disk accretion flow. In Padovani et al. (2019), TXS 0506+056 is claimed to be a masquerading BL Lac, based on its radio power, its optical spectrum and its Eddington rate, $L/L_{Edd} \geq 0.04$.

The energy of the parent proton for the production of an event with $E_\nu = 290$ TeV by $p\gamma$ interaction is $E_p \sim 6$ PeV, which sets the corresponding threshold for target photons to

$$\epsilon \sim \frac{m_\pi m_p c^4}{E_p} \sim 440 \text{ eV} \quad , \tag{3.3}$$

in the UV/soft X-ray band (Ansoldi 2018).

Different models have been tested to reproduce the flaring state of TXS 0506+056. *Hadronic models* would allow the most optimistic scenario for neutrino production, but they are shown to be problematic in explaining both the observed SED and the neutrino emission. With a pure hadronic modeling, indeed, the synchrotron X-ray emission by secondary electrons would overshoot the observed flux (Gao 2019). The *proton synchrotron* model could explain the HE emission from the source, but it would predict a maximum $0.1 - 10$ PeV neutrino flux of $\epsilon_\nu F_\nu \sim 10^{-15}$ erg cm^{-2}s^{-1}, which yields a very low probability for IceCube neutrino detection ($\sim 0.085\%$), as independently found in Cerruti et al. (2018) and Keivani et al. (2018).

Hybrid models where leptonic emission constitute the bulk of the observed flux and hadronic processes contribute as strongly as it is allowed by data are therefore taken into consideration. In these scenarios, the proton synchrotron peak is hidden below the other components and hadrons are allowed to reach lower energy than in purely hadronic models. Moreover, a higher proton density is predicted, which leads to a higher neutrino flux peaking at lower energies (Cerruti et al. 2018).

In Gao (2019), the coincidence of a neutrino with the flare from TXS 0506+056 is interpreted in terms of enhanced injection rate of cosmic nuclei and electrons in the radiation zone. According to the time-dependence of the SED of the source, the high-energy peak of TXS 0506+056 is thought to be due to a SSC mechanism, hence a one-zone scenario is adopted. This model predicts ~ 0.27 neutrino events with $E_\nu > 120$ TeV during the flare. From the GeV-TeV light curve, the flare lasted one year and a half, which leads to a $> 10\%$ probability to actually detect a neutrino.

A single-zone, lepto-hadronic solution is presented in Cerruti et al. (2018) as well. Neutrino rates of $0.3 - 6.4$ yr^{-1} are found. These values are higher than Gao (2019) and this could be due to the different approaches used to constrain the parameter space. The size of the emitting region is constrained to be 10^{16} cm and is thought to be located at a sub-parsec distance from the central engine.

A conciliation between the two kinds of models is sought in Sahakyan (2018), where the tight requirements for hadronic emission are softened by the assumption of the interaction of the jet with a dense target, thus illustrating an internal shock scenario. The results are still compatible with lepto-hadronic models, which could be still responsible for the X-ray emission.

The two scenarios - hadronic and lepto-hadronic - could be distinguishable with studies on the variability of the source: in the hybrid model a strong correlation between the low-energy bump and the high-energy one is expected, while delays between variations in the two components are predicted to occur in hadronic models due to different acceleration and cooling time scales.

The assumption of a single-zone model puts severe constraints on the opti-

cal depth of the emitting region, which could be alleviated by the adoption of multi-zone models. In Ansoldi (2018) a jet-sheath scenario is presented for TXS 0506+056. While earlier studies on this model focused on leptonic emission, here the theory is extended in order to account for hadronic radiative processes. The maximum predicted proton energy ranges between 10^{14} eV and 10^{18} eV and the neutrino production rates are in agreement with the detection of a single neutrino during the period of enhanced γ-ray emission.

The role of Radiatively Inefficient Accretion Flows (RIAFs)[4] in neutrino emission from TXS 0506+056 has been analyzed in Righi et al. (2018). Assuming the source to be a BL Lac, RIAF would be expected to be a dominant accretion mechanism onto the central SMBH. RIAFs could therefore serve as external radiation fields for $p\gamma$ interactions and their role appears to be stronger moving from HBL to LBL objects.

The classification of the TXS 0506+056 is however an open theme, as stated in Padovani et al. (2019). If the source is actually a FSRQ, the presence of a BLR would influence the location of the γ-ray emitting region and the neutrino output.
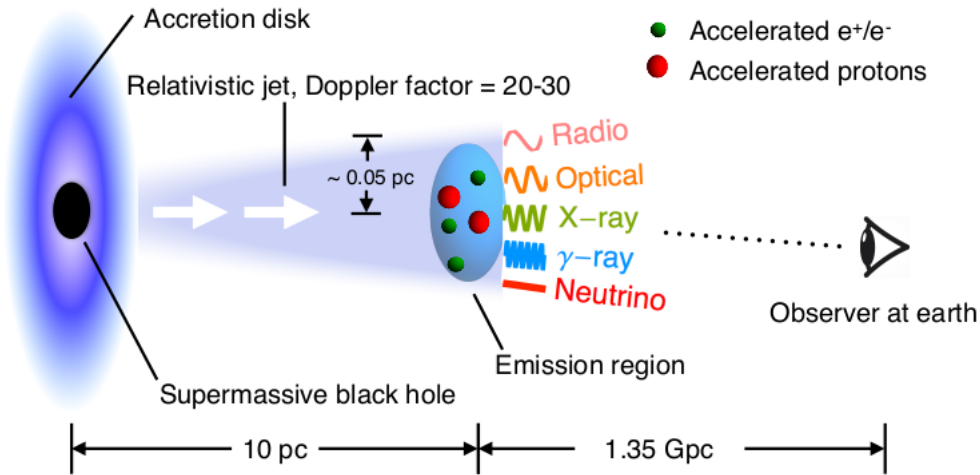

Figure 3.7: Illustration of the emission region of TXS 0506+056 travelling at relativistic speed. The physical sizes of the various objects are not drawn to scale. Credits: Gao (2019).

---

[4]In AGN,when the Eddington accretion rate is lower than the viscosity parameter α^2, defined as the ratio of the orbital period of the gas to its inflow time, accretion onto the SMBH can be radiatively inefficient because the cooling time of the gas is longer than the inflow time (Quataert 2004).

3.3   Impact of the discovery on further studies

Despite appearing as a unique case in the quest for blazar-neutrino connection, the case of TXS 0506+056 has motivated further research in the field. In Franckowiak et al. (2020), a multi-wavelength approach was used in order investigate possible coincidences between *Fermi*-LAT blazars and IceCube events with $E \sim 100$ TeV. Three particularly interesting sources were identified: the Seyfert I radio loud galaxy 1H 0323+342, the high-redshift BL Lac MG3 J225517+2409 and the bright FSRQ PKS 1502+106. The latter is associated to IceCube-190730A and its connection with this event has been subject of further analysis in Rodrigues et al. (2020). Despite being in a low-activity γ-ray state at the neutrino arrival time, the OVRO light curve of the source displays evidence of a radio outburst that reached its maximum during the arrival of the neutrino. A similar increase in the radio emission observed by OVRO was shown by TXS 0506+056, which strengthens the assumption that PKS 1502+106 could be a neutrino emitter.

For a study of coincidence between blazar flares and neutrino emission, the work of Halzen et al. (2019) is particularly noticeable. Here, a model for the neutrino flaring activity of TXS 0506+056 in 2014 has been proposed, starting from the hypothesis that a subclass of blazars with the same characteristics of this source could account for the diffuse neutrino flux observed by IceCube. The all-sky neutrino flux from a class of episodic neutrino emitters with density ρ and neutrino luminosity L_ν is calculated as

$$\sum E_\nu^2 \frac{dN_\nu}{dE_\nu} = \frac{1}{4\pi}\frac{c}{H_0}\xi_z L_\nu \rho F \frac{\Delta t}{T} \quad , \tag{3.4}$$

where F is the fraction of sources episodically emitting flares of duration Δt over a total observation time T and ξ_z is a factor of order unity that parameterizes the integration over the redshift evolution of the sources.
In Halzen et al. (2019) the calculation was made for a density of BL Lac objects of 1.5×10^{-8} Mpc^{-3} and with the parameters of the 2014 neutrino flare from TXS 0506+056, $\Delta t \sim 110$ days, $T \sim 10$ yr, $L_\nu = 1.2 \times 10^{47}$ erg/s. The flux on the left side of Eq. 3.4 is the IceCube neutrino flux (Sec. 1.5). It results $F \sim 0.05$: it means that a special class of blazars that undergo a ~ 110 days neutrino flare every 10 yr could explain the IceCube neutrino flux.

From the relation between the cosmic neutrino flux and the flux of cosmic rays (see Sec. 2.1), it follows that the optical depth of the protons in the photon targets must be $\tau_{p\gamma} > 0.4$ (Halzen et al. 2019). This high efficiency requirement is consistent with the hypothesis that only a special class of sources with high photon density is responsible for the production of the high-energy neutrino flux seen by IceCube.

The large value $\tau_{p\gamma}$ indicates that the source must be opaque to high energy γ-rays, as illustrated by means of the relation between $\tau_{p\gamma}$ and $\tau_{\gamma\gamma}$:

$$\tau_{\gamma\gamma} \sim \frac{\eta_{\gamma\gamma}\sigma_{\gamma\gamma}}{\eta_{p\gamma}\sigma_{p\gamma}}\tau_{p\gamma} \quad , \tag{3.5}$$

where $\sigma_{\gamma\gamma} \sim 6.65 \times 10^{-25}$ cm^2 is the $\gamma\gamma$ cross section and $\sigma_{p\gamma} \sim 0.7 \times 10^{-28}$ cm^2 is the $p\gamma$ cross section and $\eta_{\gamma\gamma} \sim 0.1, \eta_{p\gamma} \sim 1$ are the efficiencies for both processes. The result is $\tau_{\gamma\gamma} \sim \mathcal{O}(100)$ (Halzen et al. 2019). As a consequence, it is impossible for the VHE pionic γ-rays to leave the source: they would lose energy inside the source before interacting with the EBL and cascading to lower energies. Therefore, we do not expect to witness γ-ray flaring activity, which is consistent with the γ-ray emission from TXS 0506+056 during the 2014 neutrino flare.

3.3.1 The aim of this thesis

This thesis aims at investigating deeply the temporal coincidence between IceCube events and γ-ray emission from *Fermi* blazars.

The study was performed on a sample of blazars (HBLs, IBLs and LBLs) selected in Giommi et al. (2020) that had been found to be spatially coincident with a selection of IceCube events (Sec. 5.1). In this work, sources were matched with *Fermi* 4FGL counterparts and their γ-ray activity was inspected on various time scales (6 months, 3 months and 1 month) centered on each neutrino arrival time. The bin size was chosen in order to inspect increasingly short time scales around the neutrino event: 7 days for the 6-months light curves, 3 days for the 3-months light curves and 2 days for the 1-month light curves. The light curves were built performing a full binned likelihood analysis in each bin. The analysis method is discussed in Sec. 5.2. The same light curves were built for TXS 0506+056 as a reference.

In Chap. 6, we inspected each light curve by means of a N parameter defined as as the percentage ratio of detections with $TS > 9$ for each light curve. After observing that most of the 3-months and 1-month light curves show $N \sim 0$, we furtherly studied the 6-months light curves with a variability index following Angioni (2019). On the basis of the results obtained for TXS 0506+056 ($N > 50\%$ and $> 3\sigma$ variability), a subsample of 4 *TXS-like* sources, all LBLs, was selected as *flaring* blazars. Due to different statistic, HBLs and IBLs are considered *flaring* when at least 2 detections are found in the one-month interval centered on the event in the 6-month light curves. Two sources (a HBL and a IBL) were subsequently selected. The subsample of 6 flaring blazars thus obtained is discussed in detail in Appendix A.

A *flare-neutrino coincidence* was defined as the occurrence of a neutrino event in the 7-days interval centered on a detection. Out of the 6 selected flaring blazars, 4 display a coincidence in the 6-months light curves with 7-days binning.

Finally, the significance of the observed temporal coincidences has been assessed using a statistical analysis. Following the results of Giommi et al. (2020), where the spatial coincidence between the classes of HBLs/IBLs and their neutrino counterparts was found to be significant at the 3.56σ confidence level, the class of HBLs/IBLs and LBLs were treated separately.

The results and future perspectives are discussed in Chap. 7.

Chapter 4

Gamma-Ray analysis

4.1 The Fermi Gamma-Ray Space Telescope

The γ-ray light curves analyzed in this thesis were built utilizing data released to the scientific community by the Fermi collaboration[1]. A brief introduction about the Fermi Gamma-Ray Space Telescope and data reduction will therefore be presented in this section.

The NASA's Fermi Gamma-Ray Space Telescope is a powerful γ-ray observatory which observes light in the photon energy range between 0.8 keV and 300 GeV. The mission was launched on June 11th, 2008. An artist concept of the Telescope is shown in Fig. 4.1.

Fermi is in a 565 km altitude orbit with an inclination of 25.6°.The orbit has a period of $\sim$ 96 minutes, and its pole precesses about the celestial pole with a period of $\sim$ 53.4 days. At this inclination, the telescope spends about 15% of the time inside the South Atlantic Anomaly (SAA), where science data taking is suspended because of the high flux of trapped particles.

The Telescope carries two instruments: the *Large Area Telescope* (LAT), which is the primary instrument, and the *Gamma-Ray Burst Monitor* (GBM). The LAT's field of view covers about 20% of the sky at any time and scans continuously, covering the whole sky every three hours. The Gamma-ray Burst Monitor complements the LAT for observations of high-energy transients. It has a field of view several times larger than the LAT and provides spectral coverage that extends from the lower boundary of the LAT down to 10 keV. The performances of the two instruments are compared in Fig. 4.2.

In this work, data from LAT were considered; the features of this instrument will therefore be discussed in details. The information about LAT is mainly se-
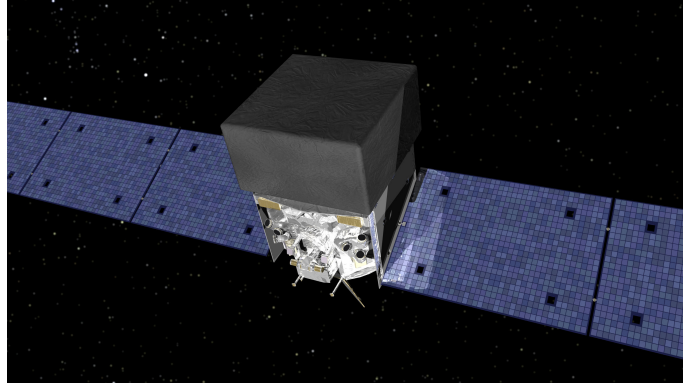
---

[1]https://fermi.gsfc.nasa.gov/cgi-bin/ssc/LAT/LATDataQuery.cgi.

Figure 4.1: Artist concept of the Fermi Gamma-Ray Space Telescope. Credits: NASA.

lected from Atwood et al. (2009) and.

	Fermi-LAT	GAMMA-400
Orbit	Circular, 565 km	Highly elliptical, 500-300000 km (without the Earth's occultation)
Operation mode	Sky-survey (3 hours)	Point observation (up to 100 days)
Source exposition	1/7	1
Energy range	20 MeV - 300 GeV (γ, e)	~20 MeV - 1 TeV (γ) 1 GeV - 10 TeV (e)
Effective area (E_γ > 1 GeV)	~6500 cm^2 (total) ~4000 cm^2 (front)	~4000 cm^2
Coordinate detectors - readout	Si strips (pitch 0.23 mm) digital	Si strips (pitch 0.08 mm) analog
Angular resolution	~4° (E_γ = 100 MeV) ~0.2° (E_γ = 10 GeV) ~0.1° (E_γ > 100 GeV)	~2° (E_γ = 100 MeV) ~0.1° (E_γ = 10 GeV) ~0.01° (E_γ > 100 GeV)
Calorimeter - thickness	CsI(Tl) ~8.5 X_0	CsI(Tl) + Si ~25 X_0
Energy resolution	~10% (E_γ = 10 GeV) ~10% (E_γ > 100 GeV)	~3% (E_γ = 10 GeV) ~1% (E_γ > 100 GeV)
Proton rejection factor	~10^3	~5x10^5
Mass, kg	2800	4100
Telemetry downlink volume	15 Gbytes/day	100 Gbytes/day

Figure 4.2: Overview of the LAT and GBM characteristics.

4.1.1   The Large Area Telescope (LAT)

The LAT is a pair conversion telescope which consists of four main subsystems: a tracker, a calorimeter, an anti-coincidence detector and a data acquisition system. These four modules work together in order to reject spurious signals induced by cosmic rays and detect γ-rays from astrophysical sources.

The tracker/converter (TKR) consists of 18 layers of paired x–y silicon strip detector planes with interleaved tungsten foils, which promote pair conversion and

measure the directions of incident particles. The first 12 paired layers are arranged to immediately follow converter foils, which have a thickness of $\sim$3% of a radiation length of tungsten. In the subsequent four layers the tungsten converters are ~ 6 times thicker; these layers are referred to as the thick or back section. The last two layers have no converter. The front section allows to optimize the angular resolution at low energy; the back section maximizes the effective area at the expense of the angular resolution (at 1 GeV) for photons converting in that region.

The calorimeter (CAL) is composed of CsI(Tl) scintillation crystals stacked in eight layers and provides energy measurements as well as some imaging capability. It also helps in rejecting cosmic rays, since their pattern of energy deposition is different than for γ-rays. The anticoincidence detector (ACD) rejects CR backgrounds.

For every γ-ray that enters in the LAT, in fact, there are $10^5 - 10^6$ charged particles produced by the interaction of CRs with our atmosphere. The ACD is made of special plastic tiles that produce flashes of light when a charged particle hits them. It surrounds the other modules so that, if no alert is given by this system, the signal detected in the other modules can indeed be considered a γ-ray. The ACD is 99.97% efficient.

The Data Acquisition System (DAQ) collects information from the other three modules and makes the distinction between background signal from cosmic rays and real γ-ray signal. It is made of specialized electronics and microprocessors.

The structure of LAT is shown in Fig. 4.3. When a γ-ray enters the LAT, it first passes through the Anticoincidence detector without producing a signal, then it goes through conversion foils and the tracking detectors. It will interact via pair conversion in one of the tungsten sheets, and the paths of the resulting electron and positron will be tracked by the silicon strips. The energy of the secondary particles is then measured in the calorimeter.

4.1.2 LAT Performances

Data downlinked from the Fermi spacecraft (Level 0 data) are reprocessed to produce the Level 1 data. In particular, the interaction of the event in the LAT in the various parts of the instrument are reconstructed from the signal and the type of event (e.g., astrophysical photon) identified. Relevant physical parameters (e.g., direction, energy) are then associated to each event.

The classification of the events is based on their probability of being photons and the quality of their reconstruction. The events are separated into event classes with each class characterized by its own set of instrument response functions. Events within a class are subdivided into event types that use selections based on individual event topologies (for instance whether an event is converted in the Front or Back section of the Tracker).
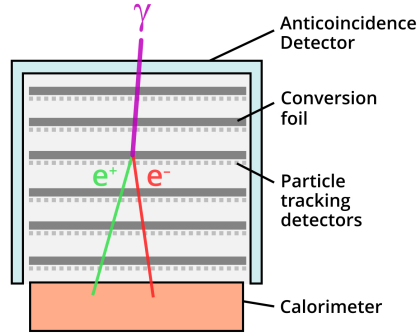
Figure 4.3: Cross-section of the LAT instrument on board the Fermi Gamma-Rays Space Telescope. The tracking detectors are made of silicon-strips alternated with tungsten sheets which serve as conversion foils. The anticoincidence detector filters out charged particles from CRs that could be mistaken for γ-rays. The calorimeter performs energetic measurements. Credits: NASA's Goddard Space Flight Center.

The event-level analysis software has been periodically updated and for this reason the LAT community has provided several data releases that, for historical reasons, are called *Passes*. The first Pass, Pass 6, was released at launch, while the current pass is Pass 8 (Atwood et al. 2013).

The current event classes are a nested hierarchy in which the higher probability photon selections are subsets of the less restrictive selections. Higher probability photon selections have smaller effective areas, narrower point spread functions (PSF), and lower contamination from background events.

The loosest selection criteria (the TRANSIENT classes in Pass 8) are designed for short-duration events, such as gamma-ray bursts, and timing studies that benefit from increased photon statistics while tolerating a higher background fraction and broader PSF. An intermediate selection (SOURCE class in Pass 8) provides lower background contamination at the expense of lower effective areas (in particular, at low energies) and is most favorable for analysis of moderately extended sources and point sources on medium to long timescales. The most restrictive selections (in Pass 8: the ULTRACLEANVETO or the SOURCEVETO classes) are ideal for analysis of large regions being characterized by a background rate 5-20% lower than the background rate of SOURCE class below 10 GeV, and 50% lower at 200 GeV.

Each event class has a corresponding set of response functions that are unique to that class. The response functions for each class are internally partitioned into FRONT and BACK conversion types related to the two tracker sections (thin and thick, as described above). The PSF for FRONT events is approximately a factor

of two better than the PSF for BACK events.

In order to correctly evaluate the spectra of astrophysical γ-ray sources, we need to know the LAT performance that is described by the Instrument Response Functions (IRFs). To evaluate the LAT response, a dedicated Monte Carlo simulation is performed. A large number of gamma-ray events are simulated in order to cover all possible photon inclination angles and energies with good statistics. This is based on the best available representation of the physics interactions, the instrument, and the on-board and ground processing to produce event classes. The comparison between the properties of the simulated events within a given event class and the input photons gives the instrument response functions.

The IRF is the product of three terms:

- Effective area, $A_{eff}(E, v, s)$, the product of the cross sectional geometrical collection area, γ-ray conversion probability, and the efficiency of a given event selection (denoted by s) for a gamma ray with energy E and direction v in the LAT frame (see Fig. 4.5).

- Point-spread function (PSF), $P(v', E, v, s)$, the probability density to reconstruct an incident direction v' for a γ-ray with (E, v) in the event selection s.

- Energy dispersion, $D(E, E', v, s)$, the probability density to measure an event energy E for a γ-ray with (E, v) in the event selection s.

Given a distribution of γ-rays $S(E, p)$ coming from a celestial direction (p) of the sky, the distribution of the observed photons $M(E', p', s)$ is

$$M(E', p', s) = \iiint S \times A_{eff} \times P \times D dt d\Omega dE$$

.

The effective area (A_{eff}) is the projected area of the detector multiplied by its efficiency, defined as the probability that a photon will interact in the detector and pair-produce. P is the Point Spread Function (PSF) of the instrument and it reflects the performance of the instrument in measuring the photon direction. D is the energy dispersion and reflects how well the instrument measures the photon energy. All three parameters depend on s, the event selection.

The source model $S(E, p)$ contains contributions from the point sources, from Galactic and Extra-Galactic diffuse sources and from the other sources in the field of view.

The integrals are over the time range of interest for the analysis, the solid angle in the LAT reference frame and the energy range of the LAT.

The set of IRF used in Pass 8 event analysis is called P8R3_V3, which has been optimized for the study of point-like sources and the production of the fourth LAT source catalog (4FGL, see. Sec. 4.1.4).

In the P8R3_V3 response functions the PSF, defined as the likelihood to reconstruct a γ-ray with a given angular deviation, is derived entirely from Monte Carlo (MC) simulations.

At low energies ($<$ GeV) the PSF is determined by multiple scattering. If multiple scattering were the only contribution to the PSF, it should become narrower as E^{-1}. The PSF, instead, improves more slowly with energy, as $\sim E^{-0.78}$: this is due to missed measurements and hard scattering processes and is predicted by the MC calculations.

Above a few GeV, the narrowing of the PSF with energy is limited by the finite hit resolution of the Silicon Strip Detectors.

As shown in Fig. 4.4, the PSF is $\sim 5°$ at 100 MeV and decreases to $\sim 0.8°$ at 1 GeV. At 20 GeV, it becomes close to the asymptotic value of $\sim 0.1°$.

The *energy dispersion D* of the instrument is defined as the dispersion of measured energies around the true values and is generally asymmetric, with the most prominent tail being toward lower energies. The *energy resolution* is a figure of merit which is customarily used to summarize in a single number the information contained in the energy dispersion parametrization. It is defined as the half-width of the energy window containing 68% of the energy dispersion on both sides of its most probable value (ΔE), divided by the most probable value itself (E): $\sim \Delta E/E$.

The energy resolution as a function of energy has a minimum between ~ 1 GeV and ~ 10 GeV (Fig. 4.6a), degrading at lower energies due to the energy deposited in the TKR and at higher energies due to the leakage of the electromagnetic shower out the sides and the back of the CAL. Conversely, the energy resolution tends to improve as the incidence angle increases (Fig. 4.6b). This is especially true at high-energy, where a longer path length in the CAL implies less shower leakage.

4.1.3 γ-ray analysis of *Fermi*-LAT data

Because of the paucity of counts and the large PSF of LAT at low energies, when analyzing a point source the contribution of nearby sources must be included. A Region Of Interest (ROI) is then chosen to be several time the characteristic PSF size and each source in the ROI requires a model. The sources outside the ROI can bring photons as well, therefore the model is extended in the so-called Source Region, centered on the ROI and with a radius that is larger than the ROI radius of several PSF scale length.

A likelihood analysis is performed on LAT data in order to assess the presence of a γ-ray source in a ROI of the sky.
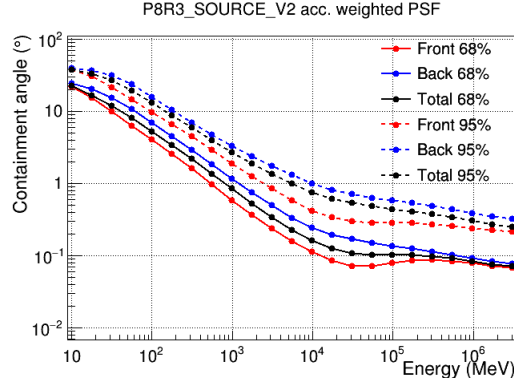
Figure 4.4: 68% and 95% containment angles of the PSF for the P8R3_V2 response function, derived from Monte Carlo simulations. The *Front* and *Back* classes of events refer to the location of the tracker where the conversion takes place.

Given a data set D and a parametrized model $M(x)$, the likelihood function of the model is defined as the probability of obtaining the data D if the model is true:

$$\mathcal{L}(M) = P(D|M(x)) \ . \tag{4.1}$$

As a consequence, the value of x that maximizes the likelihood is considered to be the best estimator for the true value.

When a comparison between two different models is needed, a *likelihood ratio test* is performed in order to assess which model is more statistically significant. To this purpose, the *test statistics* is defined as

$$TS = -2 \log \left(\frac{\mathcal{L}_{max,0}}{\mathcal{L}_{max,1}} \right) \tag{4.2}$$

where $\mathcal{L}_{max,0}$ and $\mathcal{L}_{max,1}$ are the maximum likelihood values for each model. In γ-ray analysis, the input model M is the distribution of γ-ray sources in the sky and includes their intensity and spectra. $\mathcal{L}_{max,0}$ is the maximum likelihood for the model without any additional source (*null hypothesis*): in this scenario, all the events in the data set are due to an isotropic background. $\mathcal{L}_{max,1}$ is the maximum likelihood for the model which includes the presence of a source in a given location.

For a large number of counts, Wilks' theorem (Wilks 1938) states that the test statistic of the null hypothesis follows a χ_n^2 distribution, where n is the number of parameters in the model for the additional source. As a rule of thumb,

$$\sigma \sim \sqrt{TS} \ , \tag{4.3}$$

where σ is the detection significance for a given source.

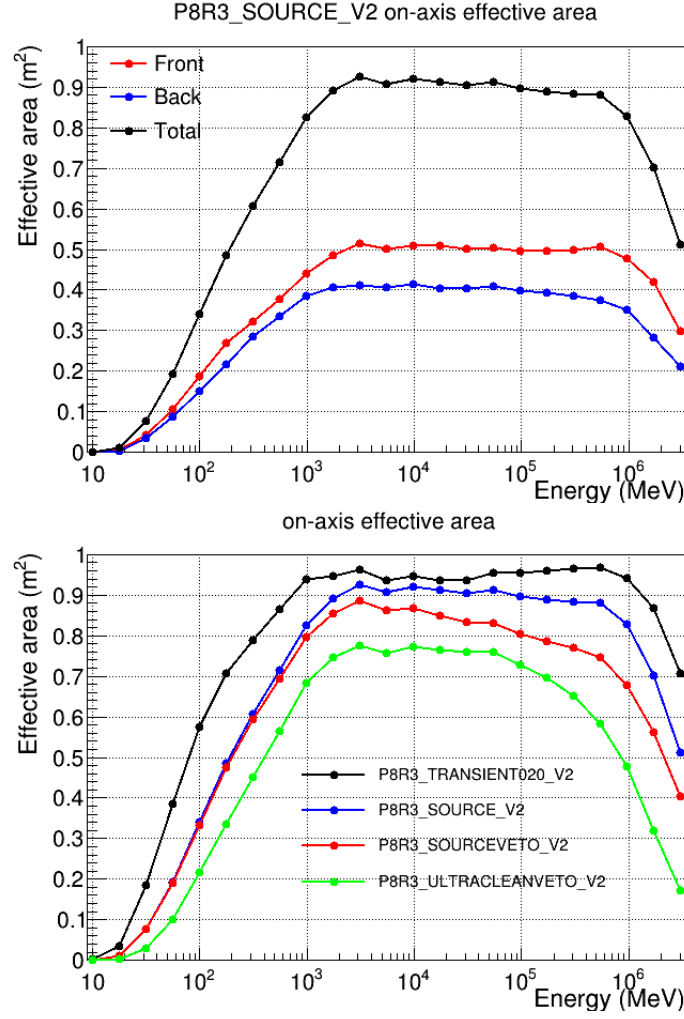The functional form of the likelihood can be obtained starting from the evidence

Figure 4.5: *Upper Panel*- Effective area as a function of energy for normal incidence photons. The *Front* and *Back* classes of events refer to the location of the tracker where the conversion takes place. *Lower Panel*- On-axis effective area (as a function of the energy) for different event classes.

that LAT data will be divided in many bins because they depend on many variables. As a consequence, even with a great number of counts, each bin will contain a small number of them, following a Poisson distribution. The likelihood function $\mathcal{L}$ is defined as the probability n_k of observing the detected counts in each bin while m_k counts are predicted by the model:

$$\mathcal{L} = \prod_k \frac{m_k^{n_k} e^{-m_k}}{n_k!} = e^{-N_{pred}} \prod_k \frac{m_k^{n_k}}{n_k!} \tag{4.4}$$
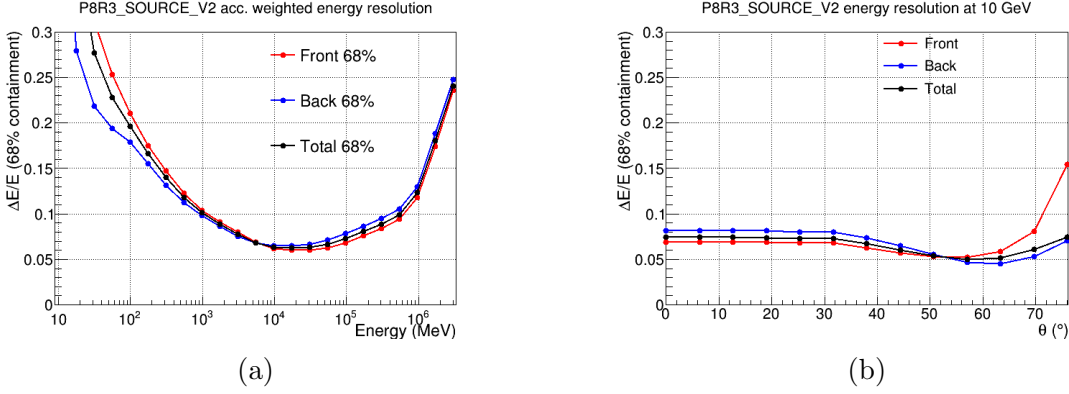
Figure 4.6: *Left*: Energy resolution of LAT as a function of energy. *Right*: Energy resolution of LAT for 10 GeV photons as a function of the incidence angle. In both figures, the *Front* and *Back* classes of events refer to the location of the tracker where the conversion takes place.

If the size of the bins gets infinitesimally small, $n_k = 0$ or 1. The resulting functional form for the likelihood is

$$\mathcal{L} = e^{-N_{pred}} \prod_k m_k \; . \tag{4.5}$$

This is called *unbinned likelihood* and is an accurate choice for a small number of counts. For a large number of counts, the *binned* likelihood in Eq. 4.4 is preferred for reducing the calculus time.

The likelihood analysis of LAT data requires models of Galactic diffuse and isotropic emission. The Galatic model is a spatial and spectral template and it was built tracing H_2 with spectral line surveys of CO (as a tracer of H_2) and H I (HI4PI Collaboration et al. 2016) to derive the distribution of interstellar gas in the Galactocentric rings. The γ-ray emissivity of the rings was then fitted in several LAT energy bands in order to obtain the diffuse γ-ray model provided by *Fermi*. The version for Pass 8 data is the `gll_iem_v07.fits` file and it was used in this analysis.

The background contribution from extragalatic diffuse sources of γ-rays must be taken into account as well. This emission is isotropic and it is modelled with a spectral template obtained with a fit to all-sky γ-ray emission excluding the Galactic plane. The templates are extracted in the energy range between 30 MeV and 1 TeV and they are provided by *Fermi* as well. In this work, the recommended `iso_P8R3_SOURCE_V3_v1.txt` template was employed.

4.1.4   4FGL: The Fermi-LAT 8-years Point Source Catalogue

The *Fermi* Collaboration released several catalogues of γ-ray sources built with data from the *Fermi*-LAT. The first LAT Source Catalog was released after the first eleven months of LAT activity and was named 1FGL (Abdo et al. 2010a).

Over years, several other source catalogues were built with the increasing quantity of available data. In this work, data from the 8-years Point Source Catalogue were used (4FGL) (Abdollahi et al. 2020). Point sources were included in this catalogue depending on their significance ($TS > 25$) over the entire time range of analysis, therefore it does not contain transient γ-ray sources. The total number of sources in 4FGL is 5098, which is almost three times the number reported in 1FGL (1451 point sources). The catalogue spans the energy range between 0.05 GeV and 1 TeV. The data were collected from 2008 August 4 (15:43 UTC) to 2016 August 2 (05:44 UTC) and they do not include intervals around solar flares (2 days overall) and GRB ($\sim$ 39 ks).

AGN are the largest source population in 4FGL, expecially the class of blazars, with 3131 associations. The blazar sample is made of 686 FSRQ, 1116 BL Lac and 1130 Blazars of Uncertain Type (BCU).

Two spectral representations were used for AGNs in the catalogue: a simple power law form for all sources not significantly curved and a LogParabola model for all curved spectra.

A source is considered significantly curved if $TS_{curv} > 16$, where

$$TS_{curv} = 2Log\left(\frac{\mathcal{L}(\text{curvedspectrum})}{\mathcal{L}(\text{powerlaw})}\right) \ . \tag{4.6}$$

Among blazars, the HBLs were mostly modelled in 4FGL with simple power law spectra, Eq. 4.7,

$$\frac{dN}{dE} = N_0\left(\frac{E}{E_0}\right)^{\Gamma} \ , \tag{4.7}$$

where N_0 is the normalization, E_0 is the scale parameter and Γ is the photon index.

For LBLs and part of IBLs the log-parabolic model in Eq. 4.8 (Massaro et al. 2004) is used instead.

$$\frac{dN}{dE} = N_0\left(\frac{E}{E_b}\right)^{-(\alpha+\beta log(E/E_b))} \ , \tag{4.8}$$

where N_0 is the normalization, the parameter α is the photon index at energy E_b, β measures the curvature of the parabola and E_b is a usually fixed scale parameter that should be set close to the lowest energy range of the spectrum being fit. This model is a simple representation of curved spectra when they do not show

an exponential cutoff and it has a energy-dependent photon index given by the log-derivative of Eq. 4.8,

$$\Gamma(E) = \alpha + 2\beta log(E/E_b) \ .\tag{4.9}$$

The parameters of the equivalent power-law model are reported in 4FGL for every LogParabola source.

The photon flux in 4FGL is reported in 7 energy bands, covering the whole $10 \ \mathrm{MeV} - 1 \ \mathrm{TeV}$ range.

Each source in 4FGL is designated by `4FGL JHHMM.m + DDMM`. A counterpart is assigned to most of the sources. The counterparts include several known γ-ray sources: AGN, galaxies, pulsars, pulsar-wind nebulae, supernova remnants, globular clusters, X-ray binaries.

Chapter 5

Experimental sample and analysis of *Fermi* data

5.1 The sample

The search for temporal coincidence between IceCube events and γ-ray emission from *Fermi* blazars was performed on a subsample of 61 galaxies selected by Giommi et al. (2020). The authors investigated the connection between Ice-Cube events and blazar counterparts both via a cross-matching of neutrino events with catalogues of high-energy sources and known blazars and a dissection of each neutrino error region. This last task was performed using the VOU-Blazar tool (Chang et al. 2020), which uses multi-wavelength data in order to identify candidate blazars in a given region of the sky and build their SED.

The method, already used for the dissection of the region around IceCube-170922A in Padovani et al. (2018b), is here applied to a sample of IceCube events which combines high-energy starting tracks, through-going tracks and alerts in the IceCube's realtime program (see Sec. 1.5.1). Each neutrino 90% error region is approximated to be an ellipse. Events with poor angular resolution (where the area of the ellipse was larger than that of a circle with radius $r = 3°$) and too close to the Galactic plane ($|b| < 10°$) were removed. Possible systematic uncertainties in directional reconstruction of the events were accounted for by scaling the axes of the 90% error ellipse, Ω_{90}, to 1.1, 1.3 and 1.5 times their original sizes ($\Omega_{90\times1.1}$, $\Omega_{90\times1.3}$, $\Omega_{90\times1.5}$).

The selected events are cross-matched with the *Fermi*-LAT 3FHL (Ajello et al. 2017) and 4LAC γ-ray catalogues and the multi-wavelength based 3HSP (Chang et al. 2019) catalogue. Then, the regions around each event were dissected using VOU-Blazar. The tool preliminarly uses X-ray and radio emission in order to identify possible blazar candidates, then it retrieves multi-wavelength data from

multiple catalogues and spectral databases. The location of the ν_{peak}^S is estimated and the blazar is subsequently classified as LBL, IBL or HBL.

The observed results are compared in terms of random expectations with a direct comparison and a likelihood ratio test.

After the dissection of their surrounding regions, 72 sources (47 HBL/IBL, 24 LBL and M87) were found within the $\Omega_{90\times1.5}$ and selected as possible neutrino counterparts. Although M87 is usually classified as a radio galaxy, its small jet inclination angle ($\sim 17°$, Walker et al. (2018)) and the superluminal motion detected in multiple frequency bands make it *almost* a blazar. Also, M87 is a strong γ-ray, GeV and VHE emitter, which makes it similar to HBLs. Given the nature of the source, however, it was impossible to estimate a value of ν_{peak}^S.
Most of the sources in the sample were matched with *Fermi* 4FGL sources (for details on Fermi and the 4FGL catalogue, see sec. 4.1). The HBLs in the sample were mostly modelled in 4FGL with simple power law spectra (Eq. 4.7), while for LBLs and part of IBLs a LogParabolic model was preferred in the catalogue (Eq. 4.8).

As the purpose of this work is to study the temporal coincidence between IceCube events and γ-ray emission from blazars, only the sources of the Giommi et al. (2020) sample detected by *Fermi* were taken into account. For these, it is indeed possible to build light curves covering the entire period 2008-2020.

The sample of IceCube events selected in this work is listed in Tab. 5.1. Note that is possible for each event to be associated with more than one candidate counterpart.

Out of the 72 sources selected in Giommi et al. (2020), 61 were successfully matched with 4FGL or 3FGL sources and subsequently modeled. TXS 0506+056 and its associated event IceCube-170922A were part of the sample in Giommi et al. (2020): the object was matched with the 4FGL source 4FGL J0509.4+0542, which was considered a reference for the other sources in this work (see Chap. 6).

The full list of 4FGL (59) and 3FGL (2) sources that were analyzed in this thesis is shown in Tab. 5.2 and Tab. 5.3, respectively. For each source, redshift z and classification are reported. The reported photon index (Γ) refers to a power law model (even when a LogParabola model was statistically preferred). The F column is the average flux of the sources from the 4FGL 2-months binned light curves provided by the *Fermi* collaboration (Abdollahi et al. 2020). This quantity is not available for the 3FGL sources.

The last column (V) shows the *variability index* of each source from 4FGL. This parameter was calculated on the one-year binned light curves of the sources and it is defined as

$$TS_{var} = 2\sum_i [log\mathcal{L}_i(F_i) - log\mathcal{L}(F_{glob})] - \max(\chi^2(F_{glob}) - \chi^2(F_{avg}), 0) , \quad (5.1)$$
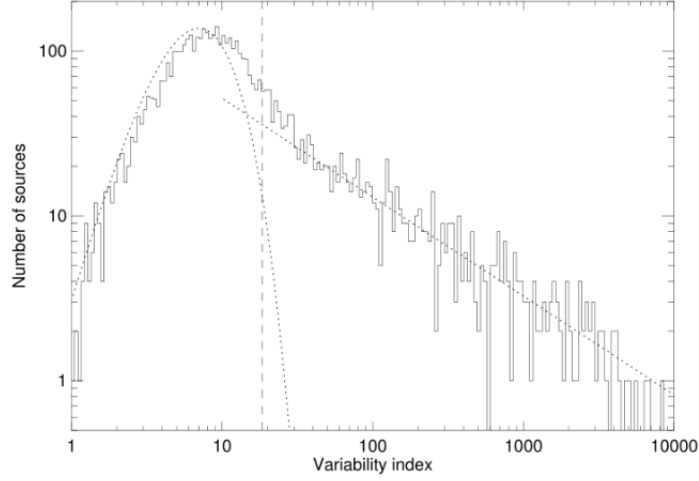
Figure 5.1: Distribution of observed TS_{var} in 4FGL. The $\chi^2(7)$ distribution on the left is expected for non-variable sources, while the dotted line at right is a power-law decreasing as $TS_{var}^{-0.6}$. The dashed vertical line is the threshold above which a source is considered likely variable. Credits: Abdollahi et al. (2020).

where

$$\chi^2(F) = \sum_i \frac{F_i - F}{\sigma^2} \ , \tag{5.2}$$

while F_{avg} is the average flux from the light curve and it can differ slightly from the global flux, F_{glob}, because of systematic effects. F_{glob} is derived from a full-band analysis on the entire period of observation assuming the best spectral shape (Abdollahi et al. 2020).

The distribution of observed TS_{var} in 4FGL is shown in Fig. 5.1. It appears like a composition of a power-law and a χ^2 distribution with 7 degrees of freedom, where 7 is the result of $N_{int} - 1$, with $N_{int} = 8$, the number of intervals in the one-year binned light curves. The left part of the distribution corresponds to constant sources and sources too faint to have measurable variability. Many blazars fall in this range, as illustrated in Tab. 5.2. Variability is considered probable if $TS_{var} > 18.45$, corresponding to a 99% confidence level in the $\chi^2(7)$ distribution. Based on this criterion, 26 out of 61 sources in this sample can be considered likely to be variable.

The same definition of TS_{var} has been used in 3FGL, although in this case the 1-month binned light curves built on 4 years of *Fermi* data were considered, for a total number of $N_{dof} = 48$ degrees of freedom. As a consequence, the threshold required for variability is higher, $TS_{var} > 72.44$.

According to the classification reported in Tab. 5.2, 25 sources are HBLs, 15

are IBLs and 19 are LBLs.

The redshift distribution of the sources is shown in Fig. 5.2. The LBLs display $z_{avg} = 1.20 \pm 0.51$, while for IBLs $z_{avg} = 0.46 \pm 0.26$ and for HBLs $z_{avg} = 0.35 \pm 0.15$: on average, the LBLs are seen at higher redshifts. This could be due to the fact that these sources tend to be brighter than HBLs and IBLs. This effect is a consequence of the shape of SED of the sources (Fig. 2.5): the high-energy peak of HBLs is usually located in the TeV energy range.

A first inspection of the sample was performed in Fig. 5.3, where the mean flux from 4FGL light curves is shown as a function of the Γ index of each source (Tab. 5.2). No correlation is observed except the one suggested by the different classes of the sources: LBLs tend to have higher fluxes and higher values of Γ, since their high-energy peak is located at lower energies, possibly in the *Fermi* energy range. HBLs, conversely, tend to have lower flux values and low Γ values since their high-energy peak should occur at higher energies, $E > 300$ GeV (see Fig. 2.5).

The average properties of the sample are summed up in Tab. 5.4.

5.2 Data analysis: the γ-ray light curves

Table 5.1: Sample of IceCube events from Giommi et al. (2020) with MJD[1] arrival time. The energy of the event is taken from Padovani et al. (2018a), The IceCube Collaboration et al. (2015), and IceCube Collaboration et al. (2017). The error on the energy is reported when available.

Event	Time (MJD)	Energy (TeV)
IceCube-160331A	57478.60	380
IceCube-121011A	56211.77	210
IceCube-190730A	58694.87	299
IceCube-150831A	57265.22	
IceCube-090813A	55056.70	480
IceCube-161103A	57695.38	
IceCube-190504A	58607.77	
IceCube-141109A	56970.21	$53.8^{+7.2}_{-6.3}$
IceCube-151114A	57340.90	740

IceCube-140721A	56859.76	$52.6^{5.2}_{-5.7}$
IceCube-130408A	56390.19	$30.8^{+3.3}_{-3.2}$
IceCube-190819A	58714.50	
IceCube-160814A	57614.91	
IceCube-140216A	56704.60	$71.5^{+8.3}_{-7.2}$
IceCube-170506A	57879.53	
IceCube-110930A	55834.45	
IceCube-150714A	57217.90	300
IceCube-140114A	56671.88	$84.6^{+7.4}_{-7.9}$
IceCube-141126A	56987.77	75.8
IceCube-151017A	57312.70	230
IceCube-120515A	56062.96	200
IceCube-131202A	56628.57	$46.5^{+5.9}_{-4.5}$
IceCube-141209A	57000.14	97.4
IceCube-150428A	57140.47	73.5
IceCube-160510A	57518.66	
IceCube-111216A	55911.28	660
IceCube-110521A	55702.77	300
IceCube-150926A	57291.90	
IceCube-120123A	55949.57	$82.2^{+9.6}_{-8.4}$
IceCube-150911A	57276.57	126.3
IceCube-110610A	55722.43	210
IceCube-100710A	55387.54	230
IceCube-131204A	56630.47	
IceCube-190104A	58487.36	
IceCube-170321A	57833.31	120

Table 5.2: Sample of IceCube events from Giommi et al. (2020) successfully matched with 4FGL blazars. The class and z are taken from Giommi et al. (2020), while the Γ column refers to the 4FGL power-law index, F is the mean flux between 100 MeV and 300 GeV and V is the variation index as described in Sec. 5.1.

Event	Source	Class	z	Γ	$F(\text{ ph/cm}^2/\text{s}^{-1})$	V
IceCube-160331A	4FGL J0103.5+1526	HBL	0.25	2.41	0.45×10^{-8}	3.92
IceCube-121011A	4FGL J1339.9-0138	LBL	1.62	2.35	1.5×10^{-9}	31.49
IceCube-190730A	4FGL J1504.4+1029	LBL	1.8	2.25	0.3×10^{-6}	13164.00
IceCube-150831A	4FGL J0336.4+3224	LBL	1.26	2.83	0.33×10^{-7}	21.00
	4FGL J0344.4+3432	HBL	nd	1.83	1.2×10^{-9}	8.14
IceCube-090813A	4FGL J0158.8+0101	IBL	0.95	2.59	0.8×10^{-8}	1.86
IceCube-161103A	4FGL J0239.5+1326	HBL	0.5	2.12	0.3×10^{-8}	43.37
	4FGL J0244.7+1316	IBL	0.9	2.6	0.8×10^{-8}	33.97
IceCube-190504A	4FGL J0428.6-3756	LBL	1.11	2.01	2.3×10^{-7}	2603.05
	4FGL J0420.3-3745	LBL	0.3	2.28	2×10^{-8}	82.15
IceCube-141109A	4FGL J0339.2-1736	HBL	0.07	1.93	0.58×10^{-8}	14.5
IceCube-151114A	4FGL J0502.5+1340	LBL	nd	2.26	0.65×10^{-8}	17.88
IceCube-140721A	4FGL J0648.0-3045	LBL	1.15	2.48	0.28×10^{-7}	416.15
	4FGL J0649.5-3139	HBL	0.56	1.7	2.2×10^{-9}	56.35
IceCube-130408A	4FGL J1117.0+2013	HBL	0.14	1.95	1.3×10^{-8}	76.52
	4FGL J1059.5+2057	LBL	0.39	2.38	0.5×10^{-8}	21.33
	4FGL J1124.0+2045	HBL	0.54	1.91	1.4×10^{-9}	7.62
	4FGL J1124.9+2143	HBL	0.36	2.03	2×10^{-9}	5.16
IceCube-190819A	4FGL J0946.2+0104	HBL	0.58	1.9	1.8×10^{-9}	5.32
	4FGL J1003.4+0205	HBL	0.48	1.95	1.5×10^{-9}	5.19

---

[1]Modified Julian Date, where the Julian Date (JD) is the number of days since Greenwich mean noon on January 1, 4713 B.C.E. Since JD is a quite a large number (e.g January 1, 2008 corresponds to JD = 2454466.5) and our calendar days start and end at midnight, we define MJD=JD-2400000.5.

	4FGL J0948.9+0022	LBL	0.59	2.63	1.25×10^{-7}	1186.43
IceCube-160814A	4FGL J1316.1-3338	LBL	1.21	2.3	0.5×10^{-7}	458.52
IceCube-140216A	4FGL J1404.8+6554	HBL	0.36	2.03	2×10^{-9}	30.51
IceCube-170506A	4FGL J1447.0-2657	HBL	0.32	1.87	1.2×10^{-9}	7.36
	4FGL J1440.0-2343	HBL	0.25	1.98	0.35×10^{-8}	19.94
	4FGL J1439.5-2525	IBL	0.18	1.73	0.9×10^{-9}	2.45
IceCube-110930A	4FGL J1744.2-0353	LBL	1.06	2.51	1.2×10^{-8}	13.69
IceCube-150714A	4FGL J2133.1+2529	HBL	0.29	2.04	0.25×10^{-8}	7.95
	4FGL J2133.0+2610	LBL	0.8	2.45	0.7×10^{-8}	42.16
IceCube-140114A	4FGL J2227.9+0036	IBL	nd	2.06	0.8×10^{-8}	10.24
	4FGL J2226.8+0051	LBL	2.26	2.42	0.4×10^{-8}	8.89
	4FGL J2223.3+0102	HBL	0.51	1.94	1.5×10^{-9}	15.2
IceCube-141126A	4FGL J1231.5+1421	HBL	0.26	1.87	2.5×10^{-9}	9.58
IceCube-151017A	4FGL J1314.7+2348	IBL	nd	2.02	0.8×10^{-8}	25.71
	4FGL J1300.0+1753	IBL	0.55	2.56	0.65×10^{-8}	7.95
	4FGL J1321.1+2216	LBL	0.94	2.34	0.35×10^{-7}	350.55
IceCube-120515A	4FGL J1310.5+3221	LBL	0.99	2.26	0.38×10^{-7}	170.41
	4FGL J1311.0+3233	LBL	1.64	2.44	0.27×10^{-7}	52.2
	4FGL J1321.9+3219	IBL	nd	2.17	1.8×10^{-9}	10.48
IceCube-131202A	4FGL J1341.8-2053	LBL	1.58	2.71	0.2×10^{-7}	80.86
IceCube-141209A	4FGL J1043.6+0654	IBL	0.43	2.03	0.25×10^{-8}	4.87
	4FGL J1040.5+0617	IBL	nd	2.26	2.9×10^{-8}	122.44
IceCube-150428A	4FGL J0525.6-2008	IBL	0.12	2.14	0.3×10^{-8}	12.42
IceCube-160510A	4FGL J2326.2+0113	IBL	0.53	1.68	0.2×10^{-9}	5.9
IceCube-111216A	4FGL J0232.8+2018	HBL	0.14	1.77	1.7×10^{-9}	4.36
	4FGL J0224.2+1616	IBL	0.3	2.3	0.6×10^{-8}	9.24
IceCube-110521A	4FGL J1554.2+2008	HBL	0.27	1.79	1.2×10^{-9}	7.64

	4FGL J1533.2+1855	HBL	0.3	1.83	2×10^{-9}	1.49
	4FGL J1528.4+2004	HBL	0.52	2.02	1.2×10^{-9}	7.88
IceCube-150926A	4FGL J1258.7-0452	HBL	0.59	1.78	10^{-9}	7.18
IceCube-120123A	4FGL J1359.1-1152	IBL	0.27	1.53	1.1×10^{-8}	10.27
IceCube-150911A	4FGL J1557.9-0001	LBL	1.77	2.49	0.6×10^{-8}	13.68
IceCube-110610A	4FGL J1808.2+3500	IBL	0.4	2.22	0.4×10^{-8}	4.26
	4FGL J1808.8+3522	HBL	0.22	2.21	0.35×10^{-8}	2.74
IceCube100710A	4FGL J2030.5+2235	HBL	nd	1.78	0.9×10^{-9}	9.27
	4FGL J2030.9+1935	HBL	0.27	1.84	2×10^{-9}	17.29
IceCube-131204A	4FGL J1916.7-1516	LBL	nd	2.6	0.15×10^{-7}	82.84
IceCube-190104A	4FGL J2358.1-2853	IBL	nd	2.23	0.55×10^{-8}	3.14
	4FGL J2350.6-3005	HBL	0.23	2.01	0.45×10^{-8}	23.3

Table 5.3: Sample of IceCube events from Giommi et al. (2020) successfully matched with 3FGL blazars. The 8-years, 2-months binned 4FGL light curves for these sources are not available, as a consequence the F value has note been included.

Event	Source	z	Class	Γ	$F(\text{ ph/cm}^2/\text{s}^{-1})$	V
IceCube-170321A	3FGL J0627.9-1517	0.29	HBL	2.72	-	52.66
IceCube-151017A	3FGL J1258.4+2123	0.63	HBL	2.64	-	43.31

In order to study the temporal coincidence between the IceCube events in Tab. 5.1 and the γ-ray activity of the sources in Tab. 5.2, light curves centered on the arrival time of each associated event were built for every source in the sample. *Fermi*-LAT data between 0.1 and 300 GeV were used. This energy range is recommended by *Fermi*: below 100 MeV it is required to account for energy dispersion because of a non-negligible bias in LAT energy reconstruction, while above 300 GeV the validation process of data is hampered by lack of statistics.

As a first step, the 2-months binned light curves presented in the 4FGL paper were inspected. These light curves, provided by the Fermi collaboration, were

Table 5.4: Average properties of the sample described in Tab. 5.2. LBLs are found at higher redshift and flux values compared to HBLs and IBLs and they have flatter spectrum (higher Γ_{avg}). In addition, LBLs are the only variable class of sources ($V_{avg} > 18.48$).

	HBL	IBL	LBL
z_{avg}	0.35 ± 0.15	0.46 ± 0.26	1.20 ± 0.51
Γ_{avg}	1.94 ± 0.15	2.14 ± 0.31	2.43 ± 0.18
F_{avg} (ph/cm²/s)	2.67×10^{-9}	6.82×10^{-9}	5.1×10^{-8}
V_{avg}	15.9	17.68	990.38

built applying a likelihood analysis in each single (2 months long) bin after having fixed all the spectral parameters but the normalization of all the sources in the ROI centered to the studied target to the best values obtained with a fit on the 10 years of data. In these plots, points with $TS < 25$ were treated as upper limits.

This first look at the sample made it evident that most of LBLs had been detected by *Fermi* with $TS > 25$ for the whole time range covered in 4FGL, while the majority of HBLs displayed two-months binned light curves mainly composed of upper limits. An example of the two different situations is shown in Fig. 5.4. This is expected: LBLs, having higher fluxes, are statistically favoured.

The second step was the production of light curves of each blazar in our sample using different temporal windows centered on the neutrino time event and temporal bins. The 6-months light curves were 7 days binned, while the binning was 3 days for the 3-months light curves, 2 days for the 1-month light curves and 1 day for 2-weeks light curves.

Table 5.5: Time windows and binning adopted for the light curves of the sources in Tab. 5.2 and Tab. 5.3.

Time window	Binning
6-months	7-days
3-months	3-days
1-month	2-days

The Region of Interest (ROI) was defined as the 10° circle around the coordi-

nates of the source. Our light curves were built following the standard analysis procedure[2]: a full binned likelihood γ-ray analysis of the ROI was performed with the *fermipy* Python package based on the Fermi Science Tools (Wood et al. 2017).

The following routine was followed:

- Data acquisition: *Fermi* data of the 20° region centered on each source were downloaded from the LAT Data Query[3] in the $0.1 - 300$ GeV energy range.

- Event selection: in order to select data with a high probability of being photons, it was set `evclass=128` during data selection, as recommended for point source analysis. Moreover, a proper cut on the zenith angle was adopted in order to mitigate the contribute of the background from photons from the Earth limb. The recommended value by Fermi for the reconstruction of events above 100 MeV is 90°, therefore data with a maximum zenith angle of 90° were selected during data preparation.

- ROI builing: the ROI was defined as the 15° radius circle centered on each source. The spectral models of sources in the ROI are extrated from the 4FGL catalog;

- Full Binned Likelihood Analysis as described below.

For each time bin, a first binned likelihood analysis of the sources in the inner 3° of the ROI was performed in the whole energy range. For each source in this region, the normalization was the only free parameter, while the indices of the PowerLaw (Γ) or LogParabola (α, β) were kept fixed. The P8R3_SOURCE_V3 Instrument Response Function was used. Then, a test statistic (TS) map of the ROI was created. The *fermipy* analysis method for this purpose is called TS Map and it evaluates the maximum likelihood test statistics given by

$$TS = 2 \sum_k \ln(\mathcal{L}(\mu, \theta | n_k)) - \ln(\mathcal{L}(0, \theta | n_k)) \quad , \qquad (5.3)$$

where the sum runs over both spatial and energy bins, μ is the normalization parameter of the source and θ stands for the parameters of the background model. It returns a map representation of the TS and predicted counts of the best-fit test source at each position.

As a third step, the Source Finding method in *fermipy* is applied. This algorithm uses peak detections on a TS Map to find new source candidates, identifying peaks with $\sqrt{TS}$ above a fixed threshold and with an angular distance larger than

---

[2]https://fermi.gsfc.nasa.gov/ssc/data/analysis/scitools/binned_likelihood_tutorial.html
[3]https://fermi.gsfc.nasa.gov/cgi-bin/ssc/LAT/LATDataQuery.cgi

a certain minimum separation from a higher amplitude peak in the map. The additional peaks are then ordered according to the TS value and a source is added to each one. The position of these additional sources is set by fitting a 2D-parabola to the log-likelihood surface around the peak maximum. These tasks are performed by the function `find_sources`. The Source Finding algorithm is a useful tool for the identification of candidate fast-flaring sources in the ROI, therefore it was applied to every bin of the light curves. The $\sqrt{TS}$ threshold was set to 5, while the minimum separation between peaks was $0.5°$. After that, a second likelihood analysis of the ROI was performed.

The upper limits are evaluated in *fermipy* with the CL$_S$ technique (Read 2002), a statistical method mostly used in high-energy physics. If θ is a non-negative parameter in a probability distribution with a random sample X, a CL$_S$ upper limit on θ with confidence level $(1 - \alpha)$ is an observable random variable $\theta_{up}(X)$ which satisfies the property

$$\frac{P(\theta_{up}(X) < \theta|\theta)}{P(\theta_{up}(X) < \theta|0)} \leq \alpha \tag{5.4}$$

for all θ. For the flux values in the light curves of the sample in Tab. 5.2, 95% CL$_S$ upper limits ($\alpha = 0.05$) were considered.

The time bins are given as Modified Julian Dates (MJD).
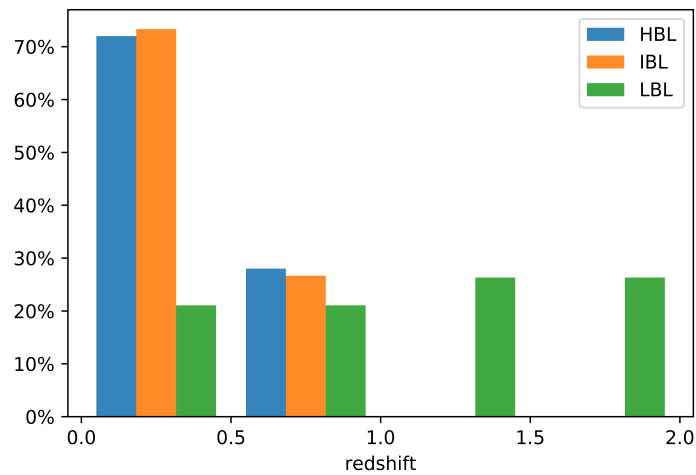
Figure 5.2: Redshift distribution of the blazars in the sample. LBLs, IBLs and HBLs are displayed in different colors. The $0 - 0.5$ redshift range includes sources with unmeasured redshift (mostly HBLs, see Tab. 5.2). 18 HBLs ($> 70\%$) have a measured $z < 0.5$ or unmeasured redshift, while the remaining have $0.5 < z < 1$. Only 3 LBLs ($\sim 15\%$) have $z < 0.5$, the majority of these sample sources is found at $z > 0.5$. IBLs show a similar behaviour to HBLs, with $> 70\%$ of them having $z < 0.5$ or unmeasured redshift.
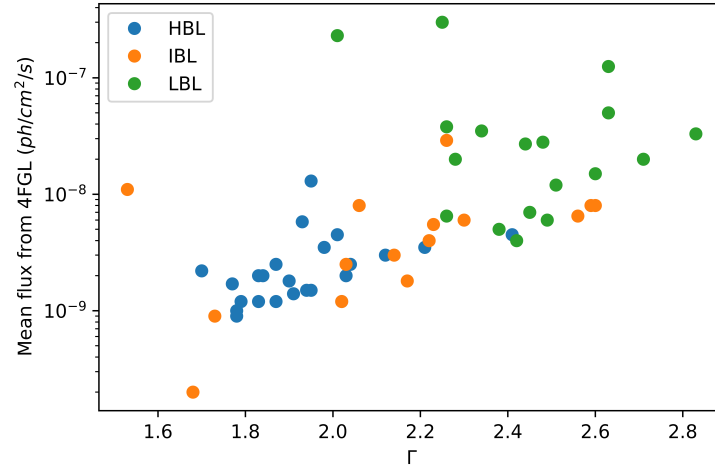
Figure 5.3: Mean flux from 4FGL light curves $(0.1 - 300 \text{ GeV})$ as a function of the Γ index. HBLs tend to have lower flux values and Γ values since their high-energy peak may be located outside $Fermi$ energy range, > 300 GeV. Conversely, LBLs have higher flux values and flatter spectral indices. IBLs show an intermediate behaviour.
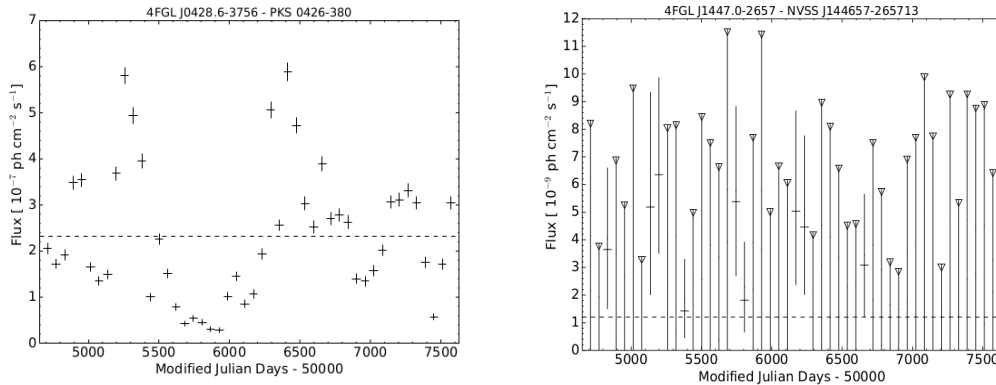
Figure 5.4: Examples of 8-years light curves from 4FGL for two different sources, a LBL (left) and a HBL (right). The binning is 2-months and points with $TS < 25$ are treated as upper limits.

Chapter 6

Flare-neutrino coincidences: selection and statistics

For every source in the sample (Tab. 5.2), 6-months, 3-months and 1-month light curves with a bin size of 7-days, 3-days and 2-days, respectively, were built according to the procedure described in Sec. 5.2.

A N parameter was defined as the percentage ratio between the number of detections, N_{det}, and the total number of bins, N_{bins}:

$$N = \frac{N_{det}}{N_{bins}} \times 100 \text{ \%}. \tag{6.1}$$

The N parameter quantifies the rate of detections in each time scale.

A study of the N parameter distribution for each class of objects was performed for each time window. First, the light curves spanning 8 years and with a bin size of 2 months provided by the *Fermi*-LAT collaboration (see Sec. 5.2) were considered. The detection threshold is $TS = 25$. The result is displayed in Fig. 6.1a. The value of N for the 6-months, 3-months and 1-month light curves is shown in Fig. 6.1. HBLs and IBLs tend to have lower γ-ray fluxes than LBLs in the *Fermi* analysis range and they will therefore be more difficult to detect on short timescales.

The trend observed in the 8-years light curves is confirmed by our light curves with a high temporal resolution (see Fig. 6.1b, 6.1c, 6.1d). IBLs and HBLs (fainter objects in the FERMI band) have low probability of detection (less than 25%) in all the windows with a bin-size of 2/3 days. Note that for bin size ≤ 7 days a less restrictive detection threshold ($TS > 9$) is adopted.

Only a small fraction of IBLs ($\sim 10\%$) is still detected more than 25% of the time (but less than 50%) using a 1 week-bin size. LBLs, as expected, are the class with the largest rate of detections. However, despite their high statistics, LBLs are the blazar class with the smaller probability to be counterparts of the neutrino sources (Giommi et al. 2020).

The weighted average flux of the source in the 6-months interval centered on the event has been calculated for each source in Tab. 5.2 and Tab. 5.3 as

$$F_{avg} = \sum w_i F_i \quad , \tag{6.2}$$

where w are the weights, $w = 1/\sigma^2_{flux}$ for bins with a significant detection and $[F_i^{UL} - F_i/2]^{-2}$ for upper limits (Angioni 2019).

The variability index Var of the 6-months light curves has been calculated following Angioni (2019) in order to investigate the presence of short-time scale variability in the selected sources:

$$Var/dof = \frac{\sum_i w_i (F_i - F_{avg})^2}{dof} \quad , \tag{6.3}$$

where $dof = N_{bins} - 1$ are the degrees of freedom of the light curve and w are the weights as defined in Eq. 6.2. The variability index follows a χ^2 distributions with $N_{bins} - 1$ degrees of freedom. A corresponding p-value was calculated as $p = 1 - CDF(Var, dof)$, where $CDF(Var, dof)$ is the cumulative distribution function for a χ^2 distribution. The sources were considered variable when $p < 10^{-3}$ ($\sim 3\sigma$ significance).

The aim of this work is to assess the presence of flaring γ-ray activity from the sources listed in Tab. 5.2 coincident with the neutrino events in Tab. 5.1. To this purpose, a definition of *flaring* and *coincident* was needed, which was particularly challenging due to the different nature of the three source classes included in the sample: LBLs, IBLs and HBLs (see Sec. 3).

As a consequence, we performed the analysis described in Sec. 5.2 on the IBL TXS 0506+056, matched with the *Fermi* source 4FGL J0509.4+0542, in order to analyze the resulting light curves and extract a general criterion for our sample.

6.1 TXS 0506+056 (4FGL J0509.4+0542)

Light curves centered on the associated neutrino event were built for the IBL TXS 0506+056, in order to compare this source to the sample selected in Tab. 5.2 and 5.3. The 2-months binned light curves are displayed in Fig. 6.2: the neutrino event occurs 6 months after the peak of the γ-ray emission, but the source is still in an enhanced γ-ray state at the arrival time of the neutrino. 6-months, 3-months and 1-month light curves are displayed in Fig. 6.3.

The arrival time of IceCube-170922A is coincident with an average flux state of the source in the 6-months light curve with 7-days binning (Fig. 6.3a). The variation index of this light curve has been calculated, $Var/dof = 10$, corresponding to a p-value $\sim 10^{-40}$: it can therefore be considered variable at the $> 3\sigma$ confidence level. The value of the N parameter is $> 90\%$, an extraordinary high value compared to the sample (see Fig. 6.1).

6.2 A selection of *flaring coincident* sources

We selected a subsample of *flaring coincident* sources on the basis of the behaviour of the 6-months light curves with 7-days binning. As the classes have light curves with different properties, we were forced to adopt a separate approach for the study of HBLs/IBLs and LBLs.

First, we searched for *TXS-like* sources based on the results shown in Sec. 6.1. A $> 3\sigma$ (p-value $< 10^{-3}$) variability and a value $N \geq 50\%$ were required in the 6-months, 7 days binned light curves. Four LBLs were selected as *flaring* sources according to these criteria and they are listed in Tab. 6.1.

We noticed that the comparison with TXS 0506+056 is not suited for sources with intrinsically low statistic, such as HBLs and IBLs: the low detection rate of these sources is due to their spectral shape and we can not correlate the lack of detections and variability to a low activity state of the source. As a consequence, for HBL and IBL blazars it is here implicitly assumed that the source was always too faint to be observed by *Fermi* and that only a significant increase of the flux (i.e. a flare) allowed it to exceed the detection threshold. We searched for sources with at least two flaring states in the one-month interval centered on the neutrino event in the 6-months, 7 days binned light curves. A HBL (4FGL J1117.0+2013) and a IBL (4FGL J1300.0+1753) were selected according to this criterion.

The full subsample of 6 sources (4 LBLs, 1 HBL and 1 IBL) selected for being in a *flaring* state is described in detail in Appendix A. The 6-months light curves with 7-days binning are shown in Fig. 6.4.

We define a *flare-neutrino coincidence* as a neutrino event falling in the 7-days interval centered on a detection. Based on this definition, we can see that a coincidence is observed in 4 light curves out of the 6 promising selected sources: the LBLs 4FGL J0428.6-3756 (Fig. 6.4a) and 4FGL J1916.7-1516 (Fig. 6.4b), the HBL 4FGL J1117.0+2013 (Fig. 6.4e) and the IBL 4FGL J1300.0+1753 (Fig. 6.4f).

Two questions led the prosecution of our work:

- whether the number of coincidence (2 for the class of LBLs and 2 for the HBLs/IBLs class) obtained with the selection criteria exposed above reflects the situation of the whole sample;

- whether the observed *flare-neutrino coincidences* are casual or due to effective neutrino emission from the sources.

The situation was then inspected with a statistical approach.

Table 6.1: Selected sources from Tab. 5.2 based on *TXS-like* characteristics. N_{6m} is the N parameter calculated on the 6-months, 7-days binned light curves centered on each event. Γ is the PowerLaw index of the source from 4FGL, F is the average flux from the 6-months, 7-days binned light curves, Var/dof is the variation index reported with the associated p-value.

Event	Source	z	Class	Γ	F_{avg}	Var/dof	p-value	N_{6m}
IceCube-190504A	4FGL J0428.6-3756	1.11	LBL	2.01	1.95×10^{-7}	10.6	$\sim 10^{-40}$	72%
IceCube-190819A	4FGL J0948.9+002	0.59	LBL	2.63	1.96×10^{-7}	2.6	1.5×10^{-5}	76%
IceCube-131204A	4FGL J1916.7-1516	nd	LBL	2.60	2.12×10^{-7}	3.7	7.4×10^{-10}	69.2%
IceCube-151017A	4FGL J1321.1+2216	0.94	LBL	2.34	4.4×10^{-8}	8.2	$\sim 10^{-30}$	50%

6.3   Statistical analysis

In Giommi et al. (2020), the significance of the spatial coincidence between blazar sources and neutrino events was evaluated with a comparison of the observed statistics and random expectations, as well as a quantitative estimate of the number of blazars that could be associated with IceCube neutrinos.

This task was performed adopting two methods: a direct comparison of the observed blazars counting with the expected random coincidences, where the corresponding probability was calculated using Poisson statistics, and a likelihood ratio test.

The number of expected random coincidences was evaluated by repeating the spatial coincidence analysis in a circular region of 3° radii centered on the Right Ascension of each detected neutrino and with declination increased or decreased by a fixed number of 6°. This procedure led to a control sample covering a total area of 2,573 square degrees (Giommi et al. 2020).

In the likelihood ratio test, according to the background hypothesis (H0), each neutrino uncertainty region has an associated number of expected background sources, while in the signal hypothesis (H1) a certain number N_{src} of sources has a signal counterpart. The smallest p-value was obtained for the HBLs/IBLs in the $\Omega_{90 \times 1.3}$ error region, 1.5×10^{-3}, corresponding in the likelihood approach to a test statistic value of $TS = 12.51$. The background hypothesis can be therefore rejected at 3.56σ (Fig. 6.5).

For the class of LBLs, no significant excess over the background has been observed, which allows to place an upper limit on the maximum number of signal LBLs in the sample, 3.48 sources at 90% CL (Fig. 6.6).

Given the results for the spatial coincidence, in this work the time coincidence between γ-ray activity from the sources and the neutrino event was studied separately for HBLs/IBLs and LBLs in the sample.

6.3.1 HBLs and IBLs

A statistical analysis was performed on HBLs in the sample in order to assess the compatibility of observed coincidences of γ-ray emission and neutrino events and random expectations. The analysis was carried out on the 6-months, 7-days binned light curves, given the low rate of detections ($N \sim 0$, see Fig. 6.1) in the 3-months and 1-month light curves.

For every light curve, a source was considered to be in a *flaring* state when detected with $TS > 9$ as explained in Sec. 6.2. A *coincidence* has been stated to occur when the arrival time of the IceCube event falls in the same time bin of a flare (i.e. in the 7-days interval centered on the detection, see Fig. 6.7).

The number of observed coincidences for the sample of 36 sources considered in the statistical analysis is $N_{obs\_coinc} = 4$. The expected number of coincidence for random associations can be obtained multiplying the flaring probability for the total number of sources: the resulting number for random coincidences is $N_{exp_coinc} = 2.39$.

The significance of this result was evaluated by adopting a randomization of the light curves: the signal detections above 3σ ($TS > 9$) and the arrival time of neutrino events were placed at random times for every light curve in the sample and the corresponding number of coincidences was calculated. The procedure was repeated $N_{trials} = 10^7$ times. The results are shown in Fig. 6.8. The most probable outcome is $N_{coinc} = 2$ ($\sim 30\%$ of cases), while the observed value $N_{obs\_coinc} = 4$ is obtained $\sim 15\%$ of times, corresponding to a p-value $p = 0.19$: while an interesting excess above the expected value is observed, the result is not significant enough to reject the background hypothesis.

As a next step, the expected number of coincidences for the sample was evaluated with a likelihood ratio test as performed in Giommi et al. (2020) for every possible value of the *number signal coincidence* N_{sign_coinc}. In the previous test, all the neutrino arrival times were randomized, $N_{sign\_coinc} = 0$. Here, N_{sign_coinc} ranges from 0 to 36, the total number of sources in the HBL/IBL sample. When $N_{sign\_coinc} = 1$, e.g., a coincidence is assumed to be due to a signal event and the signal from the remaining 35 sources is assumed to be random. The following hypothesis were considered in the likelihood ratio test:

- H0, the background hypothesis: a number of signal coincidences N_{sign_coinc} is present in the sample.

- H1, the signal hypothesis: a number of signal coincidences $N_{obs\_coinc} = 4$ is observed.

The test statistic is defined as $TS = -2 \log \frac{\mathcal{L}(H0)}{\mathcal{L}(H1)}$.

The maximum likelihood was obtained for $N_{sign\_coinc} = 2$ (Fig. 6.9): as a consequence, the most probable hypothesis about the sample is that 2 coincidences

are due to signal events and the remaining 2 observed coincidences are random. The $N_{sign\_coinc} = 4$ case corresponds to a 68% CL upper limit (see Sec. 5.2) on this result.

6.3.2 LBLs

Given the different values of N observed for HBLs/IBLs and LBLs, the statistical tests for these classes should be performed with different definitions of *flaring* state. As a first step, however, we decided to adopt the same definition of *flare* chosen for HBLs/IBLs (a detection with $TS > 9$) for LBLs as well. A more refined statistical study of the LBLs in the sample is left as a future research perspective. As a consequence, the procedure described in Sec. 6.3.1 has been applied to the 18 LBLs in the sample as well. For this class, the number of observed coincidences, $N_{obs\_coinc} = 4$, is equal to the number of expected coincidences from the flaring probability, $N_{exp\_coinc} = 4.6$.

This result is confirmed by the randomization procedure, as shown in Fig 6.10. In the likelihood ratio test (Fig. 6.11) the best fit is obtained for $N_{src} = 0$, when all the coincidences are assumed to be random. This confirms the results of Giommi et al. (2020).
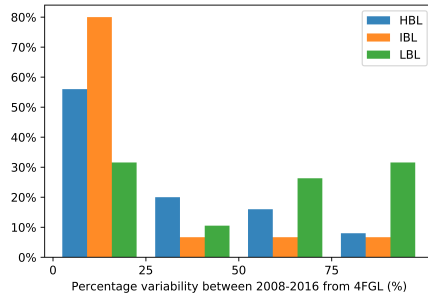
(a) Percentage value of the N parameter of the sample during 2008-2016 from 4FGL 2-months binned lightcurves. Detection with $TS > 25$ are included.
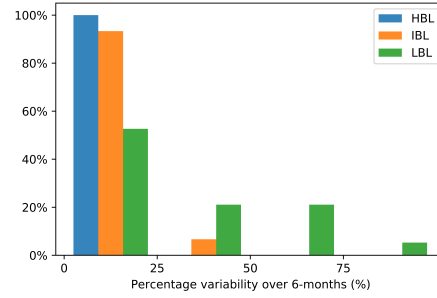
(b) Percentage value of the N parameter of the sample during the 6-months period centered on each IceCube association. The binning is 7 days. Detections with $TS > 9$ are included.
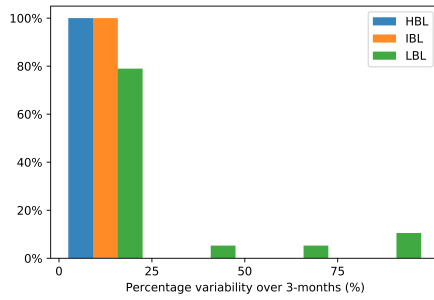
(c) Percentage value of the N parameter of the sample during the 3-months period centered on each IceCube association. The binning is 3 days. Detections with $TS > 9$ are included.
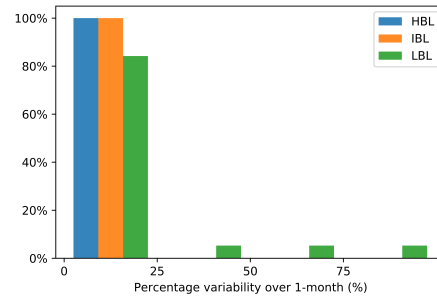
(d) Percentage value of the N parameter of the sample during the 1-month period centered on each IceCube association. The binning is 2 days. Detection with $TS > 9$ are included.

Figure 6.1: Histograms of N distribution in the sample. The full list of N values for each source is reported in Tab. B.1.
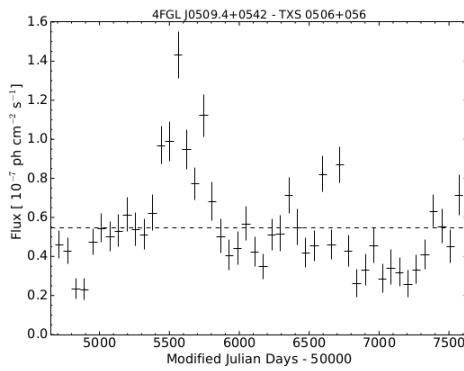
(a) 2-months binned light curve of TXS 0506+056 from 4FGL from August 2008 (54700 MJD) to July 2016 (57600 MJD). The threshold is $TS = 25$. The dashed line is the average 4FGL flux.
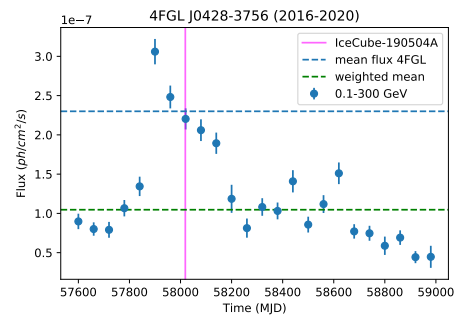
(b) 2-months binned light curve of TXS 0506+056 from July 2016 (57600 MJD) to May 2020 (57900 MJD). The threshold is $TS = 25$. The mean flux from 4FGL and the mean flux between 2016 and 2020 are shown as dashed lines.

Figure 6.2: Light curves of TXS 0506+056 between $0.1 - 300$ GeV, from 2008 to 2020.
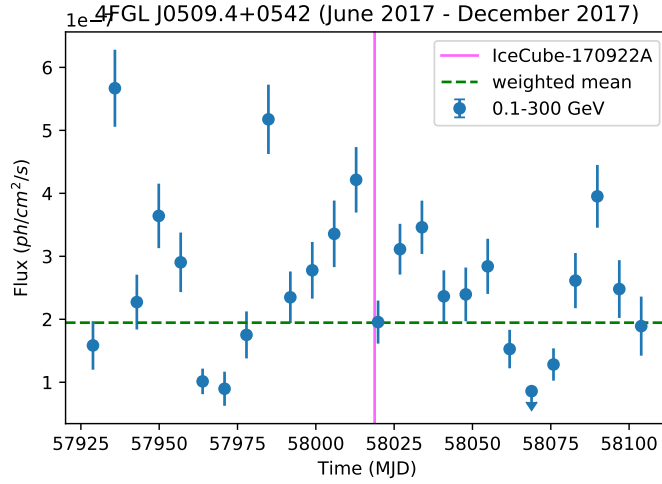
(a) 6-months, 7-days binned light curve of TXS 0506+056 centered on the arrival time of IceCube-170922A. The dotted green line is the average flux of the source. The threshold is $TS = 9$.
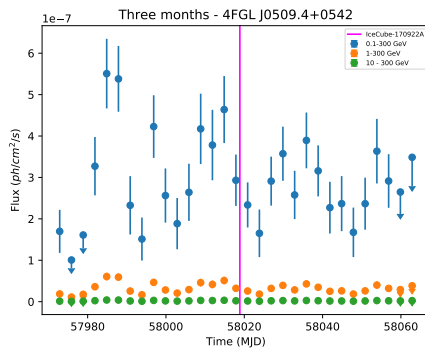
(b) 3-months, 3-days binned light curve of TXS 0506+056 centered on the arrival time of IceCube-170922A. The threshold is $TS = 9$.
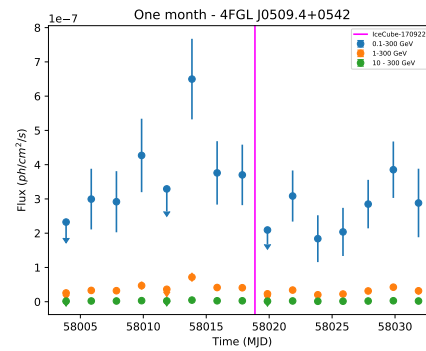
(c) 1-month, 2-day binned light curve of TXS 0506+056 centered on the arrival time of IceCube-170922A. The threshold is $TS = 9$.

Figure 6.3: Light curves of TXS 0506+056 in the $0.1 - 300$ GeV energy range, centered on the arrival time of IceCube-170922A. Different colors indicated different energy range.
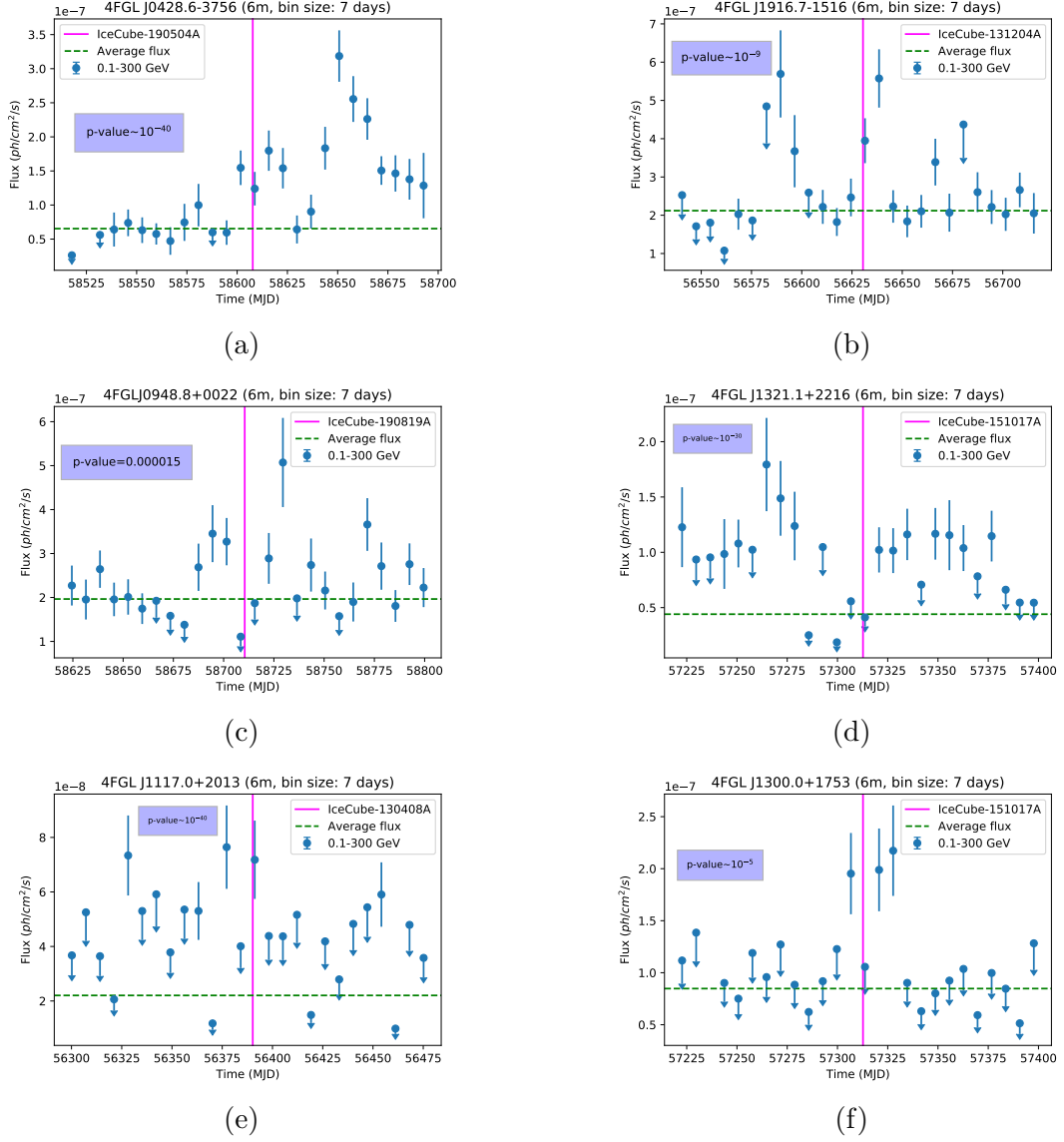
Figure 6.4: 6-months light curves with a bin size of 7 days of the sources listed in Tab. 6.1, the HBL 4FGL J1117.0+2013 (Fig. 6.4e) and the IBL 4FGL J1300.0+1753 (Fig. 6.4f). Each light curve is centered on the arrival time of the associate neutrino event. A source is considered detected if $TS > 9$. The p-value for the variability of each light curve is reported.
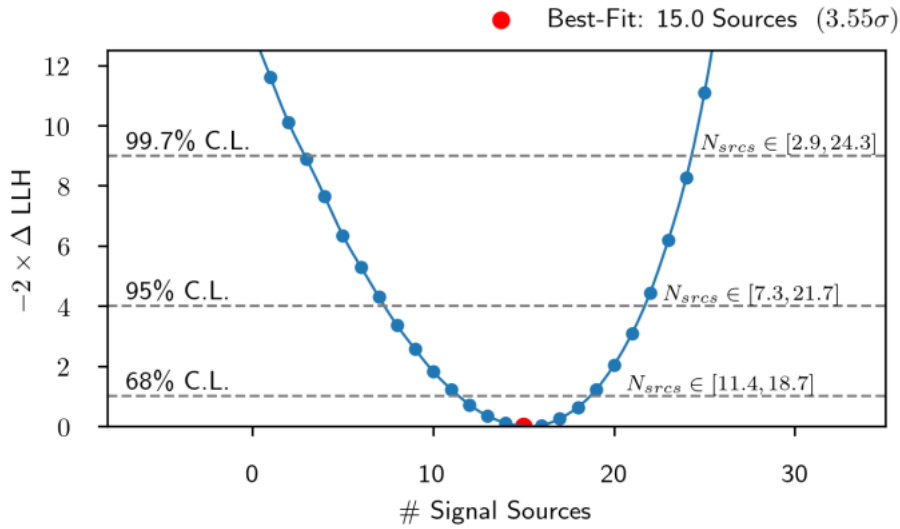
Figure 6.5: The profile likelihood for the class of HBLs/IBLs in $\Omega_{90\times1.3}$ .The best-fit is a number of 15 ± 3.6 signal sources at 1σ confidence level, over a total number of 72 sources in the sample. The background hypothesis is excluded at 3.56σ. From Giommi et al. (2020).
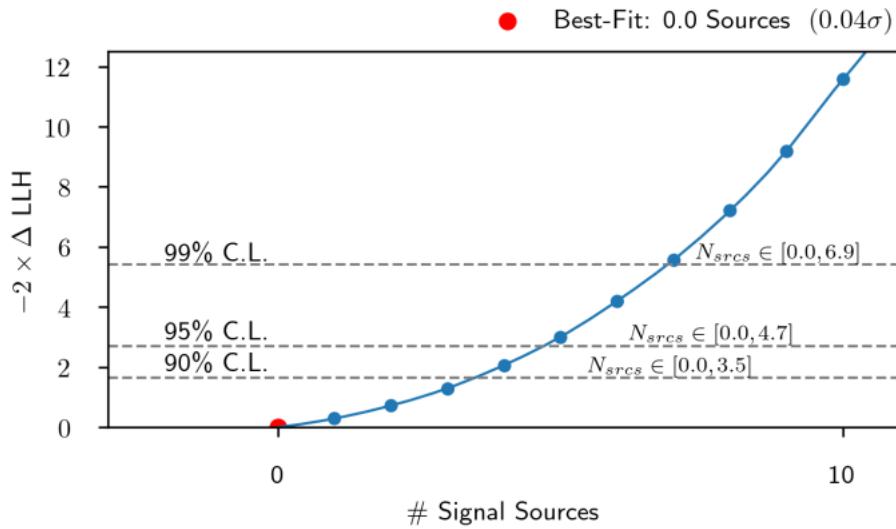
Figure 6.6: The profile likelihood for the class of LBLs from Giommi et al. (2020). As no significant detection is found, an upper limit on $N_{src}^{UL} = 3.48$ at 90% CL has been placed.
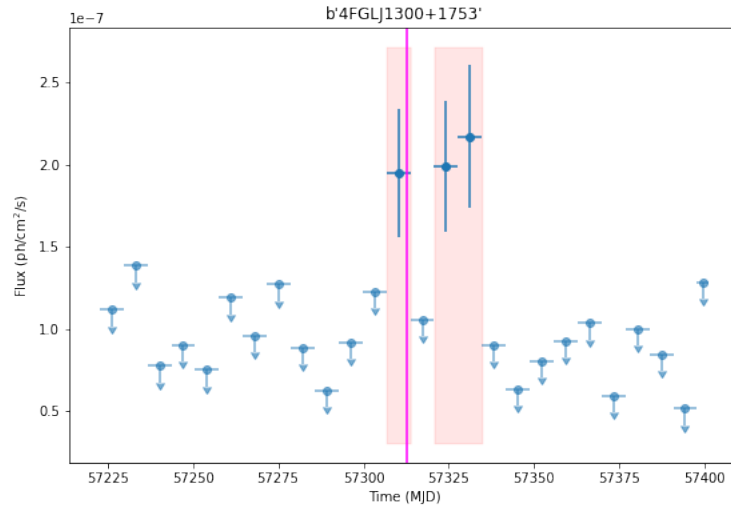
Figure 6.7: An example of coincidence between the arrival time of the neutrino event and a flaring state of the source in the 7-days binned light curve of 4FGL J1300+1753. The vertical line is the neutrino arrival time. The 7-days interval centered on each detection is highlighted.
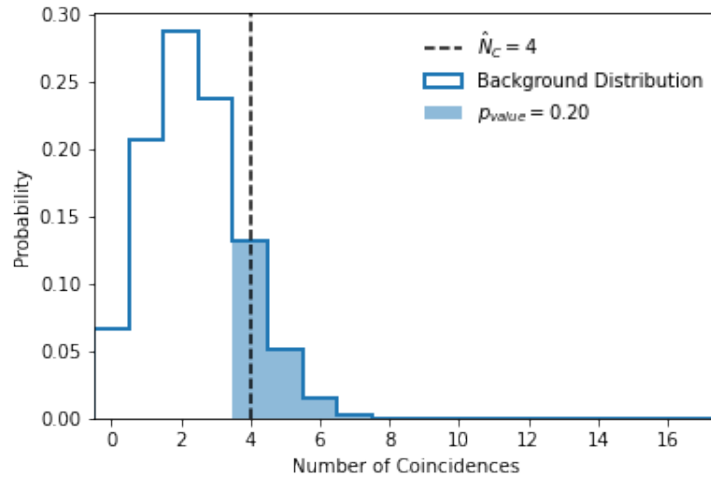
Figure 6.8: Probability of the number coincidences between a flaring state of the source and a neutrino event for $N_{trials} = 10^7$ for the class of HBLs/IBLs. The most probable value is $N_{coinc} = 2.39$, while the observed value is $N_{obs\_coinc} = 4$, corresponding to a p-value $p = 0.2$.
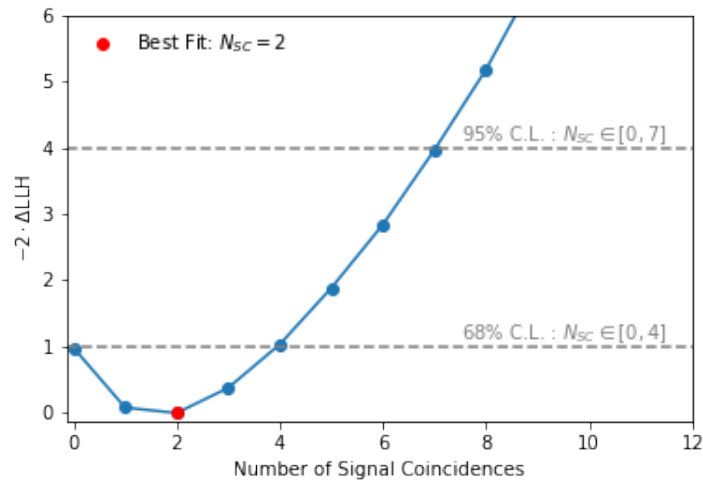
Figure 6.9: The profile likelihood for the class of HBLs/IBLs. The best fit is a number of 2 signal coincidences.
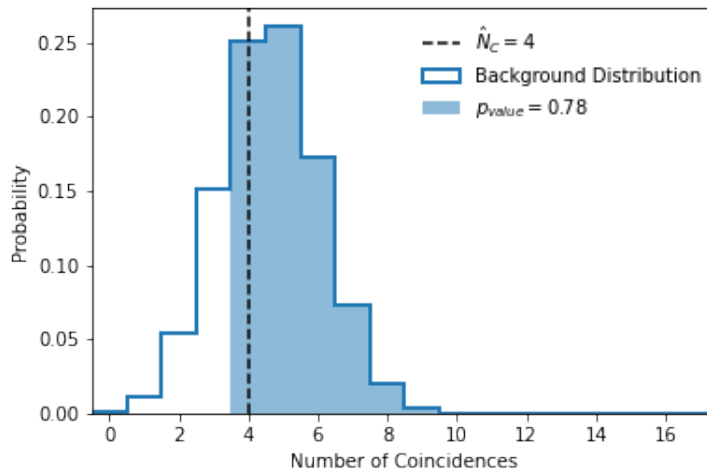
Figure 6.10: Probability of the number coincidences between a flaring state of the source and a neutrino event for $N_{trials} = 10^7$ for the class of HBLs/IBLs. The most probable value from random trials is $N_{exp_c oinc} = 4$, equal to the observed number of coincidences.
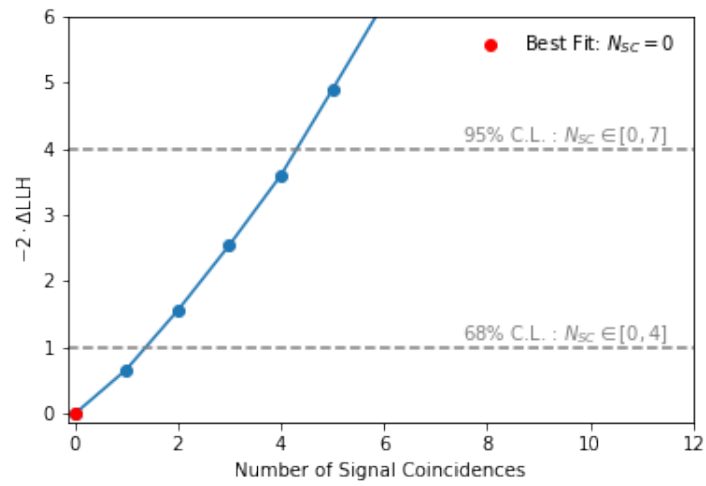
Figure 6.11: The profile likelihood for the class of LBLs. No significant detection is found.

Chapter 7

Discussion and future perspectives

The search for the astrophysical sources of cosmic neutrinos has been fueled by the association of the event IceCube-1700922A with the blazar TXS 0506+056 at the 3σ confidence level. The discovery encouraged further studies in the field of blazar-neutrino connection. In this work, we investigated for the first time *temporal* coincidence between flaring γ-ray activity of *Fermi*-detected blazars (Tab. 5.2 and Tab. 5.3) and the arrival time of IceCube neutrino events (Tab. 5.1). The *spatial* coincidence between this sample of events and the associated blazars has been studied in Giommi et al. (2020): the sources were selected for being in the $\Omega_{90\times1.5}$ error ellipse (area smaller than a circle with radius 3°) of the events.

First, the 8-years light curves with 2-months binning provided by the *Fermi* collaboration were inspected, in order to have a full view of the behaviour of the sources on long time scales. Then, the short-time variability of the sources was studied by building 6-months, 3-months and 1-month light curves, respectively with a bin size of 7-days, 3-days and 2-days, centered on each associate IceCube event. A full *Fermi* binned likelihood analysis was performed in each bin.

The sample is composed of 61 blazars belonging to 3 different classes: HBLs (27), IBLs (15) and LBLs (19). The classification is based on the position of the synchrotron peak in the SED of each object (see Sec. 3). Sources belonging to different classes show a different behaviour in the energy range covered by this analysis ($0.1 - 300$ GeV). The high-energy peak may occur in the *Fermi* energy range for LBLs, making these objects easier to detect, while it is usually located at higher energies (TeV range) for HBLs and IBLs: sources belonging to these classes are thus fainter in the *Fermi* energy band.

This global behaviour is well reflected in our light curves: the rate of detection ($TS > 9$) in the 6-months, 3-months and 1-month light curves, quantified by a N percentage parameter defined as $N = N_{det}/N_{bins} \times 100$, with N_{det} number of

detections and N_{bins} the total number of bins, is considerably higher for LBLs than for IBLs and HBLs (Fig. 6.1). As a consequence, we were forced to adopt different criteria for the selection of *flaring* blazars belonging to different classes. Our approach was driven by the temporal behaviour of TXS 0506+056: a detailed study of the γ-ray light curves of this source on each time scale was indeed performed.

- LBLs were considered *flaring* based on the display of *TXS-like* features in the 6-months light curves with 7 days binning: a $> 3\sigma$ variability and a value $N \geq 50\%$;

- HBLs and IBLs were considered *flaring* when at least two detections above the average flux value are found in the one month interval close in time to the neutrino event in the 6-months light curves with 7-days bin size.

According to these criteria, 6 sources (4 LBLs, 1 HBL and 1 IBL) were selected and discussed in Chap. 6. The presence of a *flare-neutrino coincidence* was stated when a neutrino event was found in the 7 days interval centered on a detection. This was observed in 4 sources out of 6, while we excluded the light curves featuring only upper limits around the neutrino event.

The origin of the observed coincidences was inspected from a statistical point of view with a random coincidence analysis in Chap. 6.3. In Giommi et al. (2020) a statistical excess of 3.23σ over background expectations is found for the HBL/IBL blazars in correspondence to IceCube neutrino positions, while no excess is found for LBL blazars. Following the same approach, we performed separated random coincidence tests for HBLs/IBLs and LBLs. We defined each detection with $TS > 9$ as a *flaring* state for HBLs and IBLs and searched *coincident* (defined as the one-week interval centered on each detection) emission between γ-rays and neutrinos. The definition of *flaring* state for LBLs would require a more cautious approach, given the different observed values of N for these sources. However, as a first step, we adopted the same definition (detection with $TS > 9$) chosen for HBLs/IBLs for LBLs as well. We found that:

- An excess of 2 coincidences is found for the HBL/IBL blazar classes, with a p-value $p = 0.2$: the result is not statistically relevant.

- No excess over the background expectations is found for LBLs, in agreement with the results of Giommi et al. (2020).

As expected from the spatial coincidence analysis presented in Giommi et al. (2020), LBLs seem to be disfavoured as neutrino counterparts, while the association appears more likely for HBLs and IBLs. The significance of the temporal coincidences is, however, statistically not relevant. We investigated the possible reasons beyond this evidence. We propose three hypotheses:

- *We do not detect enough temporal coincidences because of statistical reasons*:
  HBLs and IBLs are faint sources in the energy range covered by *Fermi*, the
  variability on time scales shorter than 7 days could not be fully investigated
  in this work ($N \sim 0\%$, see Fig. 6.1). As a consequence, if the neutrino events
  had been accompanied by a fast flaring episode (< 7 days), *Fermi* would not
  be able to detect it.

- *We do not detect enough temporal coincidences because the emission of a cos-
  mic neutrino is a rare event caused by a special subclass of TXS-like sources
  and a γ-ray flare is not expected (Halzen et al. 2019).* As discussed in Sec. 3.3,
  the expected γ-ray activity from TXS 0506+056-like neutrino emitters has
  been studied in Halzen et al. (2019). From a study of the γ-ray emission of
  the blazar during the dominant neutrino flare in 2014 it is found that ab-
  sorption and interactions intrinsic to the source, followed by the interaction
  with EBL, will result in a gamma ray flux consistent with the *Fermi* observa-
  tions. In other words, a γ-ray flare is not expected to occur when the source
  is a highly efficient neutrino emitter. It is worth noticing that, according
  to Halzen et al. (2019), these sources would constitute only $\sim 5\%$ of the
  total blazar population. Moreover, Halzen et al. (2019) suggest a connection
  between accretion events onto the SMBH and the emission of neutrino flare:
  this scenario would imply a major role for FSRQs such as PMN J1916-1519
  and TXS 1318+225, two of the selected sources from this sample, in the
  cosmic neutrino production, despite these blazars belong to the statistically
  disfavoured class of LBLs.

- *We do not detect enough temporal coincidences because the neutrino flux
  from the source is better correlated with the flux in other energy bands, e.g.
  the X-rays.* In Petropoulou et al. (2020), a *hybrid model* is proposed for the
  high-energy emission of TXS 0506+056 in coincidence with IceCube-170922A
  where the high-energy emission from the source is explained by synchrotron
  and inverse Compton processes of accelerated electrons that are injected in
  a localized region and a population of relativistic protons is injected in the
  same region. In this picture, the highest maximal neutrino flux should fol-
  low more closely the changes in the soft X-ray flux probed by *Swift*-XRT
  (up to 10 keV) than the γ-ray flux in the *Fermi*-LAT band. From the re-
  quirement that the proton-induced emission does not overshoot the observed
  X-ray and γ-ray data, it follows that the maximal neutrino flux should be
  reached when the source is in a bright X-ray state. Similar results are inde-
  pendently obtained in Gao (2019), where the existence of *orphan* neutrino
  flares, not accompanied by γ-ray flares but coincident with intense X-ray
  activity, is justified in the frame of a *hybrid* emission model. This underlines

the importance of multi-wavelength studies for a full understanding of the connection between blazars and neutrinos and could explain the lack γ-ray flaring activity in our sample.

These considerations are motivated by the fact that the FSRQs PKS 1502+106, the suggested counterpart of the event IceCube-190730A, is a part of the sample defined in Chap. 5 but does not satisfy the criteria defined in Chap. 6. This source is detected with $N > 50\%$ in the 6-months light curve with 7-days binning, but it does not reach the 3σ threshold for variability.

As anticipated in Sec. 3.3, the correlation between the emission from PKS 1502+106 and IceCube-190730A was inspected through a multi-wavelength study in Rodrigues et al. (2020). According to the lepto-hadronic and proton-synchrotron models adopted in this analysis, the neutrino flux is expected to scale with X-rays, co-produced inside the source during the cascade (see Sec. 3). The results are compatible with the observation of a neutrino event during a quiescient γ-ray state of the source. Moreover, the observation of a radio outburst of the source with OVRO (Franckowiak et al. 2020) reveals that, when IceCube-190730A was detected, PKS 1502+106 was in a high radio state (Fig. 7.1), showing a similar behaviour with TXS 0506+056 at the arrival time of IceCube-170922A. This strengthens the hypothesis that, despite not being associated with a flaring γ-ray activity of the source, the neutrino event IceCube-190730A could be correlated with the FSRQ PKS 1502+106.

To sum up, the future perspective for this work include:

- A refined statistical test for the LBLs in this sample (Tab. 5.2 and Tab. 5.3) with a definition of *flaring* state adequate to this class of sources.

- The study of temporal coincidences between the blazars in this sample (Tab. 5.2 and Tab. 5.3) and the neutrino events in the X-ray band following the model described in Petropoulou et al. (2020).

- The simulation of the SEDs of the sources in this sample (Tab. 5.2 and Tab. 5.3) as they would be observed by the next-generation of γ-ray telescopes, such as the Cherenkov Telescope Array, with the purpose to assess the capability of the instrument in discriminating among different *hybrid* models for the high-energy emission of the selected blazars.

The future perspectives for neutrino astronomy linked to the Cherenkov Telescope Array are briefly discussed in the following section.
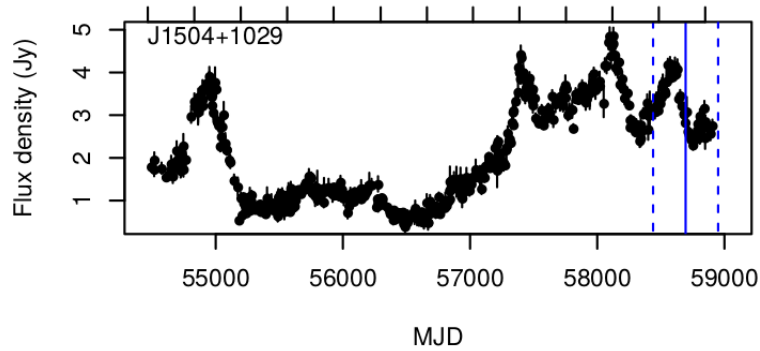
Figure 7.1: OVRO 15 GHz light curve of PKS 1502+106. The blue solid line marks the arrival time of IceCube-190730A, while the dashed lines highlight the 2.3 yr time window around the event. Credits: Hovatta et al. (2020)

7.1 Future perspectives

The study of temporal coincidence between γ-ray emission and neutrino emission from blazars carried out in this work was hampered by the lack of statistics in the *Fermi* energy band for the classes of HBL and IBL blazars. The low values of the N detection rate (Fig. 6.1) for these sources prevented a full investigation of their γ-ray activity on time scales ≤ 7 days. Therefore, the presence of fast γ-ray flaring episodes in coincidence with the neutrino events can not be excluded only on the basis of our work.

Given the position of their high-energy peak ($\sim$TeV), the detection of HBL and IBL blazars could be improved by the next generation of VHE instruments, such as the Cherenkov Telescope Array (CTA).

CTA is the next generation ground-based observatory for γ-ray astronomy at very-high energies in the range from 20 GeV to 300 TeV. It will provide a wider energy range and better angular resolution and sensitivity when compared to any existing γ-ray detector (see Fig. 7.2). To achieve all-sky coverage, CTA will consist of two arrays, one in each hemisphere, with the northern array consisting of 19 telescopes spread over 1 km^2 in La Palma and the southern array consisting of 99 telescopes spread over 4 km^2 in Chile. The construction completion of the project is planned for 2025[1].

The differential sensitivity of the CTA, defined as the minimum flux required by the instrument to obtain a 5σ detection of a point-like source, is shown in Fig. 7.3. The minimum detectable flux is reached at ~ 3 TeV both for the Southern and Nothern Array.

The performance of CTA will bring major advantages in the study of transient

---

[1]https://www.cta-observatory.org/project/status/

astrophysical messengers such as neutrinos: the telescopes in the two arrays are designed to rapidly re-position ($\sim$ 30 seconds) to any location in the sky and their large field of view ($\sim$ 4.5° to $\sim$ 9° depending on the telescope size) will allow to maximize the sky coverage. In the CTA transient key science program (KSP) a total of 5 hours per site, per year, has been allocated to high-energy neutrino events observations, during the first 10 years of CTA operations. The Target of Opportunity program for neutrinos in CTA has been presented in Satalecka et al. (2019).

Simulations of the CTA follow-up observations triggered by IceCube alerts on TXS 0506+056-like sources as defined in Halzen et al. (2019) have been carried out depending on the flaring source fraction F and the array configuration. The results are shown in Fig. 7.4: in the case of $F = 0.5\%$ (Halzen et al. 2019) CTA has a $\sim$ 30% chance of detection, assuming that 50% of the IceCube alerts correspond to real sources and all of them are observable by CTA. CTA prospects are then particularly promising for neutrino sources similar to the 2014-1015 neutrino flare by TXS 0506+056.
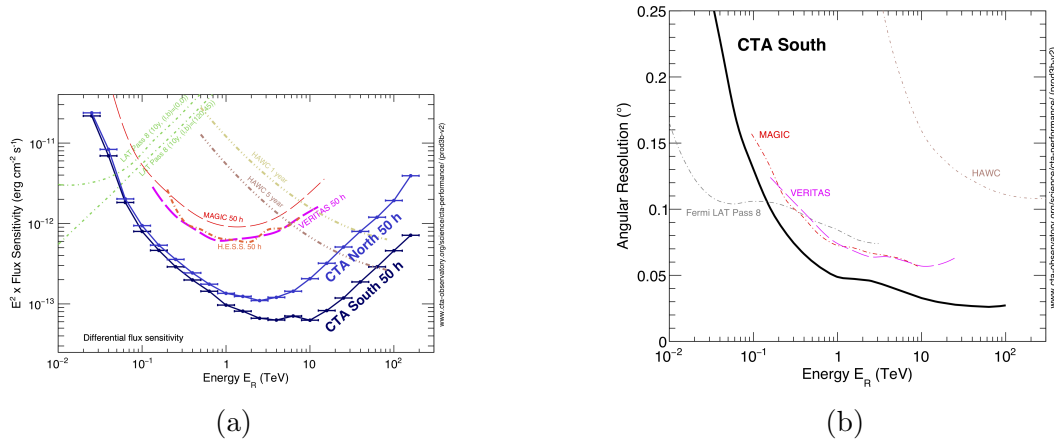
Figure 7.2: CTA sensitivity (*Left*) and angular resolution (*Right*) for the Southern and Nothern array compared to the performances of other γ-ray instruments. Credits: CTA Observatory.
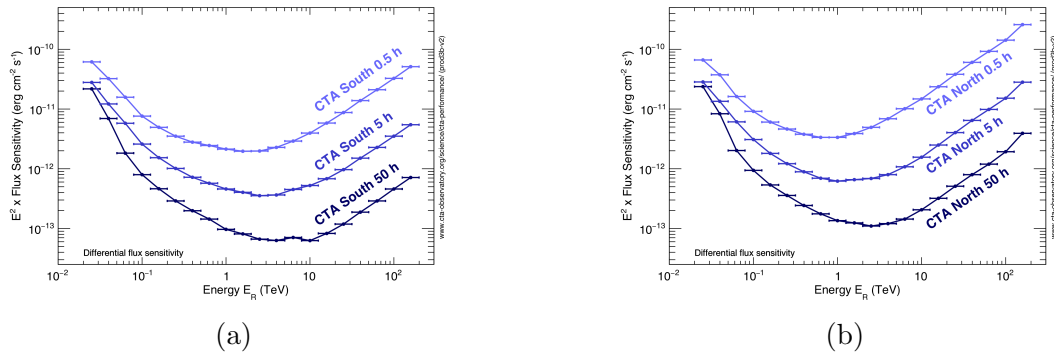
Figure 7.3: CTA sensitivity for the Southern Array (*Left*) and for the Nothern Array (*Right*). The optimal cut values depend on the duration of the observation, therefore the instrument response functions are provided for three different observation times: 0.5, 5 and 50 hours. Credits: CTA Observatory.
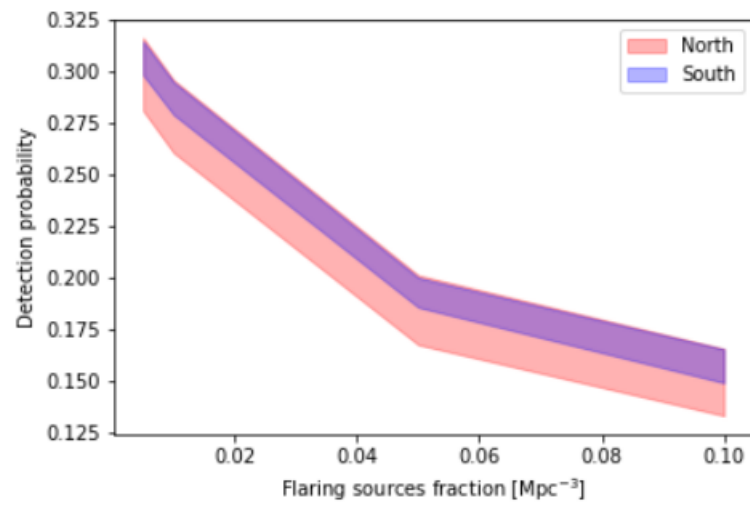
Figure 7.4: Probability to detect a neutrino source as a function of the flaring sources fraction F. Credits: Satalecka et al. (2019).

Appendix A

Notes on the subsample of *flaring* blazars

Here, we present the properties of the 6 γ-ray sources selected in Chap. 6 for being in a *flaring* state in the 6-months interval centered on the associated IceCube event. The 3-months and 1-month light curves of these blazars are presented.

A.1   4FGL J0428.6-3756

The γ-ray source 4FGL 0428.6-3756 is associated with the BL Lac PKS 0426-380 (Abdollahi et al. 2020) with preferred redshift $z = 1.11$ (Heidt et al. 2004). The source is classified as a LBL.

PKS 0426-380 has been reported to show year-like Quasi Periodic Variations at high energies ($E > 100$ MeV) with significance $> 3\sigma$ ((Ait Benkhali et al. 2020), (Covino et al. 2019)). These results are inferred from only 10 years of observations, the claim that this source is actually a Quasi Periodic Oscillator should therefore be handled carefully. Several physical processes have been invoked to explain the presence of QPOs: the presence of binary black hole systems is an example. In addition, a scenario based on the quasi periodic modulation between standard and ADAF accretion flow has been proposed (Ait Benkhali et al. 2020).

The Quasi Periodic Variations of PKS 0426-380 are visible in Fig. A.1a and Fig. A.1b.

The FSRQ is spatially correlated with the neutrino event IceCube-190504A (Ω_{90} ellipse). The LBL 4FGL J0420.3-3745 was found in the 90% error region of the event as well. However, it was not included in this selection due to the lack of statistics ($N < 50\%$).

The light curve in Fig. A.1b shows that the event is coincident with the peak of a local flare in the γ-ray emission from the source. The behaviour of 4FGL

0426-380 has been further inspected using the 6-months, 3-months and 1-month light curves centered on IceCube-190504A (Fig. A.1).

For the 6-months light curve of PKS 0426-380, a $Var/dof = 10.6$ is obtained (Tab. **??**), the source shows indeed signs of variability on the selected time scale. Despite that, the peak of the γ-ray flux is reached six weeks after the arrival of the neutrino (Fig. A.1c). This is confirmed in Fig. A.1d: it is not possible to state a *coincidence* between the increased emission and the arrival time of the neutrino.

A.2   4FGL J0948.9+0022

The γ-ray source 4FGL J0948.9+0022 is associated to PMN J0948+0022, a Narrow Line Seyfert 1 galaxy (NLS1) which displays typical features of FSRQ, such as a double-humped SED, high variability and the presence of relativistic jets. The detection of the source in γ-rays with *Fermi*-LAT suggested that it could be an archetype of γ-ray emitting NLS1 galaxies (Doi et al. 2019).

The source is located at $z = 0.59$, the mass of its central SMBH is $M = 1.5 \times 10^8$ M$_\odot$ and it is a LBL.

The 0.1-300 GeV light curves of PMN J0948+0022 since 2008 to 2020 are illustrated in Fig. A.2a and Fig. A.2b.

The γ-ray flaring activity of PMN J0948+0022 in July 2010 has been studied in detail with a multi-wavelength follow-up campaign (Foschini et al. 2011). During the flare, the γ-ray emission from the source was enhanced by a factor 5. The high-energy activity was accompanied by an increased emission in optical and radio (OVRO).

A second γ-ray flaring episode was reported between December 2012 and January 2013 (D'Ammando et al. 2015). The subsequent follow-up multi-wavelength campaign included VHE data from the imaging Cherenckov telescope VERITAS, but no significant emission from the source was reported at $\sim$TeV energies. Conversely, the optical and radio light curves showed signs of flaring activity simultaneously to the γ-ray peak.

In Zhang et al. (2017), the γ, optical and radio light curves of the source were inspected in search for signs of Quasi Periodic Oscillations. The presence QPO activity of PMN J0948+0022 with a period of ~ 409 days was suggested by data.

The source is spatially correlated with the neutrino event IceCube-190819A (Giommi et al. 2020) ($\Omega_{90 \times 1.5}$). The error region of the event included the HBLs 4FGL J1003.4+0205 ($\Omega_{90 \times 1.3}$) and 4FGL J0946.2+0104 (Ω_{90}). As shown in Fig. **??**, the arrival time of the neutrino event is coincident with the peak of a local flare of γ-ray flux from the source. The 6-months, 3-months and 1-month light curves centered on the event are illustrated in Fig. A.2.

In Fig. A.2c and A.2d it can be seen that the peak in the γ-ray flux occurs 3

weeks after the neutrino event. The variation index for the 6-months light curve is $Var/dof = 2.6$, with a p-value of 1.5×10^{-5}: the light curve shows signs of variability at a $> 3\sigma$ confidence level. Nonetheless, the neutrino arrival time is coincident with a low γ-ray state of the source; no coincidence can then be state between the event and a flaring γ-ray activity.

A.3   4FGL J1916.7-1516

The 4FGL source 4FGL J1916.7-1516 is associated with PMN J1916-1519, a Flat Spectrum Radio source (Healey et al. 2007) at unknown redshift. It has been included in the blazar sample of Giommi et al. (2020) as a LBLs; its SED has been built with the VOUBlazar tool. The source is the only blazar spatially correlated with the neutrino event IceCube-131204A (MJD = 56630.47) (Giommi et al. 2020).

The light curves of the source are shown in Fig. A.3. The arrival time of IceCube-131204A is located in the vicinity of the peak of the flare in Fig. A.3a. The source is in an enhanced state (a factor ~ 10 above average) of γ-ray emission in coincidence with the neutrino event. The variation index of the 6-months light curve is $Var/dof = 3.7$ (Tab. **??**), the corresponding p-value is 7.4×10^{-10}. A detection coincident with the neutrino arrival time is seen with $TS \sim 100$. The high detection rate in the days following the IceCube event is visible in Fig. A.3c and Fig. A.2e as well.

A.4   4FGL J1321.1+2216

The 4FGL γ-ray source 4FGL J1321.1+2216 is associated with the LBL TXS 1318+225, a flat-spectrum radio quasar (Healey et al. 2007). In Giommi et al. (2020), TXS 1318+225 was found to be spatially correlated to the event IceCube-151017A in the $\Omega_{90 \times 1.5}$ ellipse. The IBLs 4FGL J1314.7+2348 and 4FGL J1300.0+1753 and the HBL 3FGL J1258.4+2123 were found in the same error region. The γ-ray light curve of the source from 2008 to 2016 is shown in Fig. A.4a.

The flaring γ-ray activity of the source at MJD~ 56250 (November 2012) was accompanied by an increased optical luminosity (Frolova et al. 2012).

At the arrival time of IceCube-151017A (57312.70 MJD) Fig. A.4a shows a factor 2 increase in the γ-ray flux. The situation was inspected with the 6-months, 3-months and 1-month light curves centered on the event (Fig. A.4). As shown in Fig. A.4b, the increase of flux reaches its maximum five weeks before the arrival of the neutrino event. The neutrino arrival time is nonetheless coincident with a low γ-ray state of the source.

A.5   4FGL J1117.0+2013

4FGL J1117.0+2013 is associated with RBS 0958, an HBL located at $z = 0.14$. Among HBLs in the sample, this source showed the highest variability in the 6-months, 7-days binned light curve, $\sim 20\%$.

RBS 0958 is considered a candidate TeV emitter based on the position of its synchrotron peak (Costamante et al. 2001). The source was observed HESS, the array of imaging Cherenkov telescopes in Namibia, and an integral flux upper limit $I(> E_{th}) = 1.44 \times 10^{-12}$ ph/cm^2/s ($\sim 3\%$ Crab Nebula) was obtained for $E_{th} = 610$ GeV with a live time of 3.8 h (Aharonian et al. 2005).

The optical emission from the source has been long-term monitored in R-band and it has been found to be significantly variable by applying a chi-square test (Nilsson et al. 2018).

The SED of RBS 0958 has been fitted with a power-law model with index $\gamma = 1.95$. The source has been found to be spatially correlated with the neutrino event IceCube-130408A (HESE alert, MJD = 56390.14). The LBL 4FGL J1059.5+2057 and the HBLs 4FGL J1124.0+2045 and 4FGL J1124.9+2143 were found in the 90% error region of the event as well. The 4FGL 2-months binned light curve of the source from 2008 to 2016 is shown in Fig. A.5a, while the 6-months, 3-months and 1-month light curves are shown in Fig. A.5.

In Fig. A.5b, a detection coincident with the neutrino event arrival time is shown with $F \sim 0.7 \times 10^{-7}$ ph/cm^2/s, a ~ 3 factor higher than average. In Fig. A.5c, the highest flux following the neutrino event is $F \sim 1.2 \times 10^{-7}$, ~ 5 times higher than average. The lack of statistics in Fig. A.5d prevents further investigation.

A.6   4FGL J1300.0+1753

The γ-ray source 4FGL J1300.0+1753 is associated with the IBL SDSS J130008.52+175538.0, at redshift $z = 1.54$. This object has been found in the $\Omega_{90 \times 1.5}$ ellipse of the IceCube-151017A event (see Sec. A.4).

Despite not being a candidate variable object according to its V parameter ($V < 18.48$, see Tab. **??**), this source was included in the selection due to the increase of flux in the vicinity of the neutrino event.

As we can see in Fig. A.6a, the event is coincident in time with a factor ~ 2 increase of flux from the source above the average value. In Fig. A.6b, the source is shown to have an average flux value of 8.47×10^{-8} ph/cm^2/s in the 6-months, 7-days binned interval around the event. The three $TS > 9$ detections are above this average value (factor ~ 2) and they are detected in the one-month interval around

the neutrino event. The lack of statistics in Fig. A.6c and Fig. A.6d prevents further investigation.
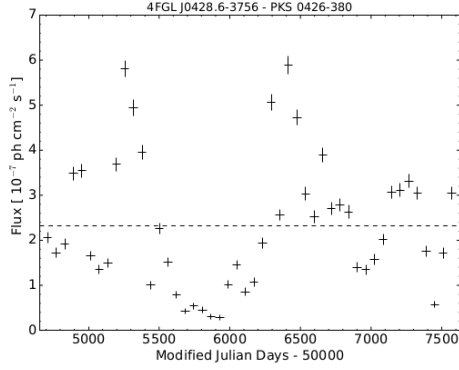
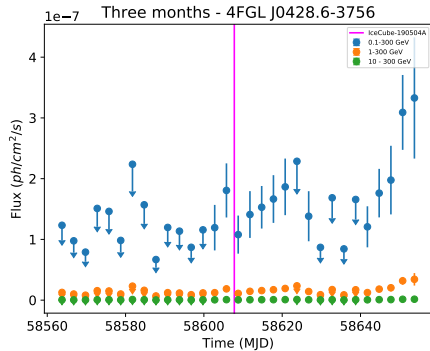(a) 2-months binned light curve of PKS 0426-380 from 4FGL from August 2008 (54700 MJD) to July 2016 (57600 MJD). Upper limits for $TS < 25$. The dashed line is the mean flux of the source.
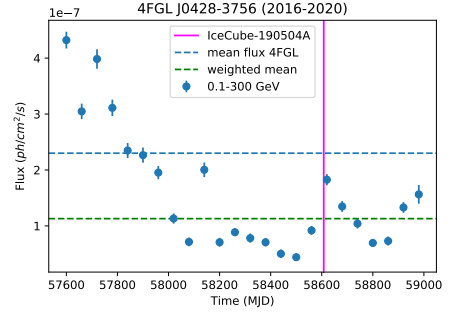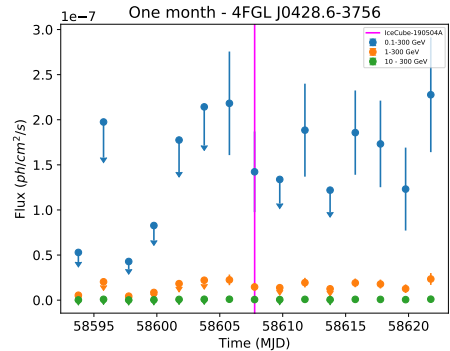
(b) 2-months binned light curve of PKS 0426-380 from July 2016 (57600 MJD) to May 2020 (59000 MJD). Upper limits for $TS < 25$. The mean flux from 4FGL and the mean flux between 2016 and 2020 are shown as dashed lines.
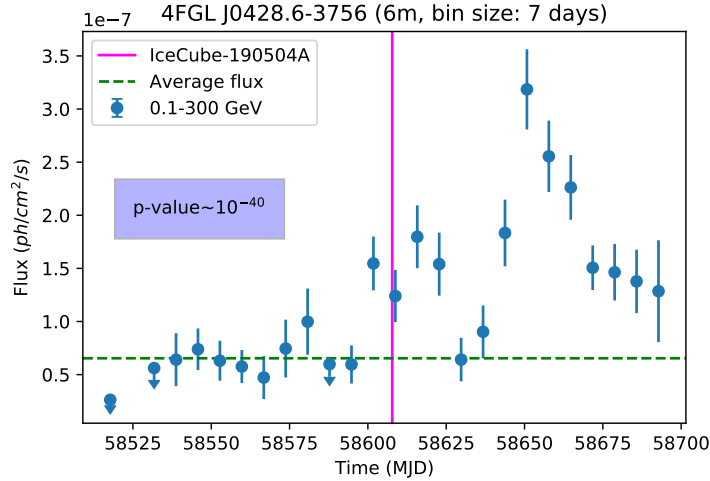
(c) 6-months, 7-days binned light curve of PKS 0426-380 centered on the arrival time of IceCube-190504A (58607.77 MJD). The dotted green line is the average flux of the source. Upper limits for points with $TS < 9$.)

(d) 3-months, 3-days binned light curve of PKS 0426-380 centered on the arrival time of IceCube-190504A (58607.77 MJD). Upper limits for points with $TS < 9$.)

(e) 1-month, 2-day binned light curve of PKS 0426-380 centered on the arrival time of IceCube-190504A (58607.77 MJD). Upper limits for points with $TS < 9$.)
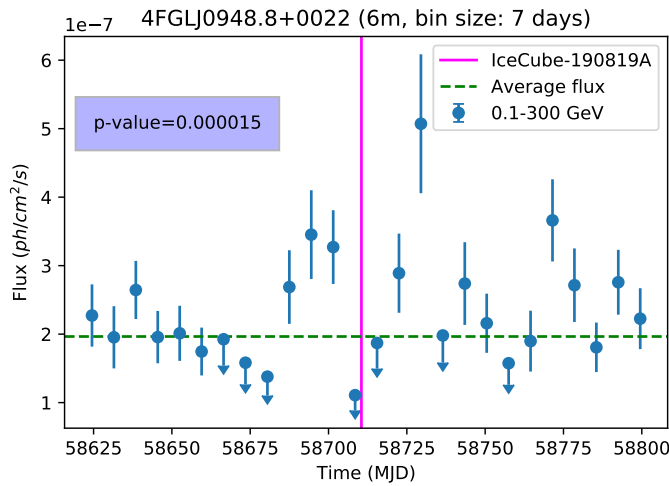
Figure A.1: Light curves of PKS 0426-380 between $0.1 - 300$ GeV, centered on the arrival time of IceCube-190504A (58607.77 MJD), with different binning.
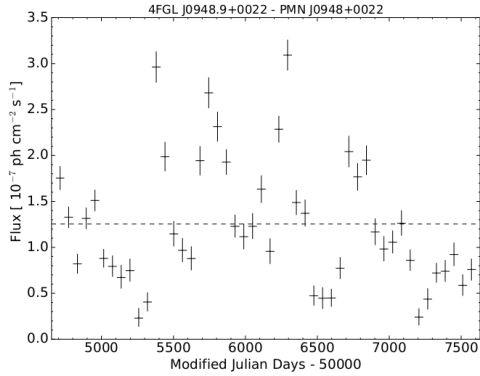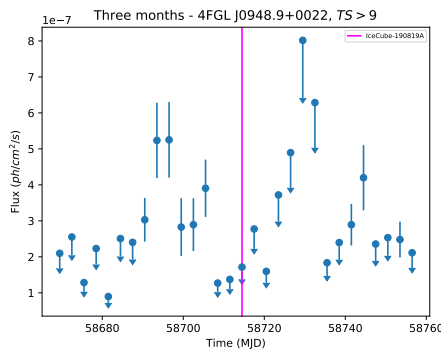
(a) 2-months binned light curve of PMN J0948+0022 from 4FGL from August 2008 (54700 MJD) to July 2016 (57600 MJD). Upper limits for detections with $TS < 25$. The dashed line is the average flux.
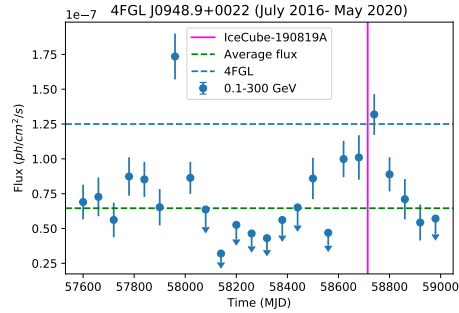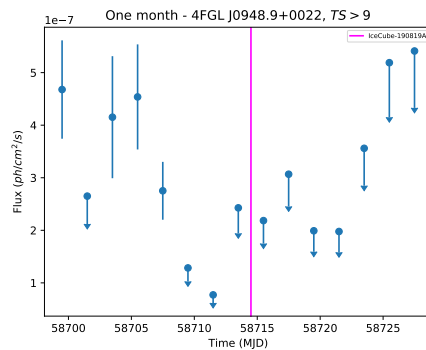
(b) 2-months binned light curve of PMN J0948+0022 from July 2016 (57600 MJD) to May 2020 (59000 MJD). Upper limits for detections with $TS < 25$. The mean flux from 4FGL and the mean flux between 2016 and 2020 are shown as dashed lines.

(c) 6-months, 7-days binned light curve of PMN J0948+0022 centered on the arrival time of IceCube-190819A (58714.50 MJD). The dashed green line is the average flux of the source. Upper limits for $TS < 9$.)
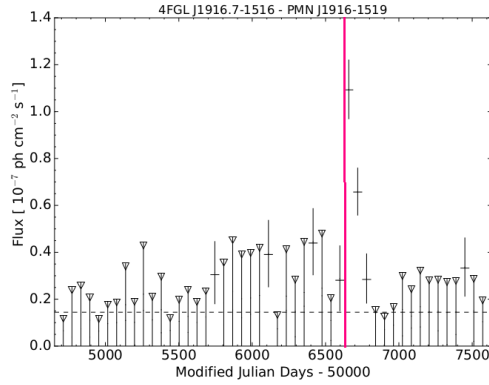
(d) 3-months, 3-days binned light curve of PMN J0948+0022 centered on the arrival time of IceCube-190919A (58714.50 MJD). Upper limits for $TS < 9$.)
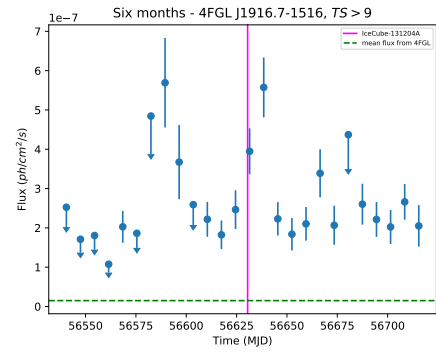
(e) 1-month, 2-day binned light curve of PMN J0948+0022 centered on the arrival time of IceCube-190504A (58714.70 MJD). Upper limits for $TS < 9$.)
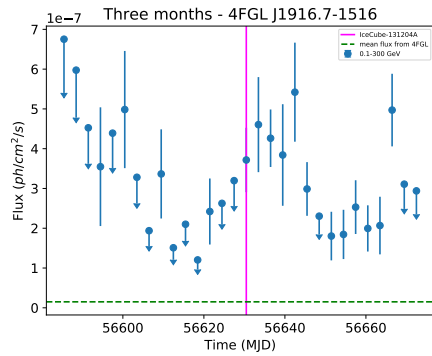
Figure A.2: Light curves of PMN J0948+0022 between $0.1 - 300$ GeV, centered on the arrival time of IceCube-190819A, with different binning.
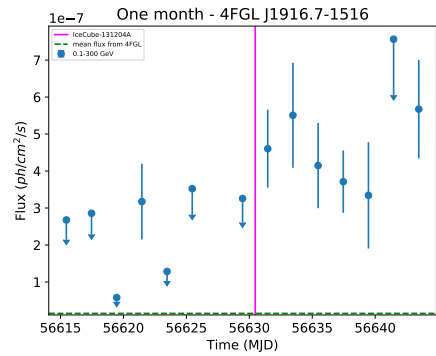
(a) 2-months binned light curve of PMN J1916-1519 in 2008-2016 time range (4FGL).

(b) 6-months,7-days binned light curve of PMN J1916-1519 centered on the arrival time of IceCube-131204A.
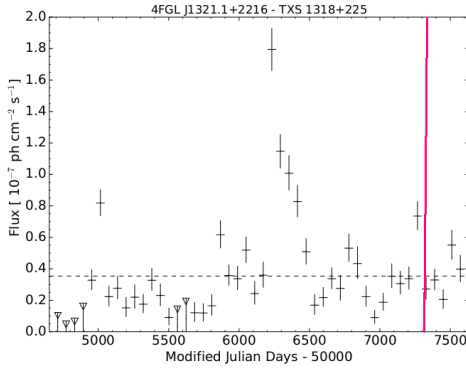
(c) 3-months, 3-days binned light curve of PMN J1916-1519 centered on the arrival time of IceCube-131204A.

(d) 1-month, 2-days binned light curve of PMN J1916-1519 centered on the arrival time of IceCube-131204A.

Figure A.3: Light curves of PMN J1916-1516 from 2008 to 2016 centered on the arrival time of IceCube-131204A (MJD = 56630.47), with different time binning.
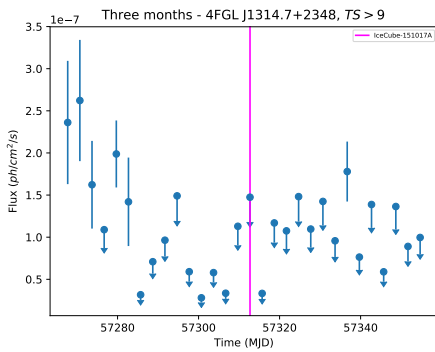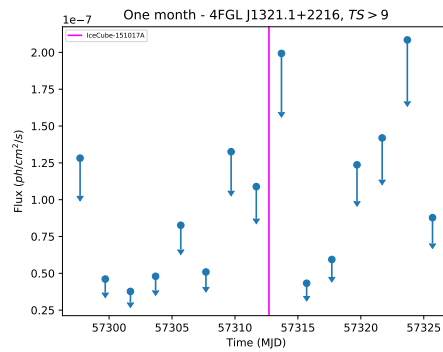
(a) 2-months binned light curve of TXS 1318+225 from 4FGL from August 2008 (54700 MJD) to July 2016 (57600 MJD). Upper limits for $TS < 25$.
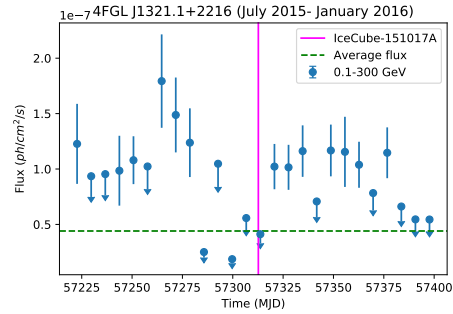
(b) 6-months, 7-days binned light curve of TXS 1318+225 centered on the arrival time of IceCube-151017A (57312.70 MJD). Upper limits for $TS < 9$.)
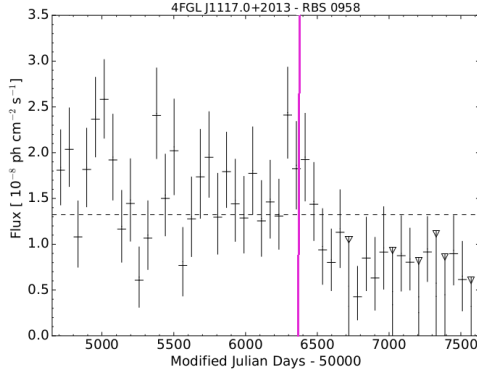
(c) 3-months, 3-days binned light curve of TXS 1318+225 centered on the arrival time of IceCube-151017A. Upper limits for $TS < 9$.
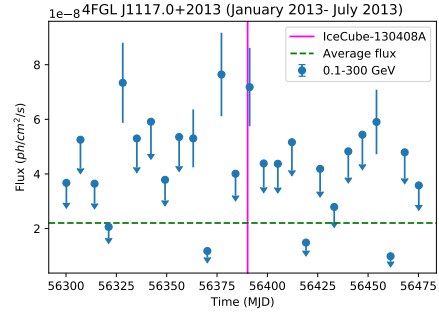
(d) 1-month, 2-day binned light curve of TXS 1318+225 centered on the arrival time of IceCube-151017A. Upper limits for $TS < 9$.

Figure A.4: Light curves of TXS 1318+225 between $0.1 - 300$ GeV, centered on the arrival time of IceCube-151017 (57312.70 MJD).

(a) 2-months binned light curve of RBS 0958 from 4FGL from August 2008 (54700 MJD) to July 2016 (57600 MJD). Upper limits for $TS < 25$.

(b) 6-months, 7-days binned light curve of RBS 0958 centered on the arrival time of IceCube-130408A (56390.19 MJD). Upper limits for $TS < 9$.
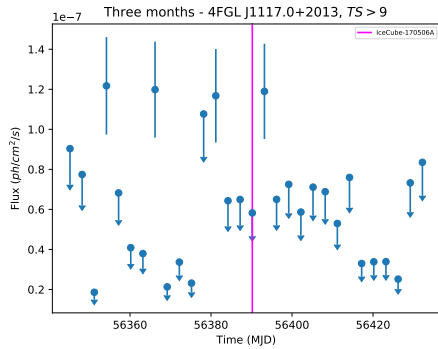
(c) 3-months, 3-days binned light curve of RBS 0958 centered on the arrival time of IceCube-130408A (56390.19 MJD). Upper limits for points with $TS < 9$.
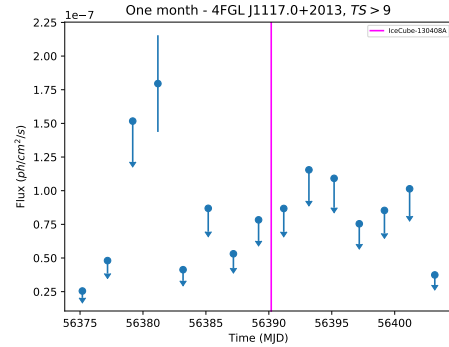
(d) 1-month, 2-day binned light curve of RBS 0958 centered on the arrival time of IceCube-130408A (56390.19 MJD). Upper limits for points with $TS < 9$.

Figure A.5: Light curves of RBS 0958 between $0.1 - 300$ GeV, centered on the arrival time of IceCube-130408A (56390.19 MJD).
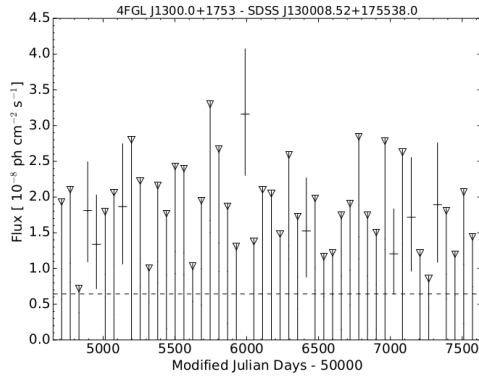
(a) 2-months binned light curve of 4FGL J1300.0+1753 from 4FGL from August 2008 (54700 MJD) to July 2016 (57600 MJD). Upper limits for $TS <$ 25.
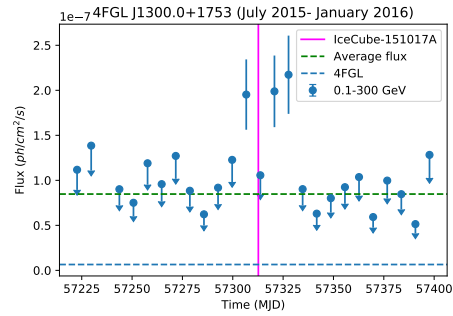
(b) 6-months, 7-days binned light curve of 4FGL J1300.0+1753 centered on the arrival time of IceCube-151017A (57312.70 MJD). Upper limits for $TS <$ 9.
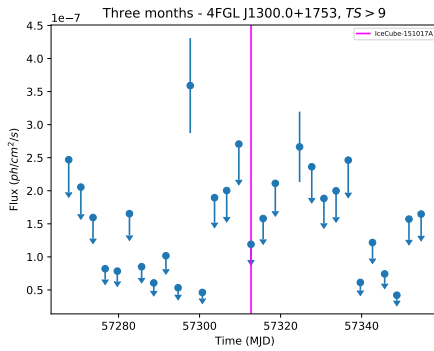
(c) 3-months, 3-days binned light curve of 4FGL J1300.0+1753 centered on the arrival time of IceCube-151017A. Upper limits for $TS < 9$.
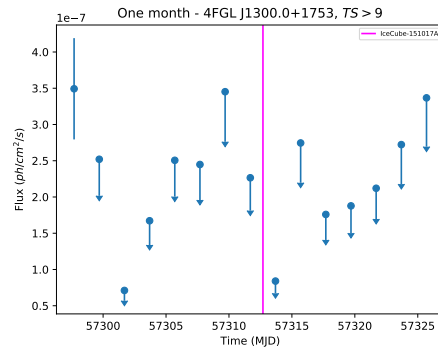
(d) 1-month, 2-day binned light curve of 4FGL J1300.0+1753 centered on the arrival time of IceCube-151017A. Upper limits for $TS < 9$.

Figure A.6: Light curves of 4FGL J1300.0+1753 in the $0.1 - 300$ GeV energy range, centered on the arrival time of IceCube-151017A (57312.70 MJD).

Appendix B

N values for the sample of blazar

Here, the full list of N values as defined in Chap. 6 is reported for each blazar listed in Tab. 5.2 and Tab. 5.3.

Table B.1: Sample of IceCube events from Giommi et al. (2020) successfully matched with 4FGL blazar and 3FGL and the associate value of the N parameter as defined in Chap. 6.

Event	Source	Class	N_{6m}	N_{3m}	N_{1m}
IceCube-160331A	4FGL J0103.5+1526	HBL	0%	0%	0%
IceCube-121011A	4FGL J1339.9-0138	LBL	0%	0%	0%
IceCube-190730A	4FGL J1504.4+1029	LBL	70.3%	80.6%	6.6%
IceCube-150831A	4FGL J0336.4+3224	LBL	3.7%	3.2%	0%
	4FGL J0344.4+3432	HBL	0%	0%	0%
IceCube-090813A	4FGL J0158.8+0101	IBL	19.2%	3.3%	0%
IceCube-161103A	4FGL J0239.5+1326	HBL	3.7%	0%	0%
	4FGL J0244.7+1316	IBL	0%	0%	0%
IceCube-190504A	4FGL J0428.6-3756	LBL	72%	80.6%	80%
	4FGL J0420.3-3745	LBL	9.1%	6.4%	6.6%
IceCube-141109A	4FGL J0339.2-1736	HBL	7.4%	0%	0%
IceCube-151114A	4FGL J0502.5+1340	LBL	29.9%	2.2%	2.6%
IceCube-140721A	4FGL J0648.0-3045	LBL	0%	0%	0%

	4FGL J0649.5-3139	HBL	0%	0%	0%
IceCube-130408A	4FGL J1117.0+2013	HBL	19.2%	13.8%	6.6%
	4FGL J1059.5+2057	LBL	3.8%	0%	0%
	4FGL J1124.0+2045	HBL	0%	0%	0%
	4FGL J1124.9+2143	HBL	0%	3.45%	0%
IceCube-190819A	4FGL J0946.2+0104	HBL	4%	0%	0%
	4FGL J1003.4+0205	HBL	0%	0%	0%
	4FGL J0948.9+0022	LBL	76%	30%	26%
IceCube-160814A	4FGL J1316.1-3338	LBL	30.8%	10%	6.6%
IceCube-140216A	4FGL J1404.8+6554	HBL	0%	0%	0%
IceCube-170506A	4FGL J1447.0-2657	HBL	0%	0%	0%
	4FGL J1440.0-2343	HBL	0%	0%	0%
	4FGL J1439.5-2525	IBL	0%	0%	0%
IceCube-110930A	4FGL J1744.2-0353	LBL	0%	0%	0%
IceCube-150714A	4FGL J2133.1+2529	HBL	0%	0%	0%
	4FGL J2133.0+2610	LBL	0%	0%	0%
IceCube-140114A	4FGL J2227.9+0036	IBL	0%	0%	0%
	4FGL J2226.8+0051	LBL	0%	0%	0%
	4FGL J2223.3+0102	HBL	0%	0%	0%
IceCube-141126A	4FGL J1231.5+1421	HBL	12%	6.7%	0%
IceCube-151017A	4FGL J1314.7+2348	IBL	3.8%	0%	0%
	4FGL J1300.0+1753	IBL	11.5%	6.7%	6.6%
	4FGL J1321.1+2216	LBL	50%	20%	0%
	3FGL J1258.4+2123	HBL	0%	0%	0%
IceCube-120515A	4FGL J1310.5+3221	LBL	4%	0%	0%
	4FGL J1311.0+3233	LBL	28%	10%	13.3%

	4FGL J1321.9+3219	IBL	0%	0%	0%
IceCube-131202A	4FGL J1341.8-2053	LBL	42.3%	13.6%	6.6%
IceCube-141209A	4FGL J1043.6+0654	IBL	0%	0%	0%
	4FGL J1040.5+0617	IBL	27%	22%	6.6%
IceCube-150428A	4FGL J0525.6-2008	IBL	0%	0%	0%
IceCube-160510A	4FGL J2326.2+0113	IBL	0%	0%	0%
IceCube-111216A	4FGL J0232.8+2018	HBL	0%	0%	0%
	4FGL J0224.2+1616	IBL	0%	0%	0%
IceCube-110521A	4FGL J1554.2+2008	HBL	3.8%	0%	0%
	4FGL J1533.2+1855	HBL	3.8%	0%	0%
	4FGL J1528.4+2004	HBL	3.8%	0%	0%
IceCube-150926A	4FGL J1258.7-0452	HBL	7.6%	0%	0%
IceCube-120123A	4FGL J1359.1-1152	IBL	0%	0% 0%	
IceCube-150911A	4FGL J1557.9-0001	LBL	15.4%	3.3%	0%
IceCube-110610A	4FGL J1808.2+3500	IBL	3.85%	0%	0%
	4FGL J1808.8+3522	HBL	7.6%	0%	0%
IceCube100710A	4FGL J2030.5+2235	HBL	0%	0%	0%
	4FGL J2030.9+1935	HBL	23%	0%	0%
IceCube-131204A	4FGL J1916.7-1516	LBL	69.2%	52.2%	50%
IceCube-190104A	4FGL J2358.1-2853	IBL	0%	0%	0%
	4FGL J2350.6-3005	HBL	0%	0%	0%
IceCube-170321A	3FGL J0627.9-1517	HBL	19.2%	0%	0%

Acknowledgements

Bibliography

Aartsen, M G, et al. 2014a. "Energy reconstruction methods in the IceCube neutrino telescope". *Journal of Instrumentation* 9, no. 03 (): P03009–P03009.

Aartsen, M. G., et al. 2016. "Observation and Characterization of a Cosmic Muon Neutrino Flux from the Northern Hemisphere Using Six Years of IceCube Data". *The Astrophysical Journal* 833, no. 1, 3 (): 3.

Aartsen, M. G., et al. 2014b. "Observation of High-Energy Astrophysical Neutrinos in Three Years of IceCube Data". *Phys. Rev. Lett.* 113, no. 10, 101101 (): 101101.

Aartsen, M. G., et al. 2017a. "The IceCube Neutrino Observatory: instrumentation and online systems". *Journal of Instrumentation* 12, no. 3 (): P03012.

Aartsen, M. G., et al. 2017b. "The IceCube realtime alert system". *Astroparticle Physics* 92 (): 30–41.

Abdo, A. A., et al. 2010a. "Fermi Large Area Telescope First Source Catalog". *ApJS* 188, no. 2 (): 405–436.

Abdo, A. A., et al. 2010b. "The Spectral Energy Distribution of Fermi Bright Blazars". *The Astrophysical Journal* 716, no. 1 (): 30–70.

Abdollahi, S., et al. 2020. "Fermi Large Area Telescope Fourth Source Catalog". *The Astrophysical Journal Supplement Series* 247, no. 1 (): 33. ISSN: 1538-4365.

Ackermann, M., et al. 2016. "2FHL: The Second Catalog of Hard Fermi-LAT Sources". *The Astrophysical Journal Supplements* 222, no. 1, 5 (): 5.

Ackermann, M., et al. 2013. "The First Fermi-LAT Catalog of Sources above 10 GeV". *The Astrophysical Journal Supplement* 209, no. 2, 34 (): 34.

Ackermann, M., et al. 2015. "The Third Catalog of Active Galactic Nuclei Detected by the Fermi Large Area Telescope". *The Astrophysical JournalFermi-LAT detection of increased gamma-ray activity of TXS 0506+056, located inside the IceCube-170922A error region.* 810, no. 1, 14 (): 14.

Aharonian, F. A. 2000. "TeV gamma rays from BL Lac objects due to synchrotron radiation of extremely high energy protons". *New Astronomy* 5, no. 7 (): 377–395.

Aharonian, F., et al. 2005. "Observations of selected AGN with HESS". *Astronomy & Astrophysics* 441, no. 2 (): 465–472.

Ahlers, Markus, and Francis Halzen. 2015. "High-energy cosmic neutrino puzzle: a review". *Reports on Progress in Physics* 78, no. 12 (): 126901.

— . 2018a. "Opening a new window onto the universe with IceCube". *Progress in Particle and Nuclear Physics* 102 (): 73–88.

— . 2018b. "Opening a new window onto the universe with IceCube". *Progress in Particle and Nuclear Physics* 102:73–88. ISSN: 0146-6410.

Ait Benkhali, F., et al. 2020. "Evaluating quasi-periodic variations in the γ-ray light curves of Fermi-LAT blazars". *Astronomy Astrophysics* 634 (): A120. ISSN: 1432-0746.

Ajello, M., et al. 2017. "3FHL: The Third Catalog of Hard Fermi-LAT Sources". *The Astrophysical Journal Supplement Series* 232, no. 2, 18 (): 18.

Angioni, R. et al. 2019. "The large gamma-ray flare of the flat-spectrum radio quasar PKS 034627". *Astronomy & Astrophysics* 627 ().

Ansoldi, S. et al. 2018. "The Blazar TXS 0506+056 Associated with a High-energy Neutrino: Insights into Extragalactic Jets and Cosmic-Ray Acceleration". *The Astrophysical Journal Letters* 863, no. 1, L10 (): L10.

Arsioli, B., et al. 2015. "1WHSP: An IR-based sample of ~1000 VHE γ-ray blazar candidates". *Astronomy & Astrophysics* 579, A34 (): A34.

Atwood, W. B., et al. 2009. "THE LARGE AREA TELESCOPE ON THEFERMI GAMMA-RAY SPACE TELESCOPEMISSION". *The Astrophysical Journal* 697, no. 2 (): 1071–1102. ISSN: 1538-4357.

Atwood, W., et al. 2013. *Pass 8: Toward the Full Realization of the Fermi-LAT Scientific Potential.*

Becker, Julia K. 2008. "High-energy neutrinos in the context of multimessenger physics". *Physics Reports*, no. 458: 173–246.

Begelman, Mitchell C., Andrew C. Fabian, and Martin J. Rees. 2008. "Implications of very rapid TeV variability in blazars". *Monthly Notices of the Royal Astronomical Society* 384, no. 1 (): L19–L23.

Bloom, Steven D., and Alan P. Marscher. 1996. "An Analysis of the Synchrotron Self-Compton Model for the Multi–Wave Band Spectra of Blazars". *The Astrophysical Journal* 461 (): 657.

Böttcher, M., et al. 2013. "Leptonic and Hadronic Modeling of Fermi-detected Blazars". *The Astrophysical Journal* 768, no. 1, 54 (): 54.

Braibant, Giacomelli, and Spurio. 2011. *Particle and Fundamental Interactions.* Springer-Verlag Mailand. ISBN: 978-88-470-2754-1.

Celotti, A., A. C. Fabian, and M. J. Rees. 1998. "Limits from rapid TeV variability of MRK 421". *Monthly Notices of the Royal Astronomical Society* 293, no. 3 (): 239–242.

Cerruti, Matteo. 2020. "Leptonic and Hadronic Radiative Processes in Supermassive-Black-Hole Jets". *arXiv e-prints*, arXiv:2012.13302 (): arXiv:2012.13302.

Cerruti, M, et al. 2018. "Leptohadronic single-zone models for the electromagnetic and neutrino emission of TXS0506+056". *Monthly Notices of the Royal Astronomical Society: Letters* 483, no. 1 (): L12–L16. ISSN: 1745-3925.

Chang, Y. -L., et al. 2017. "2WHSP: A multi-frequency selected catalogue of high energy and very high energy γ-ray blazars and blazar candidates". *Astronomy & Astrophysics* 598, A17 (): A17.

Chang, Y. -L., et al. 2019. "The 3HSP catalogue of extreme and high-synchrotron peaked blazars". *Astronomy & Astrophysics* 632, A77 (): A77.

Chang, Y.-L., C.H. Brandt, and P. Giommi. 2020. "The Open Universe VOU-Blazars tool". *Astronomy and Computing* 30:100350. ISSN: 2213-1337.

Chiarusi, T., and M. Spurio. 2010. "High-energy astrophysics with neutrino telescopes". *The European Physics Journal C* 65:647–701.

Costamante, L., et al. 2001. "Extreme synchrotron BL Lac objects. Stretching the blazar sequence". *Astronomy&Astrophysics* 371 (): 512–526.

Covino, S., A. Sandrinelli, and A. Treves. 2019. "Gamma-ray quasi-periodicities of blazars. A cautious approach". *Monthly Notices of the Royal Astronomical Society* 482, no. 1 (): 1270–1274.

Cowan, Jr., C. L., et al. 1956. "Detection of the Free Neutrino: A Confirmation". *Science* 124, no. 3212 (): 103–104.

D'Ammando, F., et al. 2015. "The most powerful flaring activity from the NLSy1 PMN J0948+0022". *Monthly Notices of the Royal Astronomical Society* 446, no. 3 (): 2456–2467.

Doi, Akihiro, et al. 2019. "Radio jet structures at $\sim$100 pc and larger scales of the γ-ray-emitting narrow-line Seyfert 1 galaxy PMN J0948+0022". *Monthly Notices of the Royal Astronomycal Society* 487, no. 1 (): 640–649.

Foschini, L., et al. 2011. "The first gamma-ray outburst of a narrow-line Seyfert 1 galaxy: the case of PMN J0948+0022 in 2010 July". *Monthly Notices of the Royal Astronomical Society* 413, no. 3 (): 1671–1677.

Franckowiak, A., et al. 2020. "Patterns in the Multiwavelength Behavior of Candidate Neutrino Blazars". *The Astrophysical Journal* 893, no. 2 (): 162.

Frolova, A., et al. 2012. "MASTER detection of optical activity from TXS 1318+225". *The Astronomer's Telegram* 4616 (): 1.

Gaisser, Thomas K., Francis Halzen, and Todor Stanev. 1995. "Particle astrophysics with high-energy neutrinos". [Erratum: Phys.Rept. 271, 355–356 (1996)], *Phys. Rept.* 258:173–236.

Gandhi, Raj, et al. 1998. "Neutrino interactions at ultrahigh energies". *Physical Review D (Particles and Fields)* 58, no. 9, 093009 (): 093009.

Gao, S. et al. 2019. "Modelling the coincident observation of a high-energy neutrino and a bright blazar flare". *Nature Astronomy*, no. 3: 88–92.

Ghisellini, G., and F. Tavecchio. 2009. "Canonical high-power blazars". *Monthly Notices of the Royal Astronomical Society* 397, no. 2 (): 985–1002. ISSN: 0035-8711.

Giommi, P. 2012. "A simplified view of blazars: clearing the fog around long-standing selection effects". *Monthly Notices of the Royal Astronomical Society* 420 (4): 2899–2911.

Giommi, P., P. Padovani, and G. Polenta. 2013. "A simplified view of blazars: the γ-ray case". *Monthly Notices of the Royal Astronomical Society* 431, no. 2 (): 1914–1922. ISSN: 0035-8711.

Giommi, P., et al. 2012. "Simultaneous Planck, Swift, and Fermi observations of X-ray and γ-ray selected blazars". *Astronomy&Astrophysics* 541, A160 (): A160.

Giommi, P, et al. 2020. "Dissecting the regions around IceCube high-energy neutrinos: growing evidence for the blazar connection". *Monthly Notices of the Royal Astronomical Society* 497, no. 1 (): 865–878. ISSN: 0035-8711.

Gonzalez-Garcia, M. C., and Michele Maltoni. 2008. "Phenomenology with massive neutrinos". *Physics Reports* 460, **numbers** 1-3 (): 1–129.

Halzen, F. 2006. "Astroparticle physics with high energy neutrinos: from AMANDA to IceCube". *The European Physics Journal C* 46:669–687.

Halzen, Francis, et al. 2019. "On the Neutrino Flares from the Direction of TXS 0506+056". *ApJ* 874, no. 1, L9 (): L9.

Healey, Stephen E., et al. 2007. "CRATES: An All-Sky Survey of Flat-Spectrum Radio Sources". *The Astrophysical Journal Supplement Series* 171, no. 1 (): 61–71.

Heidt, J., et al. 2004. "Evolution of BL Lacertae host galaxies". *A&A* 418 (): 813–825.

HI4PI Collaboration et al. 2016. "HI4PI: A full-sky H I survey based on EBHIS and GASS". *A&A* 594, A116 (): A116.

Hovatta, T., et al. 2020. "Association of IceCube neutrinos with radio sources observed at Owens Valley and Metsähovi Radio Observatories". *arXiv e-prints*, arXiv:2009.10523 (): arXiv:2009.10523.

IceCube Collaboration. 2013. "Evidence for High-Energy Extraterrestrial Neutrinos at the IceCube Detector". *Science* 342, no. 6161, 1242856 (): 1242856.

IceCube Collaboration et al. 2018a. "Multimessenger observations of a flaring blazar coincident with high-energy neutrino IceCube-170922A". *Science* 361, no. 6398, eaat1378 (): eaat1378.

IceCube Collaboration et al. 2018b. "Neutrino emission from the direction of the blazar TXS 0506+056 prior to the IceCube-170922A alert". *Science* 361, no. 6398 (): 147–151.

IceCube Collaboration et al. 2017. "The IceCube Neutrino Observatory - Contributions to ICRC 2017 Part II: Properties of the Atmospheric and Astrophysical Neutrino Flux". *arXiv e-prints*, arXiv:1710.01191 (): arXiv:1710.01191.

Keivani, A., et al. 2018. "A Multimessenger Picture of the Flaring Blazar TXS 0506+056: Implications for High-energy Neutrino Emission and Cosmic-Ray Acceleration". *The Astrophysical Journal* 864, no. 1 (): 84.

López-Oramas, Alicia. 2015. "Multi-year Campaign of the Gamma-Ray Binary LS I +61 303 and Search for VHE Emission from Gamma-Ray Binary Candidates with the MAGIC Telescopes" ().

Lucarelli, F., et al. 2017. "AGILEDetection of a Candidate Gamma-Ray Precursor to the ICECUBE-160731 Neutrino Event". *The Astrophysical Journal* 846, no. 2 (): 121.

Mannheim, K. 1993. "The proton blazar." *Astronomy&Astrophysics* 269 (): 67–76.

Massaro, E., et al. 2004. "Log-parabolic spectra and particle acceleration in the BL Lac object Mkn 421: Spectral analysis of the complete BeppoSAX wide band X-ray data set". *A&A* 413 (): 489–503.

Mészáros, P. 2017. "Astrophysical Sources of High-Energy Neutrinos in the IceCube Era". *Annual Review of Nuclear and Particle Science* 67 (): 45–67.

Nilsson, K., et al. 2018. "Long-term optical monitoring of TeV emitting blazars. I. Data analysis". *A&A* 620, A185 (): A185.

Padovani, P., and E. Resconi. 2014. "Are both BL Lacs and pulsar wind nebulae the astrophysical counterparts of IceCube neutrino events?" *Monthly Notices of the Royal Astronomical Society* 443, no. 1 (): 474–484.

Padovani, P., A. Turcati, and E. Resconi. 2018a. "AGN outflows as neutrino sources: an observational test". *Monthly Notices of the Royal Astronomical Society* 477 (3): 3469–3479.

Padovani, P., et al. 2015a. "A simplified view of blazars: the neutrino background". *Monthly Notices of the Royal Astronomical Society* 452, no. 2 (): 1877–1887. ISSN: 0035-8711.

— . 2015b. "A simplified view of blazars: the neutrino background". *Monthly Notices of the Royal Astronomical Society* 452, no. 2 (): 1877–1887.

Padovani, P., et al. 2016. "Extreme blazars as counterparts of IceCube astrophysical neutrinos". *Monthly Notices of the Royal Astronomical Society* 457, no. 4 (): 3582–3592.

Padovani, Paolo, and Paolo Giommi. 1995. "The Connection between X-Ray– and Radio-selected BL Lacertae Objects". *The Astrophysical Journal* 444 (): 567.

Padovani, P, et al. 2018b. "Dissecting the region around IceCube-170922A: the blazar TXS 0506+056 as the first cosmic neutrino source". *Monthly Notices of the Royal Astronomical Society* 480, no. 1 (): 192–203. ISSN: 0035-8711.

Padovani, P, et al. 2019. "TXS 0506+056, the first cosmic neutrino source, is not a BL Lac". *Monthly Notices of the Royal Astronomical Society: Letters* 484, no. 1 (): L104–L108. ISSN: 1745-3925.

Paiano, Simona, et al. 2018. "The Redshift of the BL Lac Object TXS 0506+056". *The Astrophysical Journal* 854, no. 2 (): L32.

Petropoulou, M., and A. Mastichiadis. 2014. "Bethe–Heitler emission in BL Lacs: filling the gap between X-rays and -rays". *Monthly Notices of the Royal Astronomical Society* 447, no. 1 (): 36–48. ISSN: 0035-8711.

Petropoulou, M., et al. 2015. "Photohadronic origin of γ-ray BL Lac emission: implications for IceCube neutrinos". *Monthly Notices of the Royal Astronomical Society* 448, no. 3 (): 2412–2429. ISSN: 0035-8711.

Petropoulou, Maria, et al. 2020. "Multi-epoch Modeling of TXS 0506+056 and Implications for Long-term High-energy Neutrino Emission". *ApJ* 891, no. 2, 115 (): 115.

Quataert, E. 2004. "Radiatively Inefficient Accretion Flows". In *AGN Physics with the Sloan Digital Sky Survey*, ed. by Gordon T. Richards and Patrick B. Hall, 311:131. Astronomical Society of the Pacific Conference Series.

Read, A L. 2002. "Presentation of search results: theCLstechnique". *Journal of Physics G: Nuclear and Particle Physics* 28, no. 10 (): 2693–2704.

Righi, C, F Tavecchio, and S Inoue. 2018. "Neutrino emission from BL Lac objects: the role of radiatively inefficient accretion flows". *Monthly Notices of the Royal Astronomical Society: Letters* 483, no. 1 (): L127–L131. ISSN: 1745-3925.

Rodrigues, Xavier, et al. 2020. "Multi-wavelength and neutrino emission from blazar PKS 1502+106". *arXiv e-prints*, arXiv:2009.04026 (): arXiv:2009.04026.

Sahakyan, Narek. 2018. "Lepto-hadronic Gamma-Ray and Neutrino Emission from the Jet of TXS 0506+056". *The Astrophysical Journal* 866, no. 2 (): 109.

Satalecka, K., et al. 2019. "Neutrino Target of Opportunity program of the Cherenkov Telescope Array". In *36th International Cosmic Ray Conference (ICRC2019)*, 36:784. International Cosmic Ray Conference.

Sikora, Marek, Mitchell C. Begelman, and Martin J. Rees. 1994. "Comptonization of Diffuse Ambient Radiation by a Relativistic Jet: The Source of Gamma Rays from Blazars?" *The Astrophysica Journal* 421 (): 153.

Spurio, M. 2018. *Probes of Multimessenger Astrophysics*. Springer International Publishing. ISBN: 978-3-319-96853-7.

Svensson, Roland. 1987. "Non-thermal pair production in compact X-ray sources: first-order Compton cascades in soft radiation fields". *Monthly Notices of the Royal Astronomical Society* 227, no. 2 (): 403–451. ISSN: 0035-8711.

Tanaka, Yasuyuki T., Sara Buson, and Daniel Kocevski. 2017. "Fermi-LAT detection of increased gamma-ray activity of TXS 0506+056, located inside the IceCube-170922A error region." *The Astronomer's Telegram* 10791 (): 1.

Tavani, M. et al. 2009. "The AGILE Mission". *Astronomy&Astrophysics* 502, no. 3 (): 995–1013.

Tavecchio, Fabrizio, and Gabriele Ghisellini. 2008a. "Spine–sheath layer radiative interplay in subparsec-scale jets and the TeV emission from M87". *Monthly Notices of the Royal Astronomical Society: Letters* 385, no. 1 (): L98–L102. ISSN: 1745-3925.

— . 2008b. "Structured jets and VHE emission of blazars and radiogalaxies". In *American Institute of Physics Conference Series*, ed. by Felix A. Aharonian, Werner Hofmann, and Frank Rieger, 1085:431–434. American Institute of Physics Conference Series.

The IceCube Collaboration et al. 2015. "The IceCube Neutrino Observatory - Contributions to ICRC 2015 Part II: Atmospheric and Astrophysical Diffuse Neutrino Searches of All Flavors". *arXiv e-prints*, arXiv:1510.05223 (): arXiv:1510.05223.

Urry, C. Megan, and Paolo Padovani. 1995. "Unified Schemes for Radio-Loud Active Galactic Nuclei". *Publications of the Astronomical Society of the Pacific* 107 (): 803.

Wakely, S. P., and D. Horan. 2008. "TeVCat: An online catalog for Very High Energy Gamma-Ray Astronomy". In *International Cosmic Ray Conference*, 3:1341–1344. International Cosmic Ray Conference.

Walker, R. Craig, et al. 2018. "The Structure and Dynamics of the Subparsec Jet in M87 Based on 50 VLBA Observations over 17 Years at 43 GHz". *ApJ* 855, no. 2, 128 (): 128.

Wilks, S. S. 1938. "The Large-Sample Distribution of the Likelihood Ratio for Testing Composite Hypotheses". *The Annals of Mathematical Statistics* 9 (1): 60–62.

Wood, M., et al. 2017. "Fermipy: An open-source Python package for analysis of Fermi-LAT Data". In *35th International Cosmic Ray Conference (ICRC2017)*, 301:824. International Cosmic Ray Conference.

Zhang, Jin, et al. 2017. "Multiple-wavelength Variability and Quasi-periodic Oscillation of PMN J0948+0022". *The Astrophysical Journal* 849, no. 1, 42 (): 42.